# IMPACT OF TWO POTENTIAL POLICY OPTIONS ON ATMOSPHERIC CHEMISTRY AND CLIMATE: HYDROGEN ECONOMY AND LOW-GWP ALTERNATIVES TO OZONE DEPLETING SUBSTANCES

BY

DONG WANG

DISSERTATION

Submitted in partial fulfillment of the requirements
for the degree of Doctor of Philosophy in Atmospheric Sciences
in the Graduate College of the
University of Illinois at Urbana-Champaign, 2012

Urbana, Illinois

Doctoral Committee:

Professor Donald J. Wuebbles, Chair
Professor Angus Rockett
Assistant Professor Nicole Riemer
Assistant Professor Somnath Baidya Roy

## ABSTRACT

The fingerprint of human activities on the composition of Earth's atmosphere is manifest. It is now well recognized that the changes in the atmospheric composition due to human activities have resulted in changes in several aspects of the environment, e.g., attenuation of the ozone layer due to emissions of ozone-depleting substances, climate change due to greenhouse gas emissions, and air pollution due to fossil fuel combustion. This research analyzes the impacts of two potential future policy options, (1) hydrogen economy and (2) low-GWP (Global Warming Potential) alternatives to hydrofluorocarbons (HFCs) and hydrochlorofluorocarbons (HCFCs), on the composition of the atmosphere, on environment, on climate and on stratospheric ozone.

This research is accomplished by using state-of-the-art numerical models that represents detailed physical and chemical processes of the atmosphere with cutting-edge knowledge, together with specifically developed scenarios. This methodology can provide policymakers with prospective and insightful knowledge essential to effectively tackling the environmental issues caused by human activities.

This research gives a comprehensive analysis of the impacts of a future (2050) hydrogen economy on atmospheric environment. The uncertainties in the evolution paths of the world are bounded by the IPCC SRES high emission A1FI and low emission B1 scenarios. The atmospheric impacts of an internal combustion engine type hydrogen economy are analyzed for the first time in this research, as well as a fuel cell type hydrogen economy. The impacts of a future hydrogen economy analyzed based on global model simulations in this research include:

changes in atmospheric hydrogen budget, effectiveness in improving air quality in different regions of the world, changes in the oxidative power of the atmosphere and the climate implication, and stability of the ozone layer. Air quality improvement in a hydrogen economy for the contiguous United States is analyzed based on regional air quality model simulations with finer resolution. It is found that hydrogen economy can improve air quality, provide opportunities to mitigate climate change without significantly harming stability of the ozone layer.

This research evaluates atmospheric lifetimes and GWP values for six unsaturated halogenated hydrocarbons, which are potential low-GWP alternatives to HFCs and HCFCs, using a three-dimensional global climate-chemistry model and a radiative transfer model. It is found that the alternative compounds have lifetimes less than a month and GWPs less than 5, orders of magnitude smaller than the long-lived HFCs. This research also analyzes the inadequacies of the simple estimation approach, which is used in several prior published studies, for very short-lived substances (VSLS). A rationale of evaluating GWPs for VSLS using three-dimensional atmospheric models is presented.

Dedicated to My Parents

## ACKNOWLEDGEMENTS

The research was supported in part by the United States Department of Energy through award number DE-FC36-07GO17109 to the University of Illinois project 'Evaluation of the Potential Environmental Impacts from Large-Scale Use and Production of Hydrogen in Energy and Transportation Applications'.

I would thank my advisor Prof. Don Wuebbles, who not only provides me with helpful advices, but also sets a good example of professional scientist to me. I thank Dr. Ken Patten for preparing models and helping model output analyses; Dr. Seth Olsen for preparing models and running the CMAQ model simulations; Wenjing Jia for preparing emission files in the hydrogen economy scenarios; Dr. Hugh Pitcher for providing projections of energy efficiency; Drs. Jin-Tai Lin, Daeok Youn, M. K. Dubey, and Dr. Rajiv Singh for helpful discussions; and my doctoral committee members Profs. Angus Rockett, Somnath Baidya Roy, and Nicole Riemer for guidance and revisions. My thanks also go to my group members, with whom I spent years of pleasant time together.

## TABLE OF CONTENTS

# CHAPTER 1: INTRODUCTION

## 1.1. Motivation

The fingerprint of human activities on the composition of Earth's atmosphere is manifest. It is now well recognized that the changes in the atmospheric composition due to human activities have resulted in changes in several aspects of the environment. The increased greenhouse gases in the atmosphere have altered the radiative balance of this planet, leading to rapid changes in climate. Tailpipe exhaust of on-road vehicles has led to issues of deteriorated air quality, raising human and plant health and visibility concerns. The introduction of chlorofluorocarbons (CFCs), a family of chemical compounds that are completely manmade, into the atmosphere has led to unexpected depletion of ozone in the stratosphere.

This doctoral dissertation focuses on the impacts of two potential future policy options, (1) hydrogen economy and (2) low-GWP (Global Warming Potential) alternatives to hydrofluorocarbons (HFCs) and hydrochlorofluorocarbons (HCFCs), on the composition of the atmosphere, on environment, on climate and on stratospheric ozone. State-of-the-art numerical models representing detailed physical and chemical processes of the atmosphere will be used as key tools, together with carefully designed emission scenarios. Numerical modeling studies of the future atmosphere with specifically developed scenarios can provide policymakers with prospective and insightful information that cannot be obtained in other ways. In this research, a number of state-of-the-art three-dimensional global atmospheric chemistry-transport and climate-chemistry models, as well as a radiative transfer model, will be used as key research tools to address the science questions in the present thesis.

## 1.2. Hydrogen Economy

### *1.2.1. Research Background*

A hydrogen economy is an infrastructure system using molecular hydrogen ($H_2$) as energy carrier. In practice, $H_2$ is most likely to substitute currently used fossil fuels to provide on-road vehicles with motive power. Fossil fuel combustion in on-road vehicles emits a number of pollutants directly into the surrounding air. The exhaust air contains nitrogen oxides ($NO_x$=NO+$NO_2$), carbon monoxide (CO), volatile organic compounds (VOCs), and particulate matter. These byproducts can have adverse impacts on human health. For example, sustained high levels of $NO_2$ have an adverse impact on the respiratory system; elevated CO concentrations degrade the ability of blood to transport oxygen (e.g. WHO/Europe, 2003). In addition, $NO_x$, CO and VOCs are precursors to the formation of ground-level ozone ($O_3$), which adversely impacts human health and ecosystems in a number of ways. Particulate matter, which raises concern of physiological hazard, is either directly released in the form of soot (black carbon) or formed indirectly from gaseous pollutants through a series of photochemical and physical processes (sulfate and secondary organics). In the United States on-road vehicles rank first in $NO_x$ and CO emissions and second in VOCs emissions among all source sectors (U.S. EPA, 2009). In the future the on-road vehicle fleet is expected to become an increasingly important contributor to ambient air pollution.

On-road vehicles using $H_2$ as energy carrier offers opportunities to avoid the negative effects of using fossil fuels, as $H_2$ has higher energy efficiency and much cleaner oxidation products. $H_2$ fuel cells emit only water vapor ($H_2O$) and eliminate emissions of NOx, CO, VOCs (volatile organic compounds), and soot associated with fossil fuel combustions. Given these

reductions in tailpipe pollutant emissions it is reasonably foreseeable that transitioning the world's road traffic from fossil fuel powered vehicles to $H_2$ powered vehicles could substantially improve air quality and climate provided that the $H_2$ is produced by non-polluting methods, e.g. wind, solar, nuclear power, hydroelectricity or, promisingly, photocatalytic and photoelectrochemical dissociation of water (Abe, 2010) and microbial reverse-electrodialysis electrolysis cells (Kim and Logan, 2011). Even if $H_2$ is generated conventionally from fossil fuel, it would be easier to control the pollutant emissions from $H_2$ production since the emissions would occur at a few concentrated locations ($H_2$ production plants); the produced $CO_2$ could be sequestered in this case.

*1.2.2. Current Understanding and Remaining Issues*

There are a few modeling experiments in previously published literature on potential impact of a hydrogen economy (Derwent et al., 2006; Jacobson et al., 2005; Jacobson, 2008; Schultz et al., 2003; Tromp et al., 2003; Warwick et al., 2004); however, the current understanding about $H_2$ does not constitute a holistic picture with detailed scientific knowledge. The inadequacies of the previous studies are summarized in the following discussion.

First, the extent to which a hydrogen economy would change the $H_2$ budget in the atmosphere is not yet clear from the previous studies, despite that this question is of importance. There are several reasons why $H_2$ abundance in the atmosphere is important. To name a few, it has impacts on the climate (indirect), on stratospheric ozone and on metal structure. $H_2$ itself is not a direct greenhouse gas, as $H_2$ does not absorb infrared radiation. However, $H_2$ in the atmosphere reacts with the hydroxyl radical (OH); increase in atmospheric $H_2$ concentration may decrease OH abundance, leading to slower removal of methane ($CH_4$), a powerful greenhouse gas, from the atmosphere. In addition, it was speculated that increase in atmospheric $H_2$

concentration can significantly reduce ozone concentrations in the atmosphere in the polar regions (Tromp et al., 2003), although later studies found relatively modest changes (Warwick et al., 2004; Jacobson, 2008). Furthermore, increased ambient $H_2$ concentrations raise concerns of hydrogen embrittlement (e.g. Johnson, 1973).

Tropospheric $H_2$ concentrations are currently around 530 ppbv (Novelli et al., 1999), making it second to $CH_4$ as the most abundant oxidizable gas in the atmosphere (Constant et al., 2009). The primary sources of $H_2$ are fossil fuel and biofuel combustion, biomass burning, ocean emissions, and photolysis of formaldehyde. Bottom-up inventories estimate its source as ~75 $TgH_2$/yr (Ehhalt and Rohrer, 2009). Its largest sink (~80%) is microbial uptake in soils, with oxidation by OH in the atmosphere making up the remainder of its loss (Constant et al., 2009). Its uptake by microbes in soil, despite its importance, is not well understood and is subject to large uncertainties. Observations show a correlation between the $H_2$ and CO deposition velocities (Conrad and Seiler, 1985; Liebl and Seiler, 1976; Yonemura et al., 1999; Yonemura et al., 2000). In this study, $H_2$ soil sink will be modeled based on its correlation with CO deposition velocities.

$H_2$'s total atmospheric lifetime is estimated to be 1 to 2 years (Constant et al., 2009; Ehhalt and Rohrer, 2009; Novelli et al., 1999; Price et al., 2007) and its lifetime with respect to OH loss is ~8 years (Ehhalt and Rohrer, 2009). The latitudinal gradient of $H_2$ concentrations is unique from many other trace gases with ~3% higher average concentrations in the Southern Hemisphere than in the Northern Hemisphere. This is thought to be due to the greater soil microbial uptake over land in the Northern Hemisphere (Ehhalt and Rohrer, 2009).

No clear long term trend of atmospheric $H_2$ concentration has been revealed in the literature (Constant et al., 2009; Ehhalt and Rohrer, 2009). However, a conversion to a $H_2$-based

road transportation sector can elevate atmospheric $H_2$ concentrations to values not previously experienced, as a result of fugitive emissions of $H_2$ during its production, transportation and storage processes; there is large uncertainty in estimating this increase in the literature.

Second, because of the inhomogeneity of transportation activities around the world, it is imperative to find out how significant a hydrogen economy improves air quality for each specific region. There are a limited number of studies on the impacts of a hydrogen economy on tropospheric chemistry and air quality. A 3-D global modeling study by Schultz et al. (2003) suggested a $H_2$ fuel cell road traffic fleet in ca. 2000 would reduce human emissions of NOx and CO by half, resulting in 3%, 5% and 29% decrease in tropospheric CO, $O_3$ and NOx, respectively. Warwick et al. (2004) reported a 2.2% decrease in tropospheric $O_3$ in a $H_2$ economy based on a 2-D global modeling study. These global studies lack detailed analysis of air quality improvement in terms of how much change in concentrations of each key species will take place in each region. Jacobson et al. (2005) compared the environmental impact of a 1999 hydrogen on-road vehicle fleet in the United States by means of steam reforming of natural gas, wind electrolysis, and coal gasification; they found the wind and natural gas options have the best desired environmental improvement. This study only focused on the United States, whereas in developing countries like China and India concerns of air quality is increasing.

Third, it is not yet clear by how much a hydrogen economy changes the oxidative power of the atmosphere. Even though utilization of $H_2$ could provide opportunities to offset $CO_2$ emissions, climate concerns have arisen due to its indirect greenhouse potential by affecting OH abundance in the atmosphere (e.g. Prather, 2003). A hydrogen economy can affect OH abundance via the reaction of $H_2$ and OH, through changes in concentration of ozone, whose photolysis initiates the reactions producing OH in the troposphere, and through changes in

concentrations of VOCs, which react with OH and are ozone precursors. Changes in OH abundance can affect $CH_4$ lifetime in the atmosphere. $CH_4$ is an ozone precursor and a greenhouse gas that is 25 times more powerful than $CO_2$ in terms of integrated radiative forcing over a 100-year time horizon. Currently its radiative forcing is second only to that of $CO_2$ (IPCC, 2007). The removal rate of $CH_4$ depends critically on the oxidative power of the atmosphere.

Taking all effects associated with emission changes in a hydrogen economy into account, the decrease in tropospheric OH abundance ranges from 0% to 12%, and the increase in $CH_4$ lifetime ranges from 0% to 26%, depending on the specific scenario assumed (Jacobson, 2008; Schultz et al., 2003; Warwick et al., 2004). In this study, the combined effect of all emission changes associated with a hydrogen economy will be examined using a 3-D global climate-chemistry model that have included cutting-edge knowledge of the related physical and chemical processes in the atmosphere.

Fourth, there is not a consensus on whether a $H_2$ economy poses a threat to the ozone layer. There are a few papers on a hydrogen economy containing discussion over the impact of a hydrogen economy on stratospheric ozone. Under an assumption of more than quadrupled surface $H_2$ concentration (2.3 ppmv) in a hydrogen society due to a somewhat unrealistically high $H_2$ leakage rate (~12%), and without considering any changes in fossil fuel combustion related emissions, a 2-D model study by Tromp et al. (2003) found spatial and temporal enhancement of polar ozone holes, leading to ozone depletion of 3%~8%, due to lowered stratospheric temperature, resulting from increased stratospheric water vapor from oxidized $H_2$. Warwick et al. (2004) found a slight increase of 0.1% in stratospheric ozone, considering associated changes in CO, NOx, VOCs emissions with $H_2$ fuel cells in a 2-D model, with an assumed $H_2$ concentration of 1.4 ppmv. Jacobson (2008) reported a 0.4% increase in column

ozone assuming $H_2$ fuel cell vehicles with their associated decrease in fossil fuel combustion related emissions and a 3% $H_2$ leakage rate. There exists large uncertainty in the impact on stratospheric ozone; even the sign of changes in stratospheric ozone concentration is not unanimous in previous studies.

Local ozone concentration in the stratosphere is affected by atmospheric transport, photochemical production and catalytic loss. In the case of a hydrogen economy, the catalytic cycles are likely to be significantly perturbed as a result of changes in surface emission. Previous studies, however, did not explain in a detailed manner how these catalytic cycles will change in a hydrogen economy. To address the question as how will stratospheric ozone change, detailed analyses of the perturbations of a hydrogen economy to all the catalytic ozone destruction cycles are carried out in this research.

In addition, $H_2$ can also be burned in internal combustion engines, as well as being oxidized in fuel cells. Vehicles powered by $H_2$ internal combustion engines emit no CO, VOCs, or soot but do emit NOx (Deboer, 1976). NOx plays an important role in tropospheric chemistry; changes in NOx emissions may lead to much different effects on air quality, especially near surface ozone. To date, there is no published research on environmental impacts of this technical option; the impact of the $H_2$ internal combustion engines option will be investigated for the first time in this research.

Furthermore, it should also be pointed out that all the previous studies were based on the near 2000 background atmosphere, assuming an immediate transition to hydrogen technology. The transition to hydrogen based energy delivery will, in real-world practice nevertheless, require the development of a massive industrial $H_2$ production capacity and substantial changes

to the energy delivery infrastructure. To date, there are still a number of technological barriers yet to overcome. Considering the time needed to make the current infrastructure compatible with a hydrogen economy, the impacts of such a transition will be evaluated for the future to allow reasonable time for the infrastructure changes to occur. In this research, it is assumed that in the coming decades road transportation will gradually convert to $H_2$ powered such that the transition will be complete by 2050. That is, all on-road vehicles operating in 2050 will be powered by $H_2$.

### *1.2.3. Research Objectives*

This research aims at quantitatively answering the following major research questions regarding a future hydrogen economy:

a) To what extent does a hydrogen economy change the $H_2$ budget in the atmosphere?

b) How effective does a hydrogen economy improve air quality?

c) To what extent does a hydrogen economy change the oxidative power of the atmosphere?

d) Does a hydrogen economy significantly perturb ozone in the stratosphere?

State-of-the-art atmospheric model simulations based on specifically developed emission scenarios are performed. The numerical models and the scenarios are described in Chapter 2.

## 1.3. Low-GWP Alternatives to Ozone-Depleting Substances

### *1.3.1. Research Background*

The Montreal Protocol is a multilateral agreement that has been successfully protecting ozone in the atmosphere. The protocol has phase-out management plans for CFCs and HCFCs, whose role is being and expected to be replaced in a large part with HFCs. However, concerns of significant radiative forcing arise as HFCs are potent greenhouse gases. HFCs are ~100 to ~15,000 times more powerful than $CO_2$ in terms of radiative forcing integrated over a 100-year horizon after emission on a per-mass basis (IPCC, 2007). Their use is expected to increase, especially in developing countries in Asia. It projected that the radiative forcing caused by HFCs will be of that due to the $CO_2$ emitted between now and then, should the trend of increasing usage of HFCs continue (Velders et al., 2009; UNEP, 2011).

It is well established that the C=C bonds are more prone than C-C or C-H bonds to react with the hydroxyl radical (OH) in the atmosphere (Atkinson et al., 2005). Recently, various unsaturated (molecules containing double bond) halogenated hydrocarbons with very short atmospheric lifetimes have been proposed as substitutes for HCFCs and longer-lived HFCs. These short-lived substances are expected to have small, if not negligible, effects on atmospheric ozone and on climate. The chemical compounds include *trans*-1-chloro-3,3,3-trifluoropropylene (*trans*-$CF_3CH$=CHCl, or tCFP for short), and five hydrofluoro-olefins (HFOs): 2,3,3,3-tetrafluoropropene ($CF_3$-CF=$CH_2$, or HFO-1234yf), *trans*-1,3,3,3-tetrafluoropropene (*trans*-CHF=CH-$CF_3$, or HFO-1234ze(E)), *cis*-1,3,3,3-tetrafluoropropene (*cis*-CHF=CH-$CF_3$, or HFO-1234ze(Z)), *cis*-1,2,3,3,3-pentafluoropropene (*cis*-$CF_3$-CF=CHF, or HFO-1225ye(Z)), and *trans*-1,2,3,3,3-pentafluoropropene (*trans*-$CF_3$-CF=CHF, or HFO-1225ye(E)). HFO-1234yf can serve as a mobile air conditioning refrigerant. HFO-1234ze(E) can work as a blowing agent and propellant; tCFP can serve as a blowing agent. HFO-1234ze(Z) has been suggested as a

refrigerant (Brown et al., 2009). HFO-1225ye(Z) and -1225ye(E) also have potential refrigerant use (Hruley et al., 2007).

### *1.3.2. Current Understanding and Remaining Issues*

The prospect of HFO-1234yf and HFO-1234ze(E) as low-GWP alternatives to ODSs has been recently discussed in the literature (UNEP, 2011; Velders et al., 2012). The discussions are based on atmospheric lifetimes and GWP values (Nielsen et al., 2007; Sondergaard et al., 2007) estimated using a simple estimation approach (Pinnock et al., 1995). Nevertheless, it should be pointed out that, as will be discussed below and in Chapter 5, the simple approach is inadequate to accurately estimate lifetimes and GWPs for short-lived gases, and has led to significantly inaccuracies in lifetime and GWP evaluations. Accurate lifetime and GWP estimation is important in comparing cost and benefit among alternatives to ODSs and, furthermore, shaping policy decisions that direct future production and consumption of chemical compounds that have impacts on the ozone layer and/or on climate.

The first inadequacy of the estimation approach is that it uses the reaction rate of the gas of interest and OH obtained in laboratory experiments and a global weighted-average atmospheric OH concentration, which does not actually exist for short-lived gases, as OH concentrations vary significantly in the atmosphere. The second inadequacy is that the relative efficiencies of these gases in changing Earth's radiative forcing are calculated in models assuming constant mixing ratio profiles throughout the atmosphere (troposphere and stratosphere).

### *1.3.3. Research Objectives*

This research has the following objectives:

a) Derive atmospheric lifetimes for these alternative compounds to ODSs using a state-of-the-art three-dimensional climate-chemistry model and realistic emission geographical distribution. Compare the lifetimes derived from 3-D modeling method with the lifetimes derived from the simple estimation approach. Identify the inadequacy of the estimation approach.

b) Using the concentration profiles for these alternative compounds derived from 3-D models, evaluate the radiative effects of these compounds in a radiative transfer model, and calculate their GWP values. Compare the derived GWP values with those estimated by the simple approach, and identify the inadequacy of the simple approach.

c) Formulate a rationale of evaluating GWPs for very short-lived substances.

# CHAPTER 2: RESEARCH METHODOLOGY

This chapter describes the research methodology essential to tackling research questions discussed in Chapter 1. This chapter gives brief descriptions of the numerical atmospheric models that are used in this research, and then describes a set of emission scenarios developed for hydrogen economy studies.

## 2.1. Model Descriptions

### *2.1.1. CAM-Chem*

The Community Atmosphere Model with Chemistry (CAM-Chem) (Lamarque et al., 2005 and 2011; Pfister et al., 2008) is a three-dimensional global climate-chemistry model. CAM-Chem's chemistry module is based on the chemical component of the Model for OZone And Related chemical Tracers (MOZART). MOZART was described and extensively evaluated by Horowitz et al. (2003), and has been employed in a number of studies (e.g. Huang et al., 2008; Lin et al., 2008a; Lin et al., 2008b; Tie et al., 2005). CAM-Chem contains a comprehensive tropospheric gas phase and aerosol chemical mechanism and includes 119 species and 300 reactions. CAM-Chem uses a bulk aerosol method and includes organic carbon, black carbon, sulfate, and ammonium nitrate aerosols. Based on the observed correlation between $H_2$ and CO deposition velocities (Conrad and Seiler, 1985; Liebl and Seiler, 1976; Yonemura et al., 1999; Yonemura et al., 2000), a $H_2$ deposition velocity equal to twice the CO deposition velocity is adopted and used in this research.

CAM-Chem is used in this research to evaluate the impact of a hydrogen economy on global troposphere chemistry. For this research, the global atmosphere is divided into grids with a horizontal resolution of 1.9º latitude by 2.5º longitude and 26 vertical layers extending from the

surface to 3-millibar level (~40 km altitude). The meteorology is prescribed by climate model output data from Community Climate System Model (CCSM) which corresponds to the climate state of the mid-1990s. The reason of doing so is that the focus of this research is on air quality and photochemistry influenced impacts due to changes in emissions. Previous studies (e.g. Lin et al., 2008a; Wu et al., 2008) have shown that future climate changes will likely have less effect on air quality than the future changes in emissions. The model is integrated with a time step of 30 minutes. After completion of one year's calculation, the meteorology field is repeated for the next year. This method allows the impact of changes in emissions to be investigated excluding the possible influences of changes in meteorology. The 2050 monthly mean lower boundary $CH_4$ concentrations are scaled from the 2000 value (annual mean 1776 ppbv) to the concentrations projected by IPCC (2001) in 2050, 2668 ppbv for the A1FI scenario and 1881 ppbv for the B1 scenario. The model is run for eight years and has reached steady state, that is, year-to-year relative difference of key species is less than 1%. The analyses of the simulation results, which are described and discussed in Chapter 3, are based on model output data of the last year of simulation.

*2.1.2. CMAQ*

The Community Multiscale Air Quality Modeling System (CMAQ) is a high-resolution regional air quality model. The CMAQ model was initially released to the public by the United States Environmental Protection Agency (U.S. EPA) in 1998 and has undergone many revisions and improvements since (e.g. Appel et al., 2007; Appel et al., 2008). The CMAQ modeling system was designed to approach air quality as a whole by including state-of-the-science capabilities for modeling multiple air quality issues, including tropospheric ozone, fine particles, toxics, acid deposition, and visibility degradation.

In this research, the CMAQ model version 4.6 is used to assess the regional air quality impacts of a $H_2$-based road transportation sector on the contiguous United States with finer resolution. The resolution is 30 km by 30 km horizontally with 22 vertical layers from the surface to 13 km, with a relatively finer resolution in the boundary layer with 5 layers in the first km. The meteorological data driving CMAQ is from a climate version of the MM5 model (CMM5; e.g. Liang et al., 2001) for the year 1995. For this study CMAQ uses the Carbon Bond 5 gas phase photochemistry package (Luecken, et al., 2008; Sarwar, et al., 2008) with 56 species and 156 reactions. The aerosol chemistry package is coupled to the gas phase chemistry package and contains 34 transported aerosol modes. The aerosol package represents the particle size distribution as the superposition of three lognormal modes. The processes of coagulation, particle growth by the addition of new mass, and particle formation are included. Time stepping is done utilizing an analytical solution to the differential equations for the conservation of number and species mass conservation. The simulation was carried out with a 12 minute dynamical timestep and the chemistry package using a 2.5 min sub-timestep. Detailed descriptions of the mechanisms, algorithms, and implementation are available in the CMAQ scientific documentation (Byun and Schere, 2006). Boundary conditions for the CMAQ model simulations are taken from the corresponding global tropospheric model simulations. The CMAQ simulations are performed for the BL, $H_2$-FC, and $H_2$-ICE scenarios for each IPCC scenario, which are described in details in Section 2.2.

*2.1.3. MOZART*

The Model for OZone And Related chemical Tracers (MOZART) is a three-dimensional global chemistry transport model. MOZART has been evaluated and used in a number of studies on stratospheric chemistry (e.g. Gettelman et al., 2004; Kinnison et al., 2007; Kulawik et al.,

2006; Liu et al., 2009; Liu et al., 2011; Pan et al., 2007; Park et al., 2004). It simulates in a detailed fashion the physical and chemical processes of the troposphere and stratosphere. It has 108 species, 71 photochemical reactions, 218 gas phase reactions and 18 heterogeneous reactions including heterogeneous chemistry in the stratosphere and polar stratospheric cloud processes.

MOZART version 3.1 is used in this research to evaluate the atmospheric impacts of a hydrogen economy on stratospheric ozone. The model simulates the atmosphere from the surface to 0.001 Pa level (~115km) by dividing it vertically into 60 layers. Horizontally the globe is partitioned into 96 grids on latitude and 144 grids on longitude, corresponding to a resolution of 1.9º x 2.5º (latitude x longitude). The model is driven with meteorology from a year of simulation of the Whole-Atmosphere Community Climate Model version 3 (WACCM-3) (Sassi et al., 2004), which represents the mid-1990s atmosphere. This meteorology is repeated for each year for multiyear simulations. The reason of doing this is described in Section 2.1.1, as for the CAM-Chem tropospheric chemistry simulations.

*2.1.4. WACCM*

The Whole Atmosphere Community Climate Model (WACCM) is an atmospheric climate-chemistry model developed by the National Center for Atmospheric Research (NCAR). The model has been evaluated and used in a number of scientific studies, for example, in the Stratospheric Processes And their Role in Climate (SPARC) 2010 Report (Eyring et al., 2010). The model simulates 125 chemical species and uses the JPL06 recommendations on chemical reactions in the atmosphere (Sander et al., 2006) including extensions for non-methane hydrocarbon chemistry, which is key for a good representation of tropospheric oxidative capacity. WACCM numerically simulates the atmosphere from the surface up to the $4.5 \times 10^{-4}$ Pa level (~145km). The model performs well in simulating the stratosphere and the upper

troposphere and lower stratosphere as shown in the Chemistry-Climate Model Validation Activity (CCMVal) (Eyring et al., 2010; Gettelman et al., 2010).

WACCM version 3.5.48 is used in this study to derive the steady-state concentration profiles and atmospheric lifetimes for the alternative compounds to ODSs. The model is run in offline mode, which means that the meteorological fields are provided by a previous run of WACCM representing the year 2000 atmosphere (R. Garcia, private communication, 2007). By doing this, the effect of changing meteorology field is removed. In order to filter possible effects from changing weather conditions, the model is run in offline mode, that is, the meteorological fields are driven by a meteorological dataset obtained from a previous WACCM run approximating the current atmosphere (R. Garcia, private communication, 2007); after one year's simulation is complete, the meteorological dataset is repeated again. The WACCM model is run for five years so that key species reach steady state. Concentrations profiles and lifetime evaluation are based on analysis of the fifth year's WACCM output.

*2.1.5. UIUC RTM*

The radiation effects of the proposed alternative compounds to ODSs are evaluated with the University of Illinois at Urbana-Champaign Radiative Transfer Model (UIUC RTM). The UIUC RTM was derived from the radiative transfer models of the Community Climate Model (CCM; Briegleb, 1992a, 1992b). Previous versions of the UIUC RTM have been employed in several climate effects studies (e.g. Jain et al., 2000; Naik et al., 2000; Youn et al., 2009; Patten et al., 2011).

Shortwave (solar) and longwave (terrestrial) radiation across atmospheric layers is calculated in the UIUC RTM. For the solar part, 18 bins between 0.2 and 5.0 microns are

calculated taking into account of the absorption effects of $H_2O$, $O_3$, $O_2$, $CO_2$, clouds and the surface, as well as scattering processes of clouds, gas-phase molecules, and the surface. Within the UIUC RTM, a narrow band terrestrial radiation (wave number between 0 and 3000 $cm^{-1}$) model calculates absorptivity and emissivity for $O_3$, $CH_4$ $CO_2$, and $N_2O$ at 10 $cm^{-1}$ resolution, and for $H_2O$, CFC-11 and CFC-12 at 5 $cm^{-1}$ resolution. Infrared spectra for these gases are from the HITRAN 2004 database, described in Rothman et al. (2005). Clouds, surface albedo, and surface emissivity are based on observation from the International Satellite Cloud Climatology Project.

Infrared spectra data for tCFP, HFO-1234yf, HFO-1234ze(Z), HFO-1234ze(E), HFO-1225ye(E), and HFO-1225ze(Z), reported respectively in Sulbaek Andersen et al. (2008), Nielsen et al. (2007), Sondergaard et al. (2007), Nilsson et al. (2009), Hurley et al. (2007) and Hurley et al. (2007) are regridded to 10 $cm^{-1}$ resolution and used in the UIUC RTM in this research.

**2.2. Hydrogen Economy Scenarios**

A set of emission scenarios for key species associated with a hydrogen economy is developed to evaluate possible impact of a hydrogen economy on the atmospheric environment. Emissions of a given species are often estimated based on emissions factors, which relate the emissions of a given pollutant to an activity, and the level of the activity. Thus projections of future emissions are based on projections of the change in the activity level and changes in the emissions factors. The activity factors include population, energy usage, and GDP. Since there are large uncertainties in projecting the change in each of these activities over time, there are also

relatively large uncertainties in the emissions estimates based on them. To bracket the possible evolution pathways of the future emissions, scenarios are based on the highest (A1FI) and lowest (B1) IPCC SRES emissions scenarios (IPCC, 2000). In the A1FI scenario, the world is assumed to evolve with rapid economic growth and rely intensively on fossil fuel; whereas in the B1 scenario the world's economic structures are projected to become more service and information intensive.

For each of these two IPCC growth scenarios (A1FI and B1), three emission scenarios with different technologies are further developed: 1) The Baseline (BL) scenario is the reference scenario for 2050 in which fossil fuel powered vehicles are still the dominant mode of road transportation. 2) The $H_2$ Fuel Cell ($H_2$-FC) scenario, in which the energy demands of the road transportation sector are met by $H_2$ fuel cell technology. In this scenario $H_2$ emissions due to leakage as well as reductions in combustion-related emissions of $H_2$, NOx, VOCs, CO, $SO_2$, and soot are included. 3) The $H_2$ Internal Combustion Engine ($H_2$-ICE) scenario, in which the energy demands of the road transportation sector are met by $H_2$ using internal combustion technology. In this scenario, $H_2$ emissions due to leakage as well as reductions in combustion-related emissions of $H_2$, VOCs, CO, $SO_2$ and soot are included; however, there are no reductions in NOx emissions because NOx is still a byproduct of internal combustion process (Deboer et al., 1976). For each IPCC scenario, an additional scenario, Baseline+$H_2$ (BL+$H_2$), is developed as well. In this scenario $H_2$ leakage emissions into the atmosphere was included but all other emissions remain the same as in the baseline scenario. This scenario, though not realistic, is designed as a sensitivity study which allows the evaluation of the impact of $H_2$ emission alone versus the impact of the reduction in ozone precursor emissions on tropospheric composition and chemistry.

The future baseline (BL) emissions are calculated by scaling the current fossil fuel combustion emissions by regionally dependent growth scale factors from the applicable IPCC scenario. The included species are $NO_x$, CO, $SO_2$ and several NMVOCs (non-methane VOCs), namely, $CH_2O$, $CH_3OH$, $CH_3CHO$, $C_2H_4$, $C_2H_6$, $C_2H_5OH$, $C_3H_6$, $C_3H_8$, $CH_3COCH_3$ (acetone), $C_4H_8O$ (methyl ethyl ketone), $C_4H_{10}$, $C_5H_8$ (isoprene), $C_{10}H_{16}$, BIGALK (lumped species for alkanes with four or more carbon atoms), BIGENE (lumped species for alkenes with four or more carbon atoms), and TOLUENE (lumped species for aromatic compounds). Emissions of these species are prepared from the Precursors of Ozone and their Effects in the Troposphere (POET) emissions dataset, which is based on version 3 of the Emission Database for Global Atmospheric Research (EDGAR) inventory (Olivier et al., 2003; Granier et al., 2005). This dataset represents the period between 1990 and 2000. Soot emissions are from Bond et al. (2004), derived from 1996 fuel-use data.

To estimate $H_2$ emissions from fossil fuel combustion, which are not included in the IPCC scenarios or POET, a $H_2$:CO mass emission factor of 0.03 and the corresponding CO emissions are used. There is a relatively large uncertainty in the $H_2$:CO mass emission ratio from fossil fuel use including automobile traffic. Estimates range from ~0.01 (Simmonds et al., 2000) to ~0.07 (Seiler and Zankl, 1975). Other estimates are 0.025-0.032 (Barnes et al., 2003) and 0.026-0.043 (Vollmer et al., 2007). For this study a mid-value of 0.03 is chosen and it is assumed that it remains constant over time.

In the scenarios involving $H_2$ technologies, $H_2$ emissions from leakage are estimated using a top-down approach based on a $H_2$ leakage rate and the amount of $H_2$ needed to meet the projected transportation energy demands in 2050. $H_2$ demand for road transportation is calculated assuming both the $H_2$-FC and the $H_2$-ICE vehicles would have comparable

efficiencies as fossil fuel vehicles in 2050 due to technology improvement, such that $H_2$-powered vehicles will consume the same amount of energy as that of the year 2050 "business-as-usual" fleet in the IPCC A1FI and B1 scenarios. Total $H_2$ demand is then calculated assuming a 120 MJ/kg energy density of hydrogen. Current estimates of the $H_2$ leakage rate are in the 1% to 4% range (e.g., Schultz et al., 2003, Colella et al., 2005). To date, there is no available observational data to provide a basis for estimating the leakage rate, as there is no massive $H_2$ infrastructure in large-scale use so far. Estimates in the literature span a large range. Tromp et al. (2003) postulated a leakage rate of 10~20%, resulting in quadrupling of atmospheric $H_2$ concentrations. However, it is argued in later studies (Schultz et al., 2003; Warwick et al., 2004) that this estimate was too high to be realistic. $H_2$ technologies would not be adopted unless leakage rate is brought down to commercially feasible level. Furthermore, such high leakage rate would raise safety concerns because of $H_2$ detonation risks. On the other hand, one can estimate $H_2$ leakage rate from that of natural gas (major component $CH_4$), which is commercially in operation in large-scale infrastructure, using Graham's law of effusion.

$$\frac{Rate_{H_2}}{Rate_{CH_4}} = \sqrt{\frac{MW_{CH_4}}{MW_{H_2}}} = \sqrt{\frac{16}{2}} = 2.83 \qquad \text{(Eq. 2.1)}$$

The leakage rate of natural gas with current infrastructure is ~1%. $H_2$ leakage rate estimated using Eq. 2.1 is 2.83. Schultz et al. (2003) suggests that it is prospective to bring $H_2$ leakage rate to 0.1% with technical advancement. In this research, a reasonable upper-limit $H_2$ leakage rate of 2.5%, estimated based a critical review of the related technology, is used in model simulations in order to evaluate the effect of a hydrogen economy on $H_2$ budget in the atmosphere. This estimate is in line with estimated leakage from natural gas production, supply and delivery systems. Knowledge of actual leakage rates, their dependence on technological

sophistication, and how they will change in the future is one of the key uncertainties in estimating future hydrogen leakage emissions. The total $H_2$ emissions for a given scenario are then obtained by replacing the road transportation $H_2$ emissions from fossil fuel combustion with the $H_2$ leakage emissions for the $H_2$ scenarios. $H_2$ leakage emissions are distributed according to current $CO_2$ road transportation emissions from the EDGAR emissions inventory with higher $H_2$ leakage emissions over more densely populated areas such as the eastern United States, Western Europe, parts of India and Eastern China.

For all of the $H_2$ scenarios (BL+ $H_2$, $H_2$-FC, and $H_2$-ICE) $H_2$ leakage emissions are included. In the $H_2$-FC scenarios, the road transportation emissions of $H_2$, CO, $NO_x$, NMVOCs, $SO_2$, and soot are removed from the total baseline (BL) emissions. In the $H_2$-ICE scenarios, the emissions of the same species as in the $H_2$-FC scenarios are reduced except for $NO_x$, which is still emitted with the ICE technology option.

Biomass burning emissions are from the Global Fire Emissions Database version 2 (GFED-v2) (van der Werf et al., 2006) and are assumed to remain at their 2000 levels as are emissions from other sources, e.g., ocean and biogenic emissions.

Annual global emissions of key species of current (2000) and 2050 (baseline and $H_2$ scenarios) are summarized in Figure 2.1. Global emissions increase in the 2050 A1FI baseline (A1FI BL) scenario for $H_2$ (42%), CO (35%), NMVOCs (28%), $NO_x$ (115%), $SO_2$ (10%), and soot (67%) relative to 2000. In the 2050 B1 baseline (B1 BL) scenario, global emissions decrease from 2000 for $H_2$ (19%), CO (10%), NMVOCs (6%), $SO_2$ (7%), and soot (12%); $NO_x$ emissions increase by 5%.

In the A1FI scenarios with a $H_2$ road transportation sector, global $H_2$ emissions increase by 81% relative to the 2050 A1FI baseline scenario, or increase by 157% from the 2000 emissions. Meanwhile, global emissions in the 2050 $H_2$-FC and $H_2$-ICE scenarios decrease for CO (25%), NMVOCs (14%), $NO_x$ (29% in $H_2$-FC; 0% in $H_2$-ICE), $SO_2$ (3%) and soot (17%), compared to the 2050 A1FI baseline scenario. If compared with the 2000 emissions, in a 2050 A1FI world with a $H_2$ road transportation sector emissions increase, for CO (1.6%), NMVOCs (10%), $NO_x$ (53% in $H_2$-FC), $SO_2$ (7%) and soot (39%), to a lesser extent than in the A1FI baseline scenario.

In the B1 scenarios with a $H_2$ road transportation sector, global $H_2$ emissions increase by 64% relative to the 2050 B1 baseline scenario, or increase by 33% from the 2000 emissions. Concurrently, global emissions in the 2050 $H_2$-FC and $H_2$-ICE scenarios decrease for CO (10%), NMVOCs (8%), $NO_x$ (24% in $H_2$-FC; 0% in $H_2$-ICE), $SO_2$ (3%) and soot (8%), compared to the 2050 B1 baseline scenario. If compared with the 2000 emissions, in a 2050 B1 world with a $H_2$ road transportation sector emissions decrease, for CO (19%), NMVOCs (13%), $NO_x$ (20% in $H_2$-FC), $SO_2$ (10%) and soot (19%), to a greater extent than in the B1 baseline scenario.

These emissions are input to the CAM-Chem and WACCM models as monthly varying maps at the model resolutions.

## 2.3. Figures

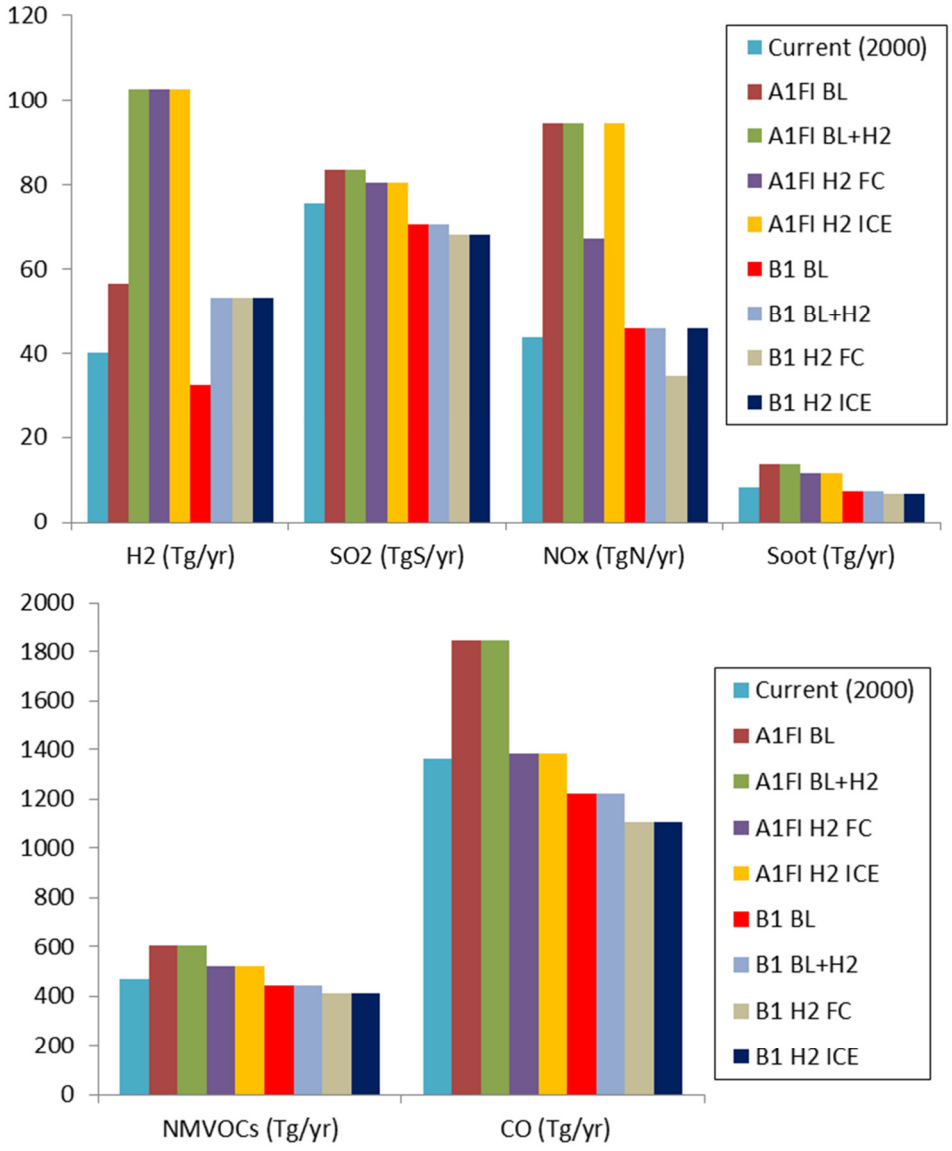


Figure 2.1. Global annual emissions of $H_2$, $SO_2$, $NO_x$, soot, NMVOCs and CO for the current (year 2000), and the Baseline (BL) , Baseline+$H_2$ (BL+$H_2$), $H_2$ Fuel Cell ($H_2$-FC), and $H_2$ Internal Combustion Engine ($H_2$-ICE) 2050 A1FI and B1 scenarios.

# CHAPTER 3: IMPACT OF A FUTURE HYDROGEN ECONOMY ON TROPOSPHERIC CHEMISTRY AND AIR QUALITY

This chapter describes and discusses the impacts of a hydrogen economy on tropospheric chemistry and air quality in details in the following sections, based on CAM-Chem model simulations. Air quality analyses based on high-resolution CMAQ simulations over the contiguous United States are also discussed in this chapter.

## 3.1. Molecular Hydrogen ($H_2$)

In all of the scenarios examined in this study, average tropospheric $H_2$ concentrations are greater in 2050 than they are in 2000. In the A1FI baseline scenario the annual average global mean concentration is 839 ppbv (Table 3.1). In this scenario the NH emissions are strong enough to offset the stronger soil sink in this hemisphere, leading to a reverse in the inter-hemispheric gradient, i.e., higher NH mean $H_2$ concentration (~850 ppbv) than SH (~830 ppbv). Annual-mean ground-level $H_2$ mixing ratios range from 720 ppbv to more than 1 ppmv (Figure 3.1a). Higher concentrations are located in highly urbanized and/or industrialized regions such as northeastern United States, California, Western Europe, Korea, Japan and eastern China, while lower concentrations appear over mid-latitude continents of the SH. The maximum/minimum pattern reflects the forcing of the $H_2$ emissions from human activities and the large $H_2$ microbial soil sink.

In the A1FI $H_2$ technology scenarios (BL+$H_2$, $H_2$-FC, and $H_2$-ICE), global mean $H_2$ concentrations increase substantially from the baseline scenario by ~40%, to up to ~1170 ppbv (Table 3.1). This increase is because the $H_2$ leakage emissions are much greater than the replaced fossil fuel $H_2$ emissions in the baseline scenario. In the $H_2$-FC scenario the south to north $H_2$

inter-hemispheric gradient is even larger than in the BL scenario (Figure 3.1b) since $H_2$ emissions increased more in the NH than in the SH due to the asymmetric intensity of road transportation activities between the hemispheres. The background surface $H_2$ mixing ratio increases by at least 40% in the NH and by at least 35% in the SH, reaching about 1.2 ppmv in the NH and 1.15 ppmv in the SH. The highest $H_2$ concentrations (greater than 1.6 ppmv) are in eastern China and Korea, corresponding to a greater than 75% increase from the baseline scenario. $H_2$ concentrations increase by approximately 50% in northeastern United States. The largest increase (~45%) in zonal-average $H_2$ concentration occurs in the boundary layer in the northern hemisphere mid-latitudes where road transportation activities are concentrated. The spatial distributions of the $H_2$ concentrations in the BL+$H_2$ and $H_2$-ICE scenarios (not shown) are nearly identical to those in the $H_2$-FC scenario. The geographical pattern of relative increase in surface $H_2$ concentrations in this scenario is similar to that calculated by Schultz et al. (2003) even though they assumed a leakage rate of 3% and their calculation is for the year 2000 atmosphere. However, the increase in eastern Asia is comparatively larger in this study because of the projected significant economic development in this region by 2050.

In the B1 baseline scenario the average tropospheric $H_2$ mixing ratio is 621 ppbv (Table 3.2), and the annual-mean ground-level $H_2$ concentration is ~600 ppbv (Figure 3.1c). The inter-hemispheric gradient is of the same direction as in the current atmosphere with higher background $H_2$ concentrations in the SH. Since human activities that emit $H_2$ are not as intensive as in the A1FI scenario, there are few regions bearing significantly higher than background value, except the northeastern United States, where $H_2$ concentrations are around 650 ppbv.

In the B1 $H_2$ scenarios (BL+$H_2$, $H_2$-FC, and $H_2$-ICE) the tropospheric $H_2$ burden increases by ~20%, corresponding to a mean tropospheric concentration of 740 ppbv. In the $H_2$-FC

scenario (the other two are quite similar), surface $H_2$ concentrations in remote regions increase from the BL scenario by more than 20% in the NH and by more than 15% in the SH (Figure 3.1d), leading to a slightly higher $H_2$ concentration in the NH, a reverse in the inter-hemispheric gradient. Maximum $H_2$ mixing ratios (860 ppbv) occur in eastern Asia, corresponding to a more than 40% increase from the baseline scenario.

### 3.2. Ozone ($O_3$)

The annual average tropospheric ozone concentration is 44 ppbv in the 2050 A1FI BL scenario, higher than the 2000 value of 39 ppbv (IPCC, 2001), due to increased precursor emissions. The summertime (June, July, and August) average surface ozone concentrations over land in the A1FI BL scenario are projected to be mostly above 40 ppbv (Figure 3.2a). Summertime ozone concentrations are highest near densely populated areas, such as the eastern United States, California, the Middle East, and eastern China. In the A1FI $H_2$-FC scenario, surface ozone mixing ratios decrease by more than 5% around the world, with as much as 20% decrease in Latin America and Southeast Asia (Figure 3.2b). In heavily polluted areas surface ozone mixing ratios are about 10% lower than those in the BL scenario. However, ozone increases in some localized populated areas in eastern China, Korea, and London, UK. In these regions ozone production is VOC-limited, hence decreasing both $NO_x$ and VOC emissions, as in this $H_2$ fuel cell case, does not effectively decrease ozone. While the changes in ozone extend throughout the troposphere, the largest changes occur near the surface (Figure 3.3). In the A1FI $H_2$-FC scenario, zonally-averaged summertime ozone mixing ratios are at least 5% lower than in the BL scenario in the lower troposphere (Figure 3.3b). The maximum decrease (more than 10%) appears in the boundary layer at the low latitudes of the NH (centered at around 15°N).

In the A1FI $H_2$-ICE scenario summertime surface ozone concentrations are virtually unchanged over most of the globe (Figure 3.2c). The relatively modest decreases occur over limited regions, such as England and Korea, which tend to include the highly localized regions where ozone increased in the $H_2$ fuel cells scenario. The zonally-averaged ozone concentrations do not change significantly except in the lower troposphere of the northern middle latitudes, where ozone decreases by as much as 5% (Figure 3.3c).

In the 2050 B1 BL scenario, the average tropospheric ozone concentration is ~37 ppbv, slightly lower than the current value, due to slightly decreased precursor emissions (except $NO_x$ which slightly increases). The distribution pattern of the summertime surface ozone concentrations over the world is similar to that for the corresponding A1FI scenarios, but the concentrations are 10-20 ppbv lower than those in the A1FI BL scenario (Figures 3.2d, 3.3d). In the B1 $H_2$-FC scenario, summertime near surface ozone decreases significantly (by 10% to 30%) (Figures 3.2e, 3.3e) along the coasts of the United State, making them considerably lower than current $O_3$ concentrations. Ozone reductions in the B1 $H_2$-ICE scenario are not as apparent (Figures 3.2f, 3.3f) except the same sensitive areas as in the A1FI $H_2$-ICE scenario, where relative reductions are no more than 15%.

The simulation results of the CMAQ model over the contiguous United States is consistent with the global model results in general; however, due to its finer resolution, CMAQ is capable of capturing some of the finer features of the ozone concentrations. For example, while CAM-Chem predicts that the highest summertime ozone concentrations appear in California and the Midwest, CMAQ predicts higher maximum daily 8-hour average ozone concentrations near population centers and along the west and east coasts with a plume extending off the east coast (Figures 3.4a,d). Over the southwestern United States and parts of the East

Coast, daily maximum 8-hour average $O_3$ concentrations at surface are projected to exceed the U.S. EPA National Ambient Air Quality Standards (NAAQS) of 75 ppbv over much of the summertime for the A1FI BL scenario. In contrast, concentrations are in compliance with the NAAQS (below ~56 ppbv) for the vast majority of the time for the B1 BL scenario.

Relatively large decreases in daily maximum 8-hour $O_3$ concentrations are noted with the adoption of the $H_2$-FC scenarios. For both the A1FI and B1 scenarios the decreases are largest over the population centers (Figures 3.4b,e). The decreases in summertime $O_3$ concentrations are nearly 18 ppbv for A1FI and 12 ppbv for the B1 scenario respectively. In stark contrast to these decreases for the $H_2$-FC scenario there is little decrease in daily maximum 8-hour $O_3$ concentrations for the $H_2$-ICE scenario over vast majority of the United States (Figures 3.4e,f). There are some relatively small reductions over the Los Angeles and San Francisco regions of California and a few very localized spots in the Midwest but these reductions are much less significant than in the $H_2$-FC scenario.

In the A1FI $H_2$-FC scenario the population of the United States would experience considerably fewer days above the 75 ppb limit than in the baseline scenario (Figure 3.5). Here an analysis of time cumulated population exposure to levels of ambient ozone is performed using population data from the 2000 U.S. census (http://www.esri.com/data/download/census2000-tigerline/index.html) and assuming the population distribution has not changed significantly in 2050. There is a large shift towards lower $O_3$ concentrations for the $H_2$-FC scenarios for both the A1FI and B1 scenarios (Figure 3.5). In the A1FI scenario much of the large tail area above 75 ppbv is reduced and compliance with the ozone air quality standard is much more frequent (Figure 3.5). While the improvements for the $H_2$-FC scenarios are quite impressive, the $H_2$-ICE scenario provides almost no noticeable improvement. The distributions are extremely similar

except for a small reduction in the over 75 ppbv tail. In the B1 scenarios (Figure 3.5) the standard is rarely exceeded in any scenario, but still there are substantial improvements with the adoption of a fuel cell powered road sector.

The scenarios examined in this study suggest that summertime $O_3$ over the contiguous United States is predominantly $NO_x$ controlled, suggesting the importance of the utilization of non-combustion technologies, e.g., fuel cells, in which $NO_x$ emissions are voided, in a $H_2$-based road transportation sector towards improving $O_3$ air quality.

### 3.3. The Tropospheric Oxidizing Capacity (OH) and Climate Implication

As discussed in Sect 1, utilization of $H_2$ raises concern over its potential impact on the oxidizing capacity of the troposphere. The model simulations show that adoption of a $H_2$-based road transportation sector can either decrease or increase the tropospheric OH abundance, depending on the technology option selected.

The tropospheric mean OH abundance changes from the 2000 modeled value of $9.7 \times 10^5$ molecules/cm$^3$ to $9.1 \times 10^5$ molecules/cm$^3$ in the 2050 A1FI baseline scenario (Table 3.1), mainly a result of the projected increase in CO emissions and $CH_4$ concentration in this scenario despite that the modeled tropospheric $O_3$ concentration increases. In contrast, the tropospheric mean OH abundance increases to $10.1 \times 10^5$ molecules/cm$^3$ in the B1 baseline scenario (Table 3.2) due to the projected decreased CO emissions in this scenario.

The sensitivity study of the BL+$H_2$ scenarios suggests that $H_2$ leakage emission itself from a $H_2$-based road transportation sector can have some impact on tropospheric OH abundance, assuming a leakage rate of 2.5%. The mean tropospheric OH abundance decreases by

2% and 1% in the A1FI and B1 scenarios, respectively, from the baseline scenarios (Tables 3.1, 3.2). The reductions in OH abundance mainly occur in the tropical troposphere (Figures 3.6a,d).

The combined effect of $H_2$ leakage emission and reductions in ozone precursor emission in the A1FI and B1 $H_2$-FC scenarios is a 4% decrease in the mean tropospheric OH abundance (Tables 3.1, 3.2). The largest OH abundance reduction is in the tropical boundary layer and extends to the middle troposphere (Figures 3.6b,e). However, the OH abundance increases in the remote troposphere at high-latitudes in the NH as a result of its decreased sink against CO, as CO concentrations decrease there.

In the $H_2$-ICE scenarios the tropospheric OH abundance would actually increase by 7% for the A1FI scenario and by 3% for the B1 scenario (Tables 3.1, 3.2) despite the increased atmospheric $H_2$ concentrations, which reduce OH abundance by 2%. This is likely because $O_3$ initiated OH production is not severely affected in these scenarios while the OH sink through reactions with CO and other fossil fuel combustion byproducts is significantly reduced. The tropospheric OH abundance increases by 10% and by 3% in the NH and in the SH, respectively, in the A1FI $H_2$-ICE scenario (Figure 3.6c), whereas it increases by 5% and by 1% in the NH and in the SH, respectively in the B1 $H_2$-ICE scenario (Figure 3.6f). Evidently the effect of the $H_2$ economy on global OH is relatively small for the scenarios examined here and can be positive or negative with relatively minor contributions to atmospheric chemistry and climate forcing as discussed next.

### *3.3.1. Impact on $CH_4$ Lifetime and Climate*

Since the reaction with OH is the primary sink of $CH_4$, changes in the OH abundance have direct impacts on the atmospheric $CH_4$ lifetime. Here the $CH_4$ lifetime was calculated by

dividing the $CH_4$ tropospheric burden by its sink against OH. A companion run of the current atmosphere estimates $CH_4$ lifetime to be 8.7 years, well within the 8~10 years range summarized by IPCC (2007). The baseline $CH_4$ lifetime is 9.1 years for the A1FI scenario and 8.3 years for the B1 scenario. In the 2050 $H_2$-FC scenarios the $CH_4$ lifetimes increased by 7% to 9.7 years for the A1FI scenario and by 6% to 8.8 years in the B1 scenario. However, in the $H_2$-ICE scenarios the $CH_4$ lifetime decreased by 4% to 8.7 years in the A1FI scenario and by 2% to 8.1 years in the B1scenario. These changes imply that transitioning to a $H_2$ fuel cell type road transportation sector may exacerbate climate warming due to $CH_4$ through its increased lifetime. However, the amount of warming due to $CH_4$ will depend on its actual atmospheric concentrations which will depend on many factors including how any transition to a $H_2$ economy occurs and changes in other, e.g., biogenic, $CH_4$ emissions which have not been evaluated here.

It is interesting to investigate the combined climate effects of a $H_2$-based road transportation sector in terms of both changes in $CH_4$ lifetime and changes in $O_3$ concentration. In the $H_2$-FC scenarios, the decrease in tropospheric ozone concentrations, which implies a cooling effect, is accompanied by increase in $CH_4$ lifetime, which implies a warming effect. The two effects tend to offset each other, but the effect is inhomogeneous because tropospheric ozone is short-lived and is thus not uniform, whereas $CH_4$ is long-lived and uniform. The changes in aerosol loadings, especially for soot and sulfate, would further complicate the combined climate effect problem of the $H_2$-FC scenarios.

Whereas in the $H_2$-ICE scenarios, both tropospheric ozone concentration and $CH_4$ lifetime are decreased, implicating a negative radiative forcing. Taking soot reductions enhances this cooling effect while reductions of sulfate aerosols would counteract it. Again, it is interesting to investigate the climate effect of the $H_2$-ICE scenarios because of its inhomogeneity.

### 3.4. Nitrogen Oxides ($NO_x$)

The tropospheric $NO_x$ burden depends on the type of $H_2$ technology option selected. In the $H_2$-FC scenarios tropospheric $NO_x$ concentrations are reduced significantly, by 16% in the A1FI scenario and by 11% in the B1 scenario (Tables 3.1, 3.2). In the $H_2$-ICE scenarios, however, tropospheric $NO_x$ concentrations increase by 10% in the A1FI scenario and by 3% in the B1 scenario.

Regions with intense human activities, such as eastern China, India, northeastern United States, and Western Europe, have high $NO_x$ concentrations in the baseline scenarios (Figures 3.7a,d). These regions would benefit substantially from $NO_x$ reductions in the A1FI $H_2$-FC scenario. Annual mean ground-level $NO_x$ concentrations decrease considerably along the coasts of North and South America, Western Europe, North Africa, the Middle East, New Zealand, and Japan (Figure 3.7b) with relative reductions as high as 80%. Although some remote areas have large relative changes, for example much of the remote Southern Hemisphere, the absolute changes are quite small there, as the baseline $NO_x$ mixing ratio is rather low. The relative reductions are most pronounced in wintertime, when the boundary layer height is lower and ventilation is inhibited. In the B1 $H_2$-FC scenario, the reduction in $NO_x$ concentrations occurs in the same regions, but the percentages are about half of those in the A1FI scenario (Figure 3.7e).

In the A1FI and B1 $H_2$-ICE scenarios the simulated surface $NO_x$ concentration change is not apparent in the $NO_x$ pollution areas (Figures 3.7c,f), showing that the internal combustion engine type of $H_2$ society would not be as effective in ground-level $NO_x$ mitigation.

As in the global CAM-Chem simulations the CMAQ model results show that higher $NO_x$ concentrations tend to appear in wintertime, so here analysis is focused on the wintertime

(February) changes. $NO_x$ peaks are concentrated in the northeastern United States and in locations in the west, e.g., Los Angeles and Bay areas of California (Figures 3.8a,d). Wintertime concentrations are higher than summertime concentrations and concentrations are higher in the A1FI than B1 scenarios. There are large decreases in $NO_x$ concentrations with the adoption of a $H_2$ fuel cell transportation sector (Figures 3.8b,e), up to ~13 ppbv (~50%) in winter over the northeast United States for the A1FI scenario. However, for the $H_2$-ICE scenario there is almost no change in wintertime $NO_x$ concentrations evident (Figures 3.8c,f).

### 3.5. Carbon Monoxide (CO)

The tropospheric CO burdens decrease by 14% and 18% for the A1FI $H_2$-FC and $H_2$-ICE scenarios respectively, and by 4% and 7% for the B1 $H_2$-FC and $H_2$-ICE scenarios respectively (Tables 3.1, 3.2).

In the A1FI baseline scenario, annual mean surface CO concentrations over North America and Eurasia exceed 200 ppbv (Figure 3.9a). Higher values are present in the northeastern U.S., Central Europe and Eastern China. There are also higher than background concentrations in the tropics due to biomass burning. In the B1 baseline scenario, annual mean surface CO concentrations over the NH continents are over 100 ppbv (Figure 3.9b). Higher concentrations are seen in eastern China, northeastern U.S., and tropical regions.

In the A1FI $H_2$-FC scenario, surface CO concentrations in remote areas of the NH decrease by at least 20% (Figure 3.9b). Relative CO concentration reductions in the $H_2$-FC scenario are largest in hotspots of human activities, such as northeastern U.S., California, central and western Europe, eastern China, South Korea and Japan. Concentrations in New York City decrease by as much as 80%. The CO mitigation is perennial but is most pronounced in winter.

In the $H_2$-ICE scenario the ground-level CO concentration reduction pattern is similar to that in the A1FI $H_2$-FC scenario, but the magnitude of reduction is even larger (Figure 3.9c), due to ~11% higher OH concentrations in the A1FI $H_2$-ICE scenario than the A1FI $H_2$-FC scenario. This is a result of the increase in atmospheric oxidizing capacity in the $H_2$ internal combustion engine scenarios which will lead to decreases in species that react with OH, e.g., CO and other VOC.

In the B1 $H_2$-FC and $H_2$-ICE scenarios, the background CO concentrations in the NH decrease by 10~20% relative to the baseline scenario (Figures 3.9d,e,f). The largest relative reduction (up to 50%) appears over northeastern United States. There is also a 30% decrease in Western Europe. The relative and absolute CO decreases in B1 $H_2$ scenarios are smaller than those in the corresponding A1FI scenarios.

The regional U.S. CMAQ simulations are consistent with the CAM-Chem global simulations with 2050. Baseline CO concentrations are generally highest over the east coast in wintertime with monthly average wintertime concentrations of greater than 400 ppbv and 150 ppbv over much of the Eastern part of the United States in the A1FI and B1 scenarios respectively (Figures 3.10a,d). However, analysis shows that there is no violation of CO NAAQS, that is, 8-hr average not to exceed 9 ppmv and 1-hr average not to exceed 35 ppmv more than once per year, in any of the scenarios examined. In the $H_2$-FC and $H_2$-ICE scenarios there are large decreases in CO concentrations due to the decrease in CO emissions. The largest decreases occur over areas with the highest emissions in the baseline case and, in contrast to some other pollutants, there are only slight differences between the $H_2$-FC and $H_2$-ICE scenarios. Wintertime CO decreases are nearly 280 ppbv and 100 ppbv for the A1FI and B1 scenarios over polluted regions, corresponding to decreases over much of the east coast of greater than 60%

(figures 3.10b,c,e,f). Summertime decreases are nearly half as large as wintertime decreases (not shown) because the wintertime planetary boundary layer is shallower, there is less vigorous vertical mixing, and chemical loss is lower.

### 3.6. Aerosols

In the $H_2$-FC scenarios, tropospheric aerosols, especially soot, sulfate aerosols and ammonium nitrate concentrations are significantly reduced as a result of emissions decreases. In the $H_2$-ICE scenarios, tropospheric soot and sulfate aerosol concentrations decrease while ammonium nitrate aerosol concentrations increase due to the $NO_x$ concentration increase.

In CAM-Chem $PM_{2.5}$ includes sulfate aerosol, nitrate aerosol, black carbon, organic carbon, secondary organic aerosol, and dust and sea salt aerosol with diameter no larger than 2.5 μm. Since emission changes have little impact on dust and sea salt aerosol, these types of aerosol are excluded in following discussion of $PM_{2.5}$.

Figures 3.11a and 3.11d show the CAM-Chem simulated annual mean surface $PM_{2.5}$ concentrations in the A1FI and B1 BL scenarios, repectively. In the A1FI BL scenario, eastern China is subject to high $PM_{2.5}$ concentrations of more than 100 $\mu g/m^3$. Surface $PM_{2.5}$ concentrations can be as high as 50 $\mu g/m^3$ in northern India and parts of Indonesia. In central Europe near ground $PM_{2.5}$ concentrations reach 30 $\mu g/m^3$. In the eastern United States surface $PM_{2.5}$ concentrations are 10~20 $\mu g/m^3$. Annual mean surface $PM_{2.5}$ concentrations in the B1 BL scenario (Figure 3.11d) are generally lower than those in the A1FI BL scenario. In central Europe and eastern United States it is ~10 $\mu g/m^3$ lower, whereas in eastern China it can be ~50 $\mu g/m^3$ lower than in the A1FI BL scenario.

In the A1FI $H_2$-FC scenario, annual mean surface $PM_{2.5}$ concentrations are significantly reduced in eastern China and northern India, by up to 10 $\mu g/m^3$ (Figure 3.11b). In northeastern United States and Europe, $PM_{2.5}$ concentrations are reduced by 1-3 $\mu g/m^3$. In the A1FI $H_2$-ICE scenario, surface $PM_{2.5}$ concentrations reductions in the northeastern United States, India and Europe are not as significant as in the A1FI $H_2$-FC scenario, whereas the reductions in eastern China is comparable to the A1FI $H_2$-FC scenario (Figure 3.11c).

In the B1 $H_2$-FC scenario, there are only a few locations having annual mean surface $PM_{2.5}$ concentrations reductions of more than 1 $\mu g/m^3$ (Figure 3.11e). The maximum reduction of ~5 appears in eastern China. In the B1 $H_2$-ICE scenario, surface $PM_{2.5}$ concentrations reductions are even less significant as in the B1 $H_2$-FC scenario. Higher reductions are only seen in eastern China (Figure 3.11f).

Again, the regional U.S. CMAQ simulations are consistent with the global CAM-Chem simulations but with more localized peaks due to their higher resolution. In the A1FI and B1 baseline scenarios the only location in the contiguous U.S. exceeding the annual mean $PM_{2.5}$ NAAQS (15 $\mu g/m^3$) is around Buffalo, NY. In the $H_2$-FC and $H_2$-ICE scenarios in both the A1FI and B1 scenarios, annual mean $PM_{2.5}$ concentration in Buffalo, NY decreases, but it is still above the NAAQS.

$PM_{2.5}$ concentrations are typically higher in winter than in summer. For the baseline A1FI and B1 scenarios, highest $PM_{2.5}$ concentrations over the contiguous United States appear generally along the Ohio River Valley and the East Coast (Figures 3.12a,d). February average surface concentrations peak at roughly 9 $\mu g/m^3$ for the A1FI scenario and around 8 $\mu g/m^3$ for the B1 scenario. As with $O_3$, improvements in $PM_{2.5}$ air quality depend on the technology adoption

scenario. $PM_{2.5}$ reductions are greatest with the $H_2$-FC scenarios' $NO_x$ and VOC emissions reductions while the reductions are much more modest with the VOC only emissions reductions of the $H_2$-ICE scenario. While the areas of largest absolute decrease correspond to the areas of highest initial concentrations the areas of largest relative decrease are typically over areas with lower initial concentrations in the Midwest and west coast. For the $H_2$-FC scenario there are reductions of ~1.5 $\mu g/m^3$ and ~1 $\mu g/m^3$ for the A1FI and B1 scenarios in February over the regions of high concentration in the Midwest (Figures 3.12b,e). For the $H_2$-ICE scenario reductions are much more modest at around 1 and 0.5 $\mu g/m^3$ for the A1FI and B1 scenarios, respectively, and more concentrated on the eastern seaboard (Figures 3.12c,f). The smaller $PM_{2.5}$ reduction in the $H_2$-ICE scenarios is primarily due to the impact of nitrate aerosol $PM_{2.5}$ production from the $NO_x$ emissions, whereas in the $H_2$-FC scenario there are reductions in soot, sulfate, and nitrate aerosols as well as secondary organic aerosol formation from decreases in VOC emissions.

The changes in annual mean surface $PM_{10}$ concentrations (not shown) are the same as those for $PM_{2.5}$, because the diameters of the aerosol reduced are less than 2.5 $\mu m$ in the CAM-Chem simulation. The following sections discuss the aerosol components that are significantly reduced.

*3.6.1. Soot*

In the baseline scenarios soot (black carbon) concentrations at the surface are rather low in remote regions (less than 1 $\mu gC/m^3$) (Figures 3.13a,d). It is nearly absent in the air of pristine regions (concentrations less than 0.1 $\mu gC/m^3$). In the tropics soot concentrations are higher due to biomass burning. Densely populated regions are plagued with soot pollution from intense fossil fuel combustion activities. These regions include eastern China, Europe, North America,

Korea, Japan, and India. The worst pollution occurs in eastern China, where annual mean soot concentration can be up to more than 10 $\mu gC/m^3$ in the A1FI BL scenario.

The tropospheric soot burden would decrease by 17% and 7% in the A1FI and B1 scenarios, respectively (Tables 3.1, 3.2), both in the $H_2$-FC and the $H_2$-ICE scenarios. Ground-level soot would be significantly reduced in most of the United States, Europe, and Japan (Figures 3.13b,c,e,f). In the A1FI scenario a $H_2$-based road transportation sector reduces surface soot concentrations by as much as 50% in the United States and Western Europe (Figure 3.13b). Soot concentrations are also reduced by 30~40% in the North Atlantic Ocean region and other regions downwind of key polluted areas. There is also significant relative reduction (~20%) of soot in eastern China. The pattern of surface soot concentration reduction is almost identical in the A1FI $H_2$-ICE scenario to that in the A1FI $H_2$-FC scenario (Figure 3.13c). In the B1 scenarios soot reductions in the $H_2$-FC and $H_2$-ICE scenarios are 10-20% less than in the corresponding A1FI scenarios, but they are still significant reductions and bear similar pattern (Figures 3.13e,f).

Soot is a warming climate agent (IPCC, 2001), though there remain uncertainties in quantitative understandings. Reductions of tropospheric soot, as in with a $H_2$-based road transportation sector, would have cooling effect on climate. This effect would be inhomogeneous in space since the reduction is not uniform.

*3.6.2. Sulfate aerosols*

Sulfate aerosols ($SO_4$) are associated with human activities (Figures 3.14a,d). The highest annual mean surface concentrations (~10 $\mu gSO_4/m^3$) are seen in eastern China, India, and Mexico in the A1FI BL scenario. In the B1 BL scenario, sulfate aerosol pollution in these densely populated areas is slightly less severe than in the A1FI BL scenario.

The tropospheric sulfate aerosol burdens decrease by 4% for both the A1FI and B1 $H_2$-FC scenarios (Tables 3.1, 3.2). In the A1FI $H_2$-FC scenario, surface $SO_4$ mass concentrations decrease by approximately 5% around the world. Higher reductions of ~10% occur in southern California, Southeast Asia and New Zealand (Figure 3.14b). The increase in Antarctica is not significant as the background sulfate aerosol concentration is extremely small there (less than 0.1 µg $SO_4/m^3$) (Figures 3.14a,d).

The tropospheric sulfate aerosol burdens decrease by 3% for the two $H_2$-ICE scenarios. In the A1FI $H_2$-ICE scenario, there is around 10%-15% decrease in $SO_4$ mass concentration over most Eurasia, North Africa, western United States, Mexico, and South America (Figure 3.14c). The $H_2$-ICE scenario is slightly less powerful than $H_2$-FC scenario in $SO_4$ mitigation (Figure 3.14f) because the former has greater oxidizing power, which makes the oxidation of $SO_2$ to sulfate aerosols faster than in the latter scenario.

*3.6.3. Ammonium nitrate*

In 2050 as today annual mean surface ammonium nitrate aerosols ($NH_4NO_3$) concentrations are higher in regions with intense human activities, such as, the northeastern United States, Europe and eastern China and India (Figures 3.15a,d). The highest annual mean surface concentrations (~10 µg/$m^3$) are seen in eastern China and India in the A1FI BL scenarios. Surface ammonium nitrate aerosols concentrations are slightly lower in the B1 BL scenarios than in the A1FI.

The tropospheric ammonium nitrate aerosol burdens decrease by 12% and by 9% in the A1FI and B1 $H_2$-FC scenarios, respectively (Tables 3.1, 3.2). In the A1FI $H_2$-FC scenario, surface concentrations decrease significantly around the world. Concentrations decrease by as

much as 80%, for example in California (Figure 3.15b). Reductions are nearly as significant in the B1 $H_2$-FC scenario as in the A1FI $H_2$-FC scenario in terms of percent change (Figure 3.15e).

The tropospheric ammonium nitrate aerosol burdens increase by 3% and by 2% in the A1FI and B1 $H_2$-ICE scenarios, respectively (Tables 3.1, 3.2). Surface concentrations increase in remote regions (Figures 3.15a,d) as a result of the increased $NO_x$ concentrations there (see Section 4.4). In the A1FI $H_2$-FC scenario, there are slight concentration reductions (~10%) in Ohio River Valley and in eastern China (Figure 3.15b). The relative increase in remote regions is not significant as the background concentration is extremely small there (less than 0.1 $\mu g/m^3$) (Figures 3.15a,d).

### 3.7. Conclusions

The possible impacts of transitioning to a $H_2$ powered road transportation sector in 2050 are evaluated using atmospheric chemistry-climate models and emissions scenarios based on the IPCC A1FI and B1 SRES growth scenarios and fuel cell and internal combustion engine technology options. The model simulation results show that air quality would improve significantly with adoption of a $H_2$ fuel cell type road transportation sector ($H_2$-FC scenarios). Primary gaseous (CO, $NO_x$) and particulate (soot) pollutants are reduced substantially once the fossil fuel based road transportation sector transitions to $H_2$ fuel cells. Ozone, a major secondary pollutant that often exceeds air quality standards in some regions of the United States (and is a severe problem in developing countries), would be reduced to a significant extent as its precursors, CO, $NO_x$ and NMVOCs emissions are reduced. Additionally, concentrations of particulate matter, especially those with diameter less than 2.5 $\mu m$ ($PM_{2.5}$) would be significantly reduced in densely populated regions.

Some aspects of air quality would also improve with application of a $H_2$ internal combustion engine type road transportation sector ($H_2$-ICE scenarios). Ambient ozone concentrations would decrease slightly as its precursor emissions by fossil fuel combustion from road transportation sector are eliminated. Ozone mitigation with the $H_2$-ICE option is not nearly as effective as in the $H_2$-FC scenarios but is somewhat more effective in the relatively few VOC-limited regions. Urban $PM_{2.5}$ concentrations would not be significantly reduced except in eastern China.

For each specific type of $H_2$ technology applied in the road transportation sector, the reductions of key air pollution species are not as significant in the B1 scenario as in the A1FI scenario. However, since the emissions of key ozone and aerosol precursors are lower in the B1 scenarios, air quality in the B1 scenarios is generally better than that in the A1FI scenarios. For example, tropospheric ozone concentrations are substantially lower in all of the B1 scenarios than in all of the A1FI scenarios regardless of the $H_2$ technology adopted.

With a leakage rate of 2.5%, $H_2$ emissions in a $H_2$-based road transportation sector are larger than the replaced $H_2$ emissions from fossil fuel burning, leading to increased $H_2$ concentrations in the atmosphere. The added $H_2$ would decrease tropospheric OH abundance, resulting in elongated $CH_4$ lifetime and thus warming. However, when taking changes in emissions of CO, $NO_x$ and NMVOCs into account, the picture of the climate impact is more complicated. In the $H_2$-FC scenarios, the combined effect of emission changes is a 4% decrease in OH abundance, which contributes to warming by increasing $CH_4$ lifetime. On the other hand, concurrent decrease in tropospheric $O_3$ concentrations would provide a cooling mechanism. The overall effect is further complicated by the temporal and spatial inhomogeneity of the two offsetting mechanisms. In the $H_2$-ICE scenarios, both decrease in $CH_4$ lifetime due to OH

increase and the decrease in tropospheric $O_3$ tend to cool the climate while, again, inhomogeneities in space and time would complicate the problem.

It is worth noting that the emission scenarios are assumed 100% market penetration of $H_2$ technologies in 2050. That is, all vehicles operating on road are replaced with $H_2$ powered ones. It is also assumed that the $H_2$ for road transportation is produced by renewable, nuclear, or fossil fuel facilities with advanced scrubbing technologies with no emissions associated with its production. The positive and negative impacts presented here will decrease in magnitude to the extent that market penetration is not total and if there are emissions associated with $H_2$ production.

## 3.8. Figures and Tables

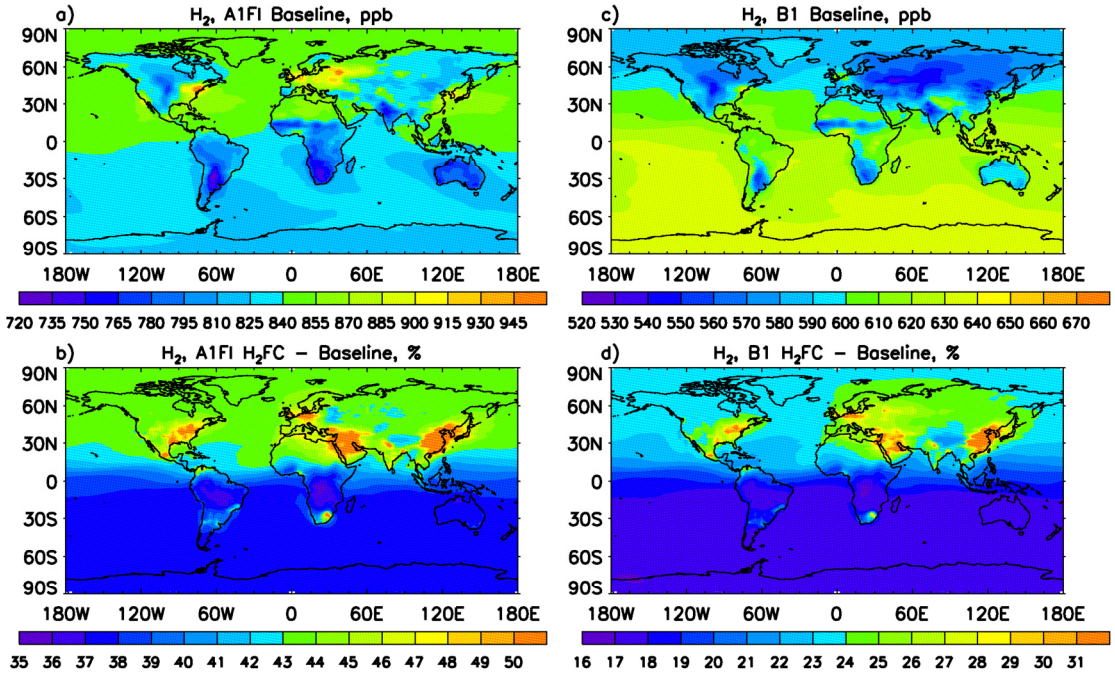


Figure 3.1 CAM-Chem simulated 2050 annual-mean ground-level $H_2$ mixing ratios in the A1FI (a) and B1 (c) Baseline scenarios and the percent differences for the A1FI (b) and B1 (d) $H_2$-FC scenarios. Note the different scales.

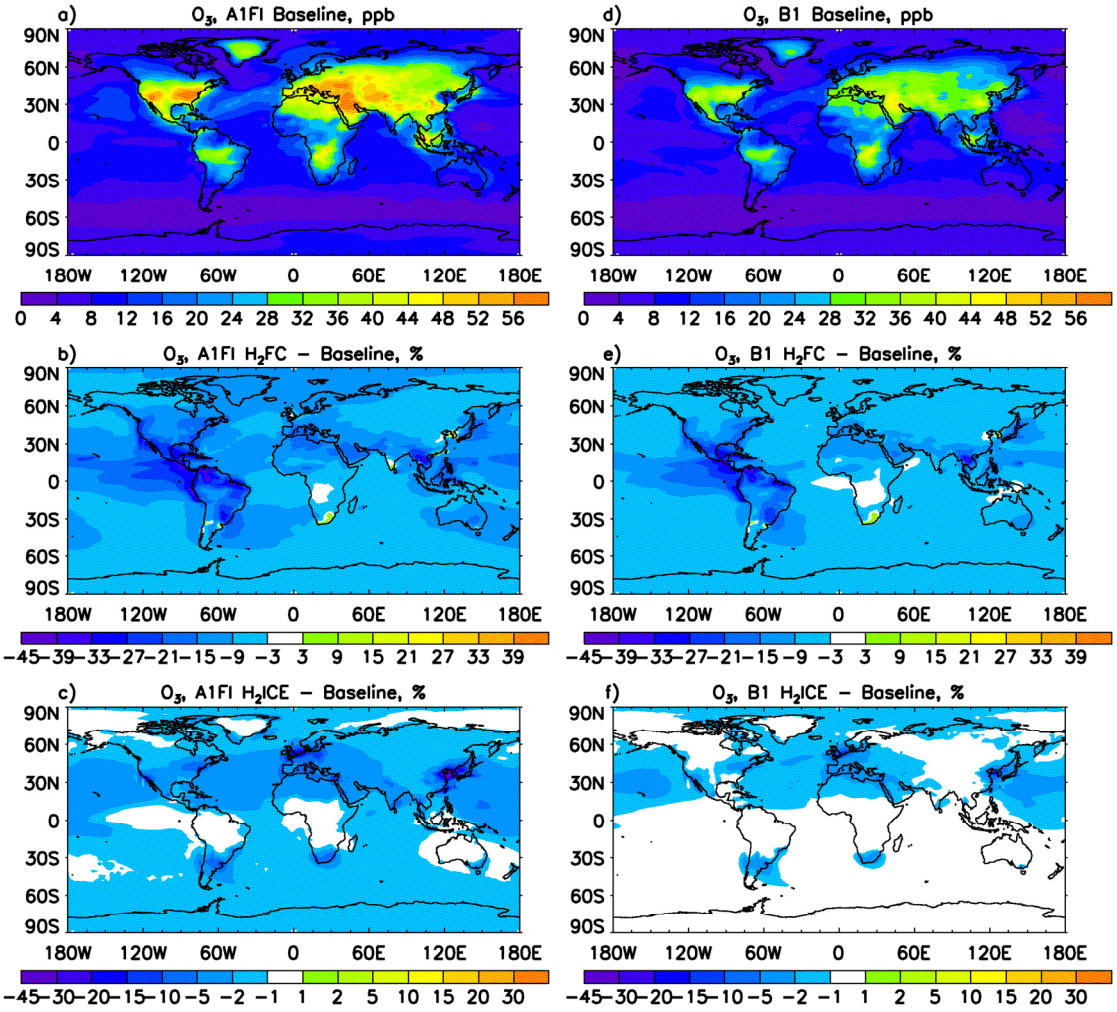


Figure 3.2 CAM-Chem simulated 2050 summertime (June, July, and August) average ground-level $O_3$ mixing ratios in the A1FI (a) and B1 (d) Baseline scenarios and percent differences for the $H_2$ Fuel Cell ($H_2$-FC) and $H_2$ Internal Combustion Engine ($H_2$-ICE) scenarios (b, c, e and f). Note the different scales.

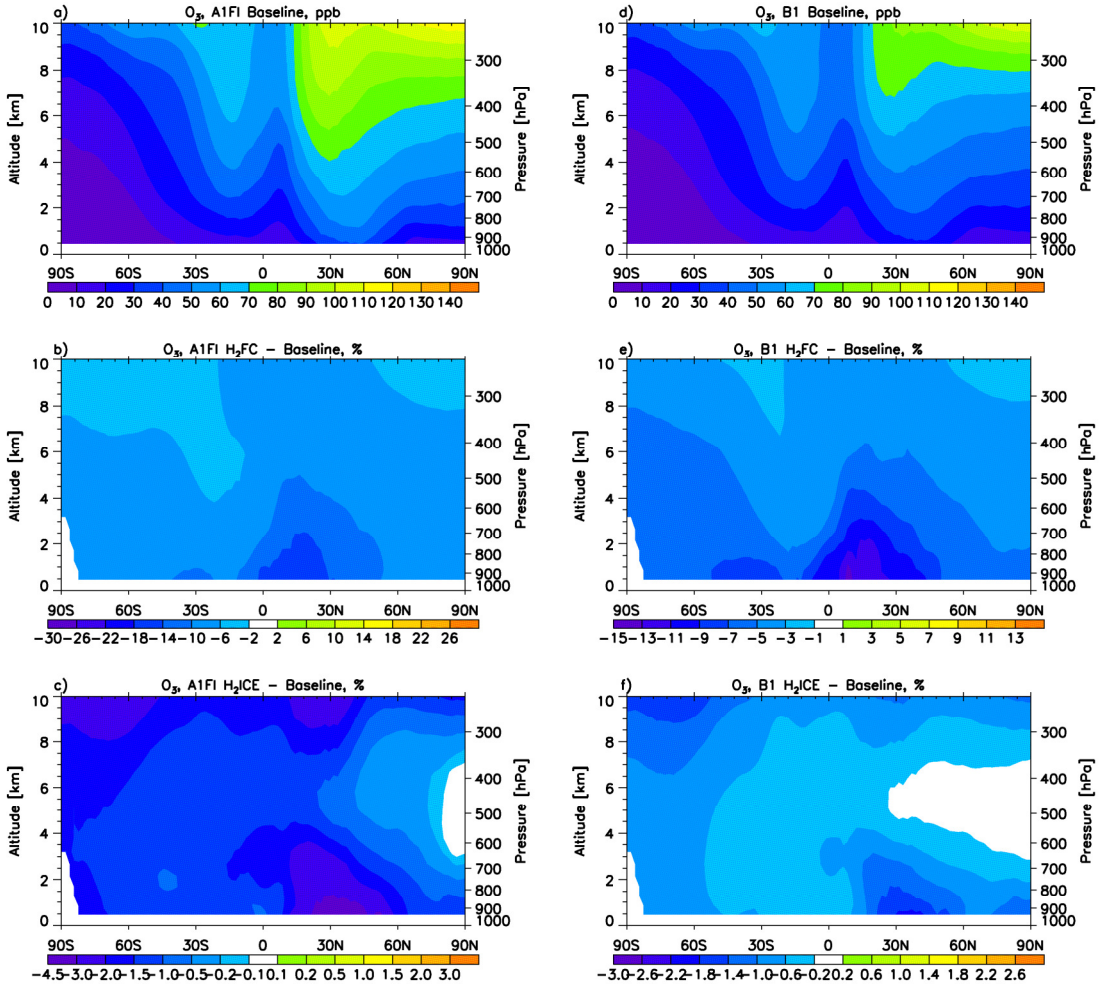


Figure 3.3 CAM-Chem simulated 2050 summertime (June, July, and August) average zonal-mean $O_3$ mixing ratios in the A1FI (a) and B1 (d) Baseline scenarios and percent differences for the $H_2$ Fuel Cell ($H_2$-FC) and $H_2$ Internal Combustion Engine ($H_2$-ICE) scenarios (b, c, e and f). Note the different scales.

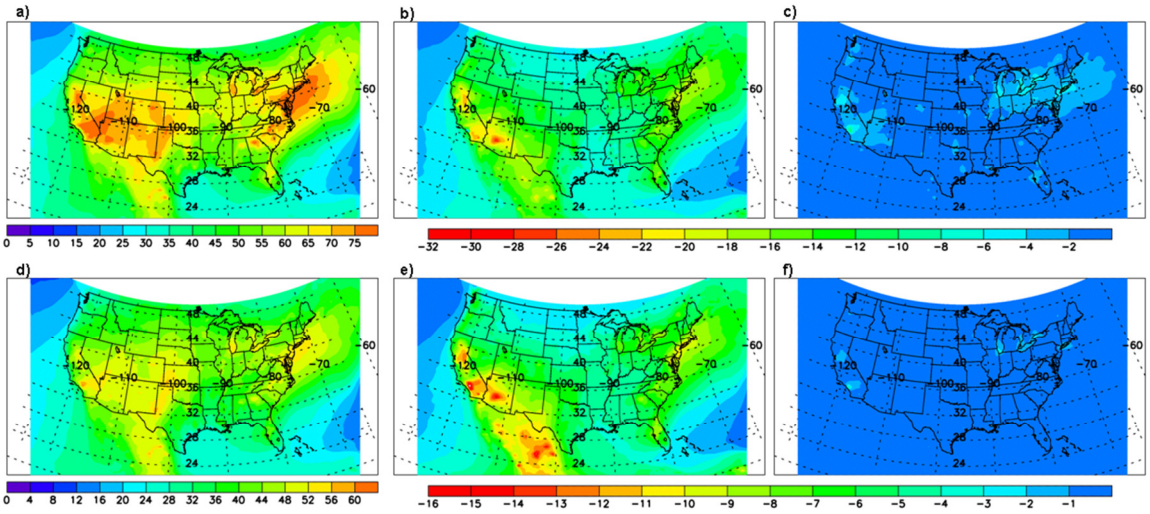


Figure 3.4 July 2050 averages of the daily maximum 8-hour-average $O_3$ concentrations simulated by CMAQ for the A1FI (top) and B1 scenarios (bottom). Each row contains the Baseline scenarios (left: a and d), differences between the Baseline and $H_2$ Fuel Cell ($H_2$-FC) scenarios (center: b and e), and differences between the Baseline and $H_2$ Internal Combustion Engine ($H_2$-ICE) scenarios (right: c and f). Data are averaged over the lowest model level (~100 m). Note that the scales are different among panels.

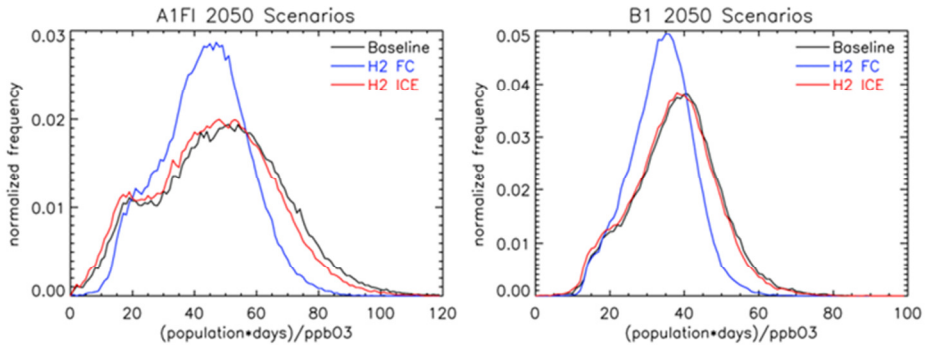


Figure 3.5 Normalized probability distribution [population*days/ppb] of CMAQ simulated surface daily maximum 8-hour-average $O_3$ concentrations throughout one year for the A1FI (left) and B1 (right) Baseline, $H_2$-ICE, and $H_2$-FC scenarios across the United States. Distributions are based on the U.S. population distribution for 2000 and the bin interval is 1 ppbv.

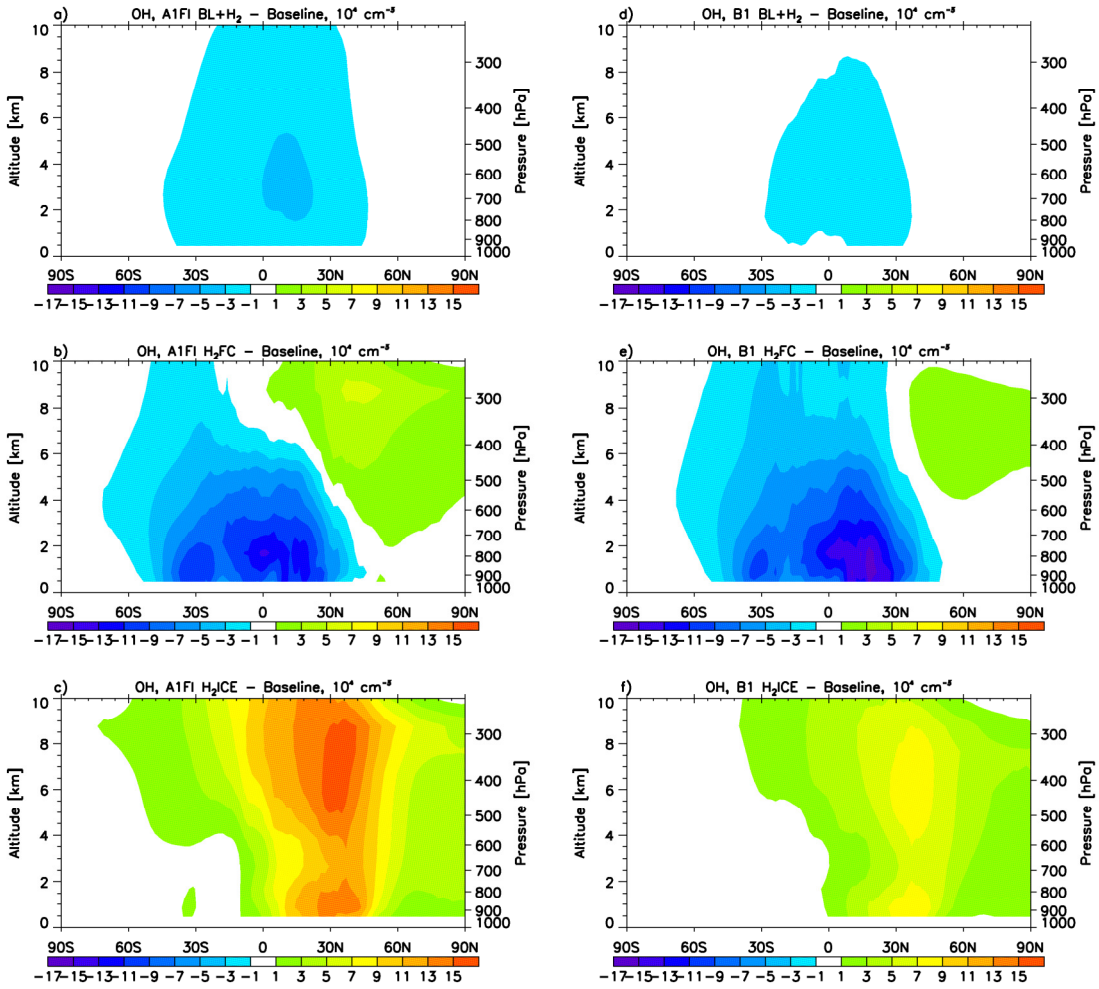


Figure 3.6 CAM-Chem simulated 2050 annual averaged zonal-mean OH abundance differences in the $H_2$ BL+$H_2$, $H_2$-FC, and $H_2$-ICE scenarios from the corresponding BL scenarios ($10^{-4}$ $cm^{-3}$). Note the different scales.

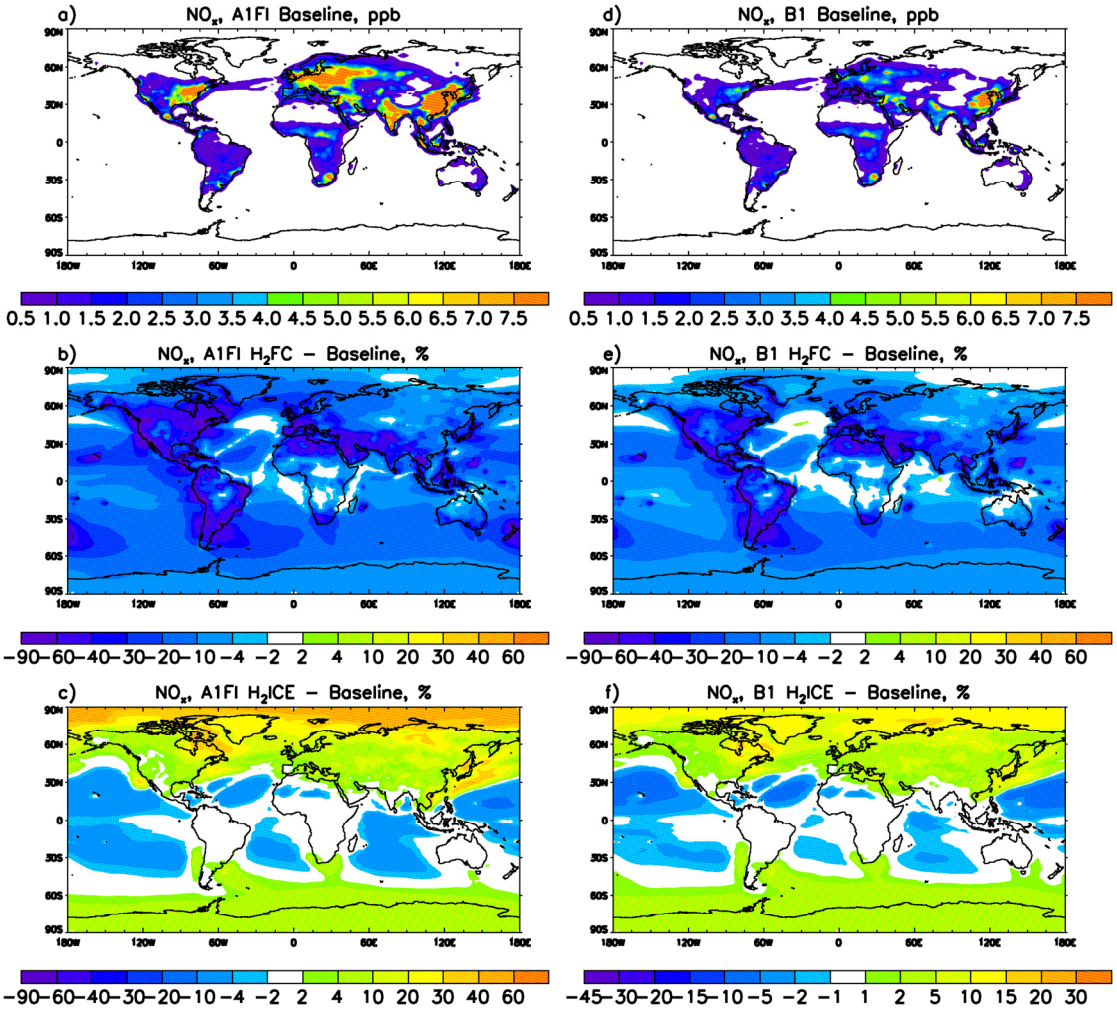


Figure 3.7 CAM-Chem simulated 2050 annual mean surface $NO_x$ mixing ratios in the A1FI (a) and B1 (d) Baseline scenarios and percent differences for the $H_2$ Fuel Cell ($H_2$-FC) and $H_2$ Internal Combustion Engine ($H_2$-ICE) scenarios (b, c, e and f). Note the different scales.

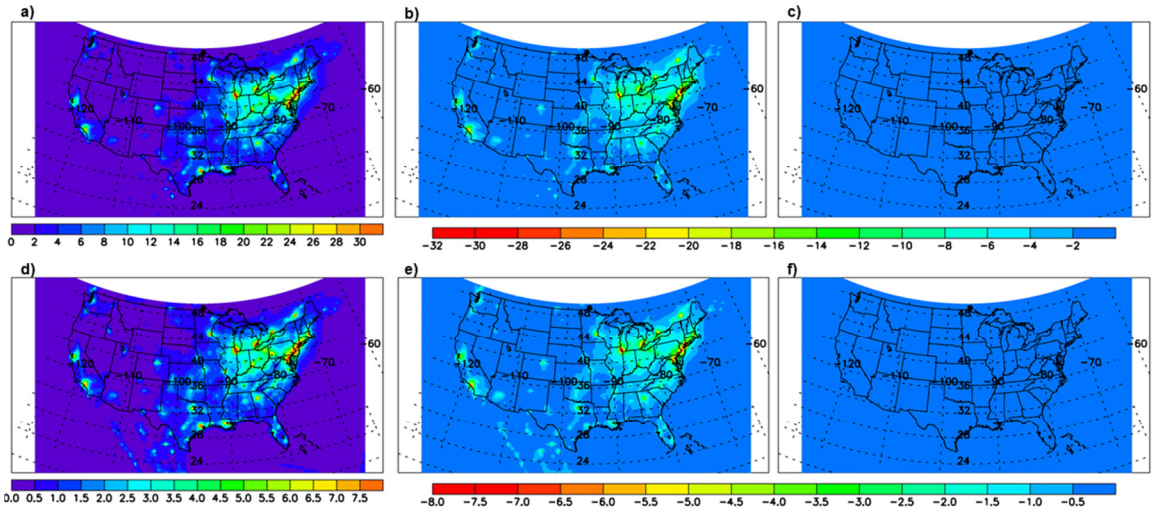


Figure 3.8 February 2050 average $NO_x$ concentrations (ppbv) simulated by CMAQ for the A1FI (top) and B1 scenarios (bottom). Each row contains the BL scenarios (left: a and d), differences (ppbv) between the BL and $H_2$-FC scenarios (center: b and e), and differences (ppbv) between the BL and $H_2$-ICE scenarios (right: c and f). Data are averaged over the lowest level (~100 m). Note that the scales are different among panels.

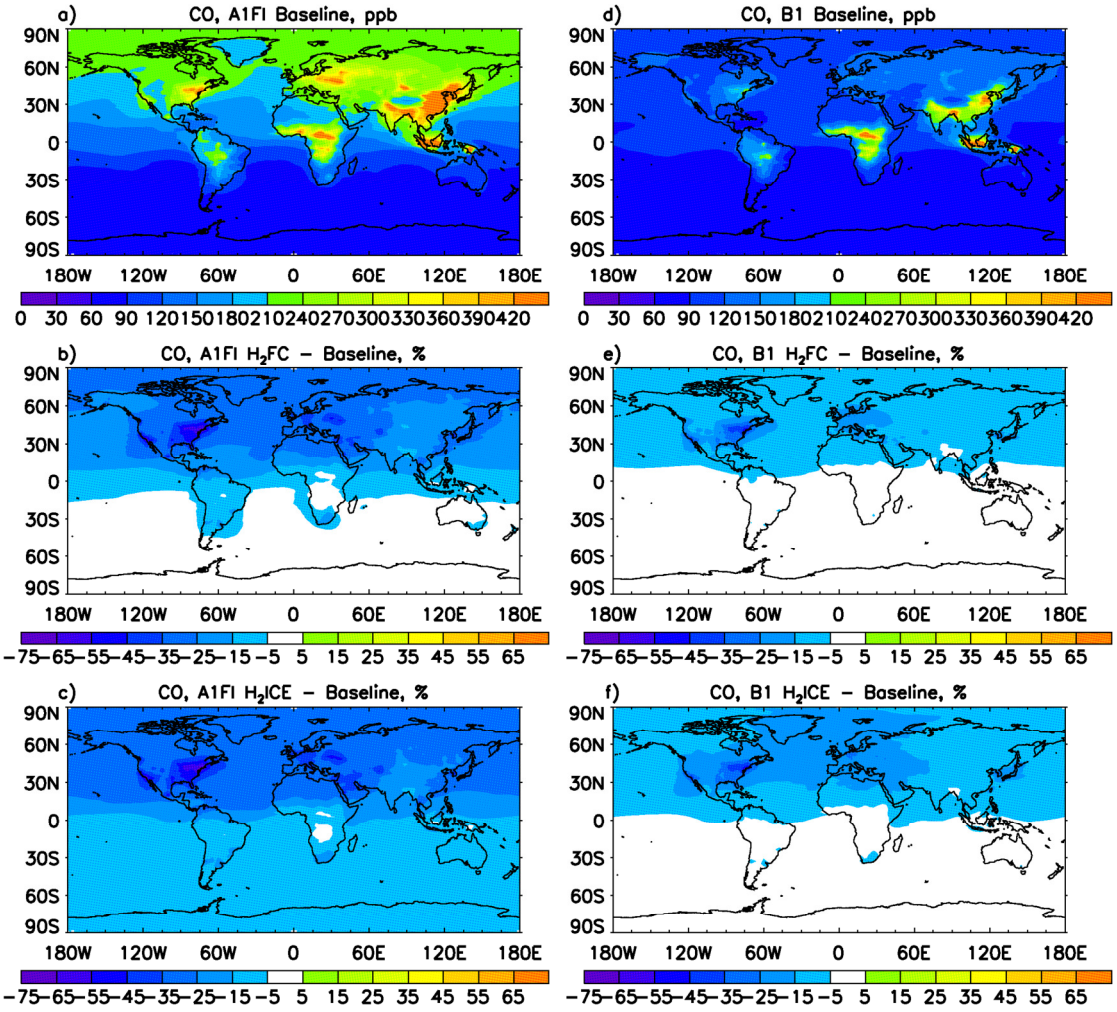


Figure 3.9 CAM-Chem simulated 2050 annual mean surface CO mixing ratios in the A1FI (a) and B1 (d) Baseline scenarios and percent differences for the $H_2$ Fuel Cell ($H_2$-FC) and $H_2$ Internal Combustion Engine ($H_2$-ICE) scenarios (b, c, e and f). Note the different scales.

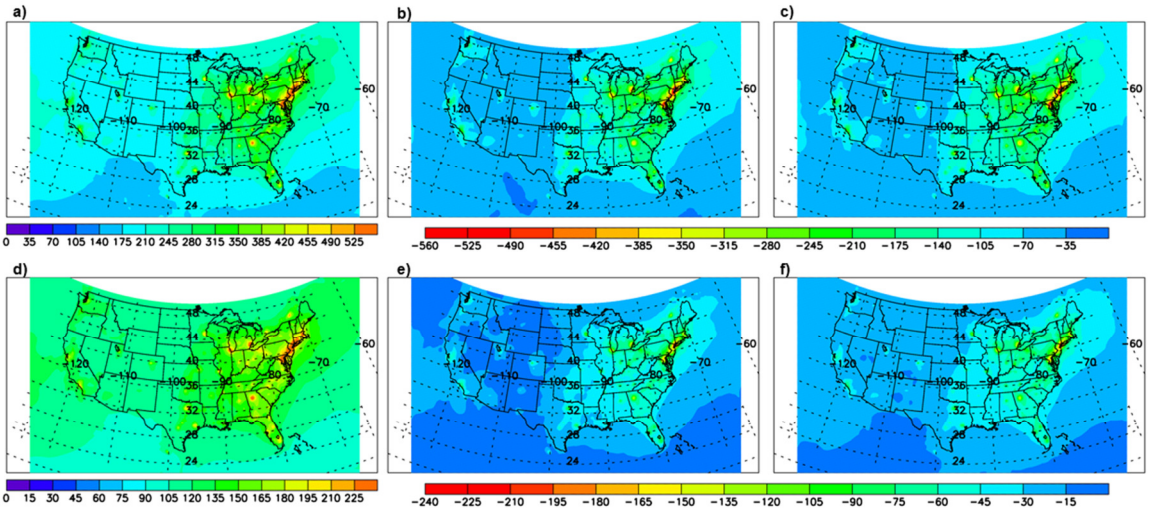


Figure 3.10 February 2050 averages CO concentrations (ppbv) simulated by CMAQ for the A1FI (top) and B1 scenarios (bottom). Each row contains the BL scenarios (left: a and d), differences (ppbv) between the BL and $H_2$-FC scenarios (center: b and e), and differences (ppbv) between the BL and $H_2$-ICE scenarios (right: c and f). Data are averaged over the lowest level (~100 m). Note that the scales are different among panels.

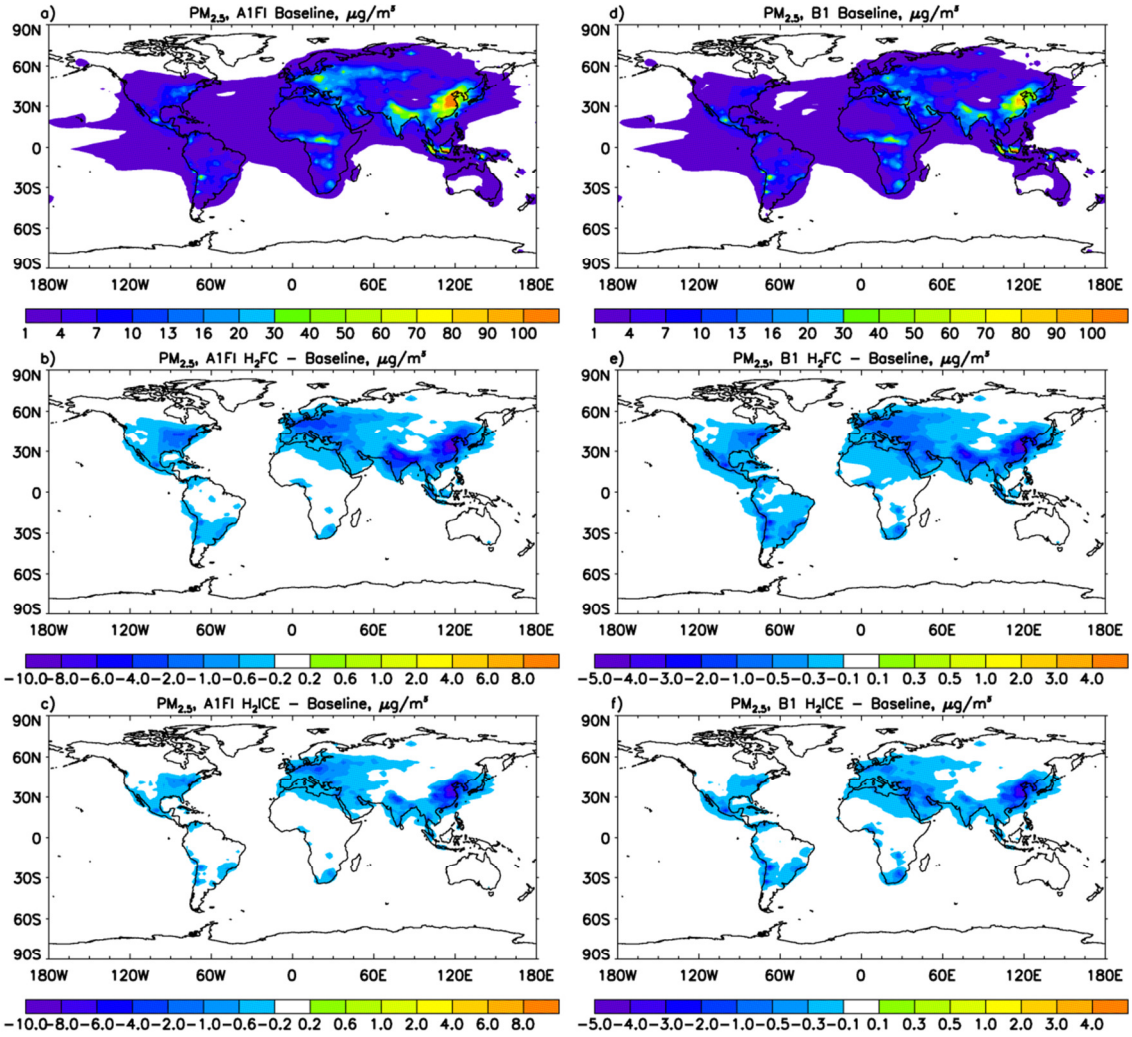


Figure 3.11 CAM-Chem simulated 2050 annual mean surface non-dust $PM_{2.5}$ concentrations in the A1FI (a) and B1 (d) Baseline scenarios and differences for the $H_2$ Fuel Cell ($H_2$-FC) and $H_2$ Internal Combustion Engine ($H_2$-ICE) scenarios (b, c, e and f). Note the different scales.

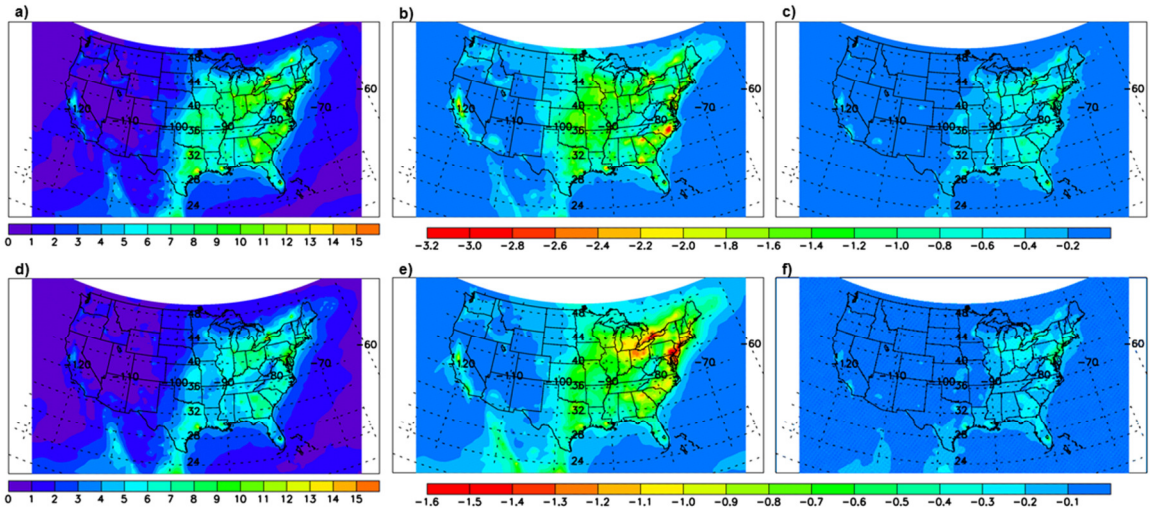


Figure 3.12 February 2050 average $PM_{2.5}$ concentrations ($\mu g/m^3$) simulated by CMAQ for the A1FI (top) and B1 scenarios (bottom). Each row contains the BL scenarios (left: a and d), differences ($\mu g/m^3$) between the BL and $H_2$-FC scenarios (center: b and e), and differences ($\mu g/m^3$) between the BL and $H_2$-ICE scenarios (right: c and f). Data are averaged over the lowest level (~100 m). Note that the scales are different among panels.

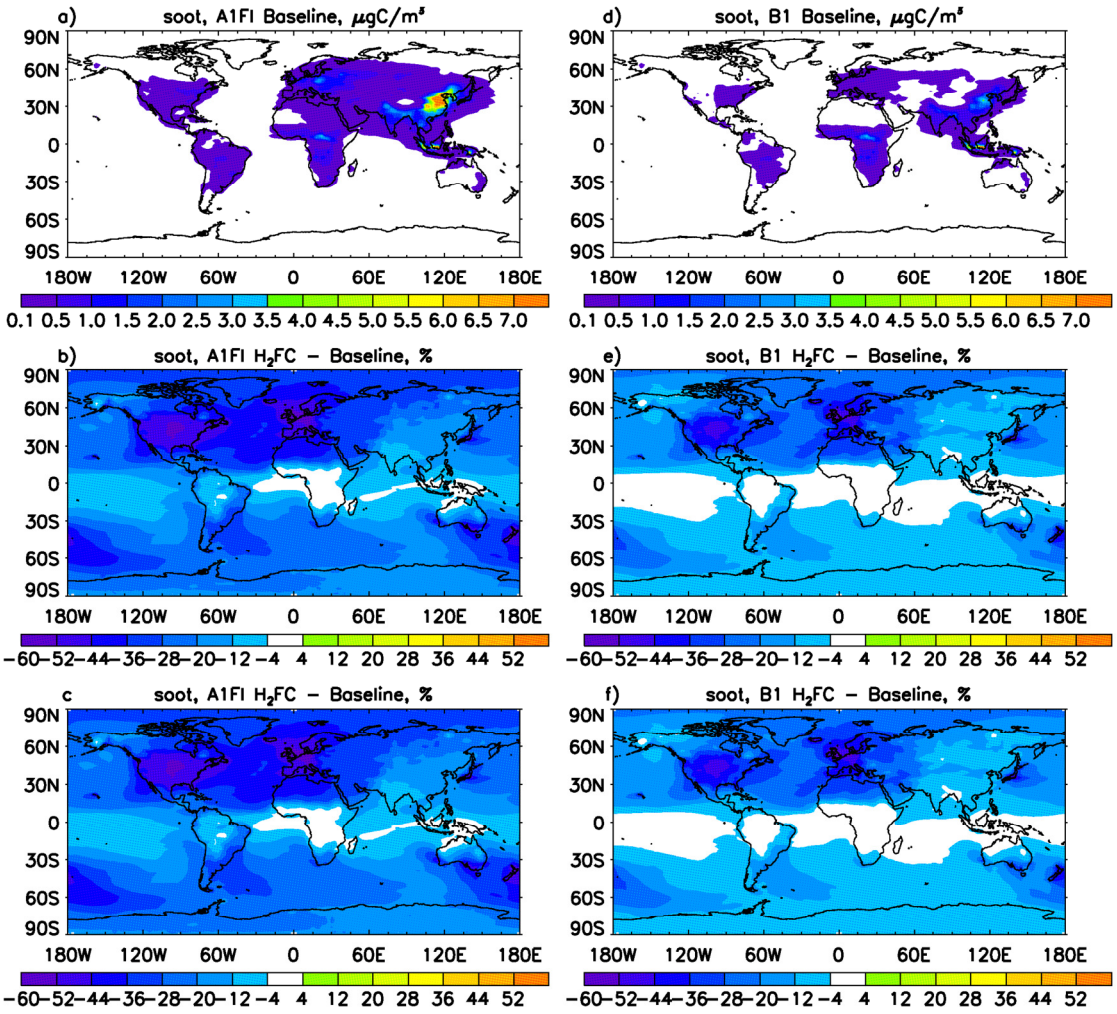


Figure 3.13 CAM-Chem simulated 2050 annual mean surface soot concentrations in the A1FI (a) and B1 (d) Baseline scenarios and percent differences for the $H_2$ Fuel Cell ($H_2$-FC) and $H_2$ Internal Combustion Engine ($H_2$-ICE) scenarios (b, c, e and f).Note the different scales.

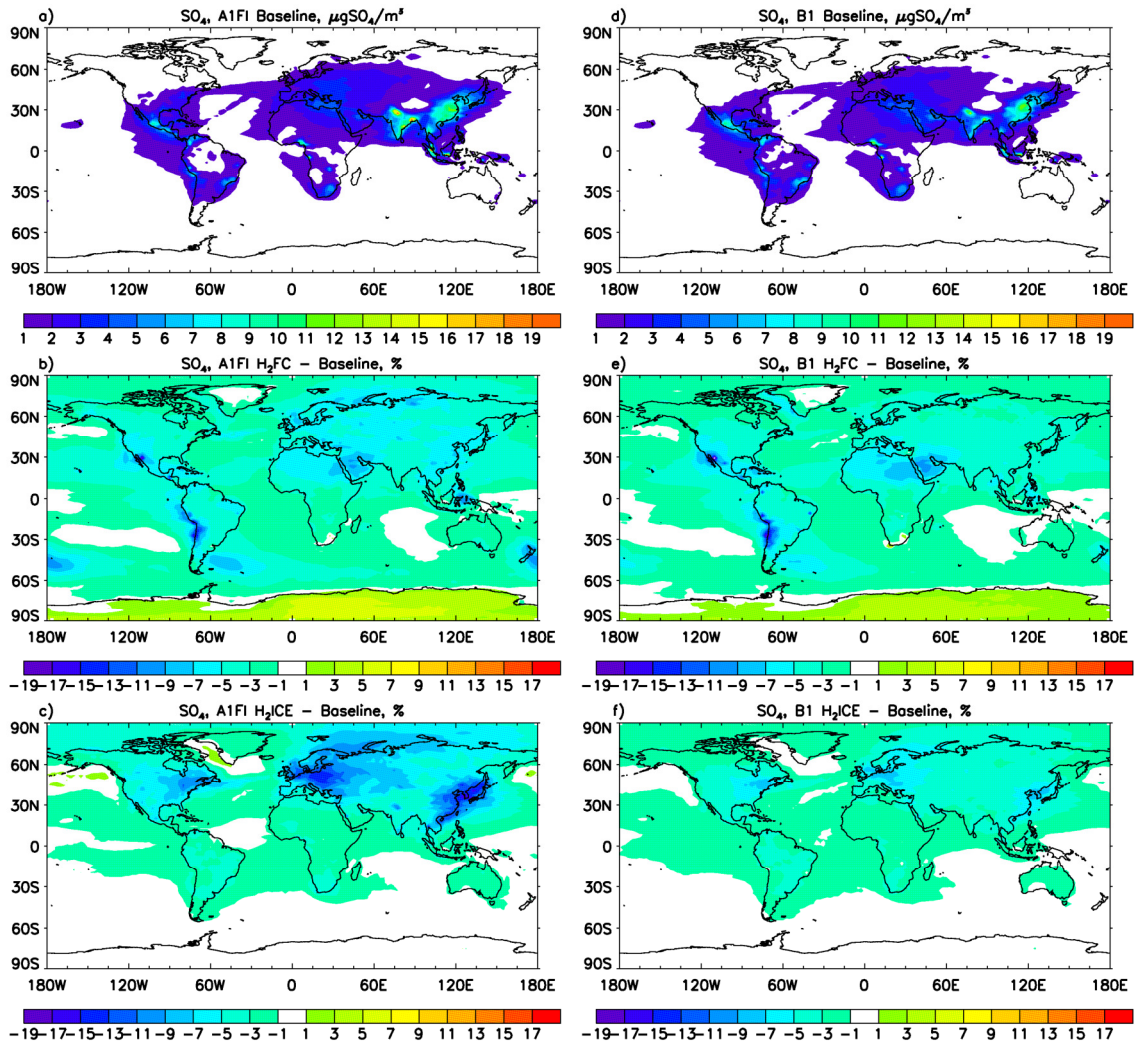


Figure 3.14 CAM-Chem simulated 2050 annual mean surface $SO_4$ concentrations in the A1FI (a) and B1 (d) Baseline scenarios and percent differences for the $H_2$ Fuel Cell ($H_2$-FC) and $H_2$ Internal Combustion Engine ($H_2$-ICE) scenarios (b, c, e and f). Note the different scales.

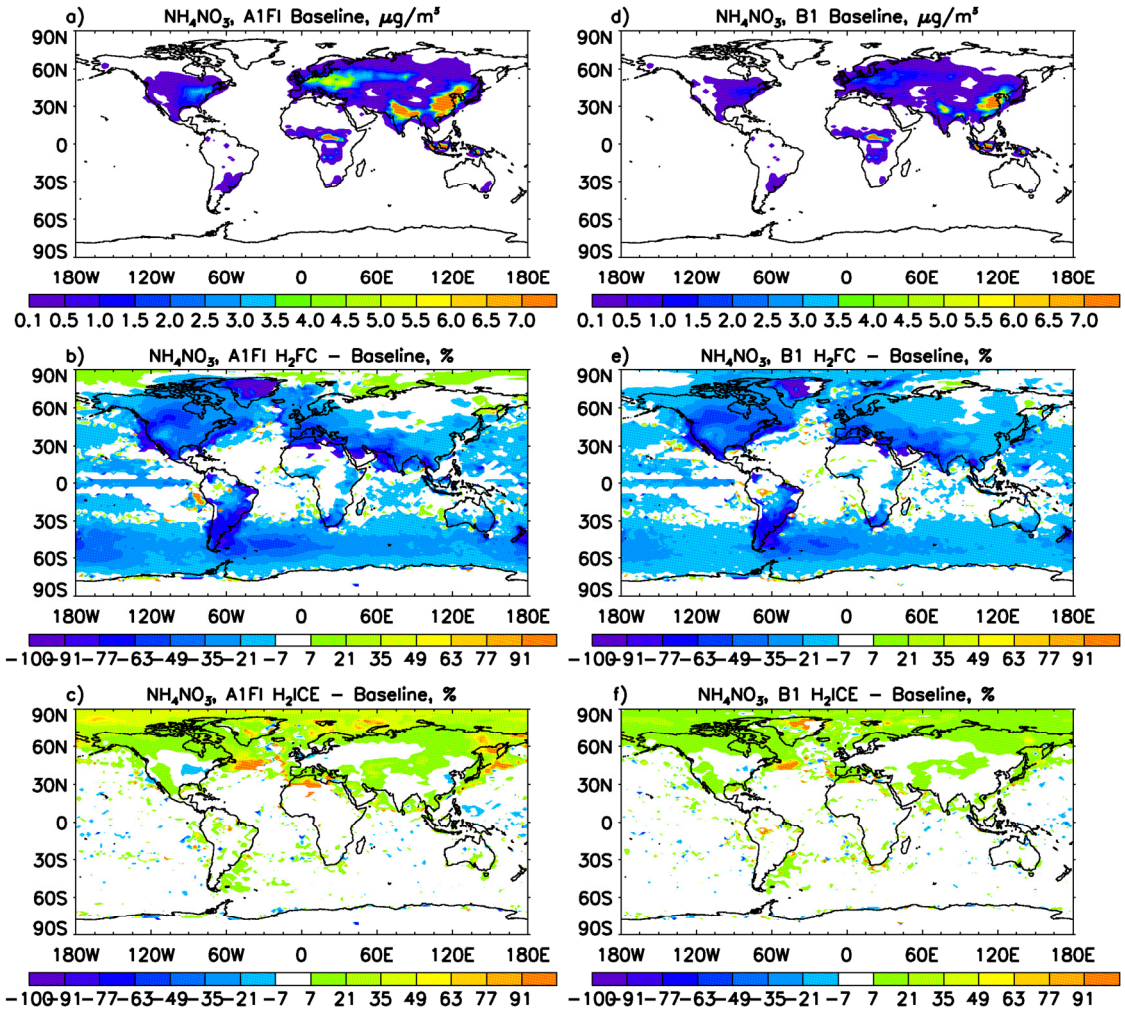


Figure 3.15 CAM-Chem simulated 2050 annual mean surface $NH_4NO_3$ concentrations in the A1FI (a) and B1 (d) Baseline scenarios and percent differences for the $H_2$ Fuel Cell ($H_2$-FC) and $H_2$ Internal Combustion Engine ($H_2$-ICE) scenarios (b, c, e and f). Note the different scales.

Table 3.1 Tropospheric burdens for the 2000 atmosphere, the 2050 A1FI baseline scenario and percent changes for the baseline + $H_2$ (BL+$H_2$), Hydrogen fuel cell ($H_2$-FC), and Hydrogen internal combustion engine ($H_2$-ICE) scenarios from the 2050 A1FI baseline scenario simulated by the CAM-Chem model.

| | 2000 | 2050 Baseline | BL+$H_2$ | $H_2$-FC | $H_2$-ICE |
|---|---|---|---|---|---|
| $H_2$ | 626 ppbv | 839 ppbv | 41% | 40% | 38% |
| $O_3$ | 37 ppbv | 44 ppbv | 0% | -7% | -1% |
| OH | $9.7 \times 10^5$ molecules/cm$^3$ | $9.1 \times 10^5$ molecules/cm$^3$ | -2% | -4% | 7% |
| CO | 97 ppbv | 133 ppbv | 1% | -14% | -18% |
| $NO_x$ | 60 pptv | 100 pptv | 0% | -16% | 10% |
| soot | 0.025 μgC/m$^3$ | 0.025 μgC/m$^3$ | 0% | -17% | -17% |
| $SO_4$ | 0.30 μg$SO_4$/m$^3$ | 0.34 μg$SO_4$/m$^3$ | 0% | -4% | -3% |
| $NH_4NO_3$ | 0.010 μg/m$^3$ | 0.014 μg/m$^3$ | 0% | -12% | 3% |

Table 3.2 Tropospheric burdens for the 2050 B1 Baseline scenario and percent changes for the Baseline + $H_2$ (BL+$H_2$), Hydrogen Fuel Cell ($H_2$-FC), and Hydrogen internal combustion engine ($H_2$-ICE) scenarios from the CAM-Chem model simulations.

| | Baseline | BL+$H_2$ | $H_2$-FC | $H_2$-ICE |
|---|---|---|---|---|
| $H_2$ | 621 ppbv | 20% | 20% | 19% |
| $O_3$ | 37 ppbv | 0% | -5% | -1% |
| OH | $10.1\times10^5$ molecules/$cm^3$ | -1% | -4% | 3% |
| CO | 90 ppbv | 0% | -4% | -7% |
| $NO_x$ | 60 pptv | 0% | -11% | 3% |
| soot | 0.014 μgC/$m^3$ | 0% | -7% | -7% |
| $SO_4$ | 0.33 μg$SO_4$/$m^3$ | 0% | -4% | -3% |
| $NH_4NO_3$ | 0.010 μg/$m^3$ | 0% | -9% | 2% |

# CHAPTER 4: IMPACT OF A FUTURE HYDROGEN ECONOMY ON STRATOSPHERIC OZONE

The MOZART model simulation results are described and discussed in this chapter. In the following analysis, the stratosphere is defined as the model levels above the tropopause and adopts the World Meteorological Organization (WMO) definition of tropopause, i.e., the lowest level at which the lapse rate decreases to 2 K/km or less. The modeling results show that the combined effect of increased $H_2$ emissions and other emission changes in a $H_2$-based road transport sector would tend to decrease ozone concentrations in the stratosphere in all scenarios except for the B1 $H_2$-ICE scenario. The overall effects on annually, globally averaged stratospheric column ozone are -0.54%, -0.23%, -0.20% and +0.04% for A1FI $H_2$-FC, A1FI $H_2$-ICE, B1 $H_2$-FC and B1 $H_2$-ICE scenarios, respectively. First the Baseline scenarios with a fossil fuel based road transportation sector will be analyzed and then the scenarios with $H_2$ technologies will be discussed and compared with the baseline scenario.

## 4.1. Baseline scenarios

In the 2050 Baseline simulations stratospheric ozone has recovered to a significant extent compared with today's atmosphere, as would be expected from future decline of atmospheric halogen concentrations. On an annual mean global average basis, stratospheric column ozone increases by ~13 DU (1 Dobson Unit (DU) corresponds to $2.69\times10^{20}$ ozone molecules per square meter) in the 2050 A1FI BL scenario and by ~11 DU in the 2050 B1 BL scenario, from the mid-1990s atmosphere. Figure 4.1 shows stratospheric column ozone and its increase from the current atmosphere as a function of latitude and time of year in the two baseline scenarios. The increase is not uniform in space and time. The increase is least in the tropics, where stratospheric ozone increases by ~5 DU. Outside the tropics, the increase is generally greater than in the

tropics, but bears inter-hemispheric asymmetry; the increase in the Southern Hemisphere is generally greater than in the Northern Hemisphere. The increase in the hemispheric spring is largest throughout a year. Arctic stratospheric column ozone increases by ~20 and ~15 DU in the 2050 A1FI and B1 baseline scenarios. In October and November Antarctic stratospheric column ozone increases by more than 70 DU from the current value (~150 DU) to ~220 DU, signaling a partial but still significant Antarctic ozone hole recovery. These results are within the range reported in WMO (2011). The recovery of the Antarctica ozone hole in October compares well with the average of model simulations in WMO (2011).

### 4.2. $H_2$ fuel cell scenarios

The annual mean global average stratospheric column ozone in the A1FI $H_2$-FC scenario decreases by 0.54% (~1.5 DU) from the A1FI baseline. In the tropics, zonal mean stratospheric column ozone decreases by less than 1 DU from December to May; whereas it decreases by 1~1.5 DU from June to November (Figure 4.2a). Outside the tropics the reductions are even larger (greater than 1.5 DU). There is a large decrease (more than 2 DU) occurring north of 35°N from September to February, with the maximum reduction of 2.5 DU (0.8%) appearing at ~40°N in October. There is also a more than 2 DU reduction in the southern mid-latitudes from mid-June to March.

In the B1 $H_2$-FC scenario the annual, global mean stratospheric column ozone decreases by 0.20% (~0.5 DU) from the B1 baseline scenario. The pattern of decrease is similar to that in the A1FI scenario, but the magnitude is smaller (Figure 4.2b). The decrease in the tropics does not exceed 0.6 DU (or 0.2%) throughout a year, while the decrease is even smaller (< 0.4 DU or 0.15%) from December to June. Again, there are larger reductions outside the tropics (greater than 0.6 DU or 0.2%). In the Northern Hemisphere, there is a significant decrease (more than 0.8

DU) present north of 35°N from September to February. In the SH, there is a band of significant decrease (more than 0.6 DU or 0.2%) between 30°S and 60°S.

In both the A1FI and B1 $H_2$-FC scenarios, ozone concentrations are reduced throughout most of the stratosphere; however, there is a layer of slight increase of less than 1%, or $1\times10^{10}$ molecules $cm^{-3}$ in the middle stratosphere (Figure 4.3). This layer of increased ozone is about 10 km thick and starts from ~20 km altitude in the poles and from ~29 km altitude in the tropics. Above this layer in the upper stratosphere, ozone concentrations are reduced by less than $1\times10^{10}$ molecules $cm^{-3}$, or 1%. Below the increased ozone layer the ozone concentration reductions are greater as the altitude decreases.

The most significant reductions in annual, zonal mean ozone concentrations are in the upper troposphere/lower stratosphere (UT/LS) region. At each altitude level, ozone concentrations decreased more near the poles (up to $10\times10^{10}$ molecules $cm^{-3}$ in A1FI and up to $5\times10^{10}$ molecules $cm^{-3}$ in B1) than in the tropics (around $4\times10^{10}$ molecules $cm^{-3}$ in A1FI and around $2\times10^{10}$ molecules $cm^{-3}$ in B1). The relative reduction, however, is greater in the tropics as there is less ozone in the baseline scenario. The maximum zonal mean $O_3$ relative reduction (up to 10% in A1FI and up to 5% in B1) is at approximately 13 km altitude around 15ºN. In the lowermost stratosphere, ozone reductions occur partly because of the influence of the underlying troposphere, where ozone concentrations are reduced due to the reduced tropospheric ozone precursor emissions associated with the adoption of $H_2$ fuel cells (Chapter 3), and partly because local ozone production is reduced as a result of a strong reduction in $NO_x$ concentrations. As shown in Figure 4.4, $NO_x$ mixing ratios in the tropical UT/LS region decrease by up to 12% (75 pptv) in the A1FI and by up to 8% (30 pptv) in the B1 $H_2$-FC scenarios relative to their corresponding baseline scenarios. The reduction in the tropical ozone production reduces the

amount of ozone transported to the mid-latitudes and the poles. The impact of the tropospheric air and the tropospheric ozone formation mechanism on UT/LS ozone concentrations diminishes with increasing altitude. At higher altitudes, perturbations to the catalytic ozone destruction cycles contribute more to the changes in ozone concentrations.

In the mid-latitude lower stratosphere, it is well established that catalytic cycles involving $HO_x$ dominate local ozone destruction (e.g. Wennberg et al., 1994; WMO, 1995). In these model simulations $HO_x$ catalytic cycles contribute the most to the ozone loss rate in the stratosphere below 20km altitude at 35ºN at the September equinox. $HO_x$ concentrations are predicted to increase by around 3% (~$1\times10^5$ molecules $cm^{-3}$) and 1% (~$0.5\times10^5$ molecules $cm^{-3}$) for the A1FI and B1 scenarios, respectively (Figure 4.5). As a direct result, the ozone loss cycles catalyzed by $HO_x$ are enhanced.

At the same time, $NO_x$ concentrations are reduced throughout the stratosphere in the $H_2$-FC scenarios (Figure 4.4). The increased stratospheric $HO_x$ concentrations contribute to the reductions in stratospheric $NO_x$ through the reaction

$$OH + NO_2 + M \rightarrow HNO_3 + M. \qquad (4.1)$$

Additionally, stratospheric $NO_x$ is also likely to be affected by the drastic changes in tropospheric $NO_x$ concentration in the $H_2$-FC scenarios. The major source of $NO_x$ in the stratosphere is the reaction of $N_2O$ with $O(^1D)$. However, $N_2O$ and $O(^1D)$ concentrations are not significantly affected by the perturbation of a $H_2$-FC sector. It has been proposed that reactive nitrogen ($NO_y$) in the upper troposphere over tropical regions can significantly impact lower stratosphere $NO_y$ concentrations (Ko et al., 1986) due to $NO_y$'s longer lifetime than $NO_x$ and strong upwelling in this region. This hypothesis is supported by observations (e.g., Murphy et al.,

1993). In this study, $NO_y$ concentrations in the UT/LS region in 2050 are calculated to be about 1 ppbv in all scenarios, exceeding the threshold mixing ratio of 0.6 ppbv suggested by Murphy et al. (1993). Therefore, increased $NO_y$ concentrations in the UT/LS region are likely to impact the stratospheric $NO_y$ abundance. In the $H_2$-FC scenarios, model results show that $NO_y$ concentrations in the UT/LS region are significantly reduced (by ~15% for A1FI and by ~8% for B1), likely leading to decreased $NO_x$ and $NO_y$ in the stratosphere.

Furthermore, the $NO_x$ reduction impacts the $HO_x$ cycles through reactions (1) and

$$HO_2 + NO \rightarrow OH + NO_2, \qquad (4.2)$$

hence affecting $HO_x$ as well as the partitioning between $HO_2$ and OH. In this case, $HO_2$ concentrations increase due to decreased availability of NO in reaction (4.2), leading to enhanced ozone loss since the rate of $HO_x$ cycles is dependent on $HO_2$ concentrations to the first order. Meanwhile, the rate of reaction (4.1) would fall as NO concentrations decrease, making reaction (4.1) a smaller $HO_x$ sink.

Both of these effects tend to further enhance the $HO_x$ cycles. As shown in Figure 4.6, the daily average ozone destruction rate by the $HO_x$ cycles at 35°N at the September equinox is increased by 2% (A1FI) and 1% (B1) at 20 km altitude (Figure 4.6); the total ozone destruction rate by all catalytic cycles increased by 0.5% (A1FI) and 0.2% (B1) due to enhanced $HO_x$ cycles.

In addition to promoting the $HO_x$ cycles, a decrease in $NO_x$ concentrations also leads to an enhancement of the halogen cycles via $NO_x$/halogen cycles coupling. Nevertheless, this enhancement would have a smaller impact on ozone concentrations since in 2050 halogen cycles are only responsible for a few percent of ozone destruction rate in the lower stratosphere, in which stratospheric halogen loading is expected to be significantly smaller than today's. As

shown in Figure 4.6, the overall ozone destruction rate is enhanced by 0.1% in the A1FI and 0.04% in the B1 scenarios due to the halogen cycles at 35°N at the September equinox at 20 km level. In sum, the decrease in ozone concentrations in the lower stratosphere in the A1FI and B1 $H_2$-FC scenarios is primarily due to an intensification of the $HO_x$ catalyzed $O_3$ destruction cycles.

In the middle stratosphere (25-35km altitude in the tropics, somewhat lower at higher latitudes) annually, zonally averaged ozone concentrations increase by up to 0.4% in both the A1FI and B1 $H_2$-FC scenarios (Figure 4.3). Even though ozone loss rate due to $HO_x$ catalytic cycles increases due to the previously discussed mechanisms in this region, the overall ozone loss rate is slowed down because $NO_x$ cycles dominate ozone loss in the middle stratosphere and $NO_x$ concentrations are reduced in this region. As shown in Figure 4.4, annually, zonally averaged $NO_x$ concentrations decrease by ~3% (~50 pptv) in the A1FI and by ~2% (~20 pptv) in the B1 scenario. The $NO_x$ concentration decrease is due to enhancement of reaction (4.1), through which increased $HO_x$ concentrations make this reaction a larger $NO_x$ sink and, likely due to decreases in $NO_x$ concentrations in the underlying atmosphere. The ozone loss rate due to $NO_x$ catalyzed cycles is reduced throughout most of the stratosphere (Figure 4.6); however, its impact on ozone concentrations is only significant in the middle stratosphere where $NO_x$ cycles dominate ozone destruction. As shown in Figure 4.6, the overall ozone destruction rate at 25 km altitude at 35°N at the September equinox is decreased by 0.35% in the A1FI and by 0.13% in the B1 scenario due to the attenuation of the $NO_x$ catalyzed ozone destruction cycles. Therefore, a slight ozone concentration increase is calculated in the middle stratosphere in both the $H_2$-FC scenarios. The increase in ozone concentration in the middle stratosphere, however, cannot fully compensate the decrease in the lower stratosphere since ozone molecules per unit volume is lower at higher altitude.

In the upper stratosphere, $HO_x$ catalyzed cycles again dominate ozone loss cycles. The $HO_x$ concentrations increase by 2-3% in the A1FI and by ~1% in the B1 scenarios (Figure 4.5). This increase is due to enhanced $H_2$ abundance and the decline in the rate of reaction (4.1) as a result of the $NO_x$ concentrations decrease. As a direct result, $HO_x$ catalyzed cycles are enhanced. As shown in Figure 4.6, the ozone destruction rate due to $HO_x$ cycles at 25 km altitude at 35°N at the September equinox level is increased by 0.3% in the A1FI and 0.13% in the B1 scenarios. The resulting $O_3$ concentration decline in this region is less than 1% in the A1FI and B1 $H_2$-FC scenarios (Figure 4.3). Its impact on stratospheric column ozone is small owing to the low molecule concentrations at such high altitudes.

### 4.3. $H_2$ internal combustion engine scenarios

The overall impact of a $H_2$-ICE road transportation sector on stratospheric ozone concentration is smaller compared with the corresponding $H_2$-FC scenarios mainly because of $NO_x$ being higher for the ICE scenarios. The annually, globally averaged stratospheric column ozone in the A1FI $H_2$-ICE scenario would be reduced by 0.23%, or 0.5DU. Stratospheric column ozone decreases north of 50°S but increases south of this latitude (Figure 4.7a). In the tropics, stratospheric column ozone decreases by 0.1-0.3%, or 0-1 DU throughout a year. In the northern mid- and high-latitudes, stratospheric column ozone decreases by more than 1 DU. The greatest decrease (1.5 DU or 0.6%) occurs at the northern mid-latitudes from September to January. In the Antarctic region, stratospheric column ozone increases by up to 3 DU, or 1% from October to December.

From the zonal average perspective, annual mean ozone concentrations are reduced in the lower stratosphere in the A1FI $H_2$-ICE scenario (Figure 4.8a). In the tropics, the reduction extends to the middle stratosphere (30 km altitude). The maximum relative reduction (5%)

occurs at 17 km altitude just north of the equator, whereas the largest concentration change (a decrease of $8\times10^{10}$ molecules $cm^{-3}$) is at 12 km in the Arctic region. There are very slight ozone reductions above 45 km altitude in the tropics and above 48 km altitude in the poles. Ozone concentrations are increased in the rest of the stratosphere, but the relative increase does not exceed 1%. There is an increase of up to $8\times10^{10}$ molecules $cm^{-3}$ around 18 km in the Antarctic region.

As in the $H_2$-FC scenarios, ozone concentration changes in the $H_2$-ICE scenarios are a result of changes in radical concentrations, which affect the catalytic cycles destructing stratospheric ozone. $HO_x$ concentrations decrease in the upper troposphere due to the reduced NMVOCs emissions in the A1FI $H_2$-ICE scenario, as NMVOCs oxidation provides a $HO_x$ source in the upper troposphere. Increase in $NO_x$ concentrations (Figure 4.10a) also contributes to the $HO_x$ decrease through reaction (4.1). This decrease penetrates into the lower stratosphere with rising air from the tropics. Figure 4.9a shows the pattern of $HO_x$ reductions, which diminish with altitude. Above 20 km in the tropics and above 15 km near the poles, $HO_x$ concentrations increases slightly as the $H_2$ leaked into the atmosphere provides a $HO_x$ source in the stratosphere.

$NO_x$ concentrations decrease in the middle stratosphere but increase in the upper and lower stratosphere in the A1FI $H_2$-ICE scenario (Figure 4.10a). In the lower stratosphere $NO_x$ concentrations increase because of the $NO_x$ budget increase throughout the troposphere since in the $H_2$-ICE scenarios $NO_x$ is still emitted as combustion byproduct of internal combustion engines (Chapter 3). Meanwhile, the decrease in $HO_x$ concentrations (Figure 4.9a) decreases the $NO_x$ loss due to reaction (4.1), which in turn increases $NO_x$. In the middle stratosphere where $HO_x$ concentrations (Figure 4.9a) are increased, the $NO_x$ loss due to reaction (4.1) is reduced,

resulting in increased $NO_x$ concentrations. The maximum reduction, around 24 pptv, occurs at 35 km level near the equator.

As shown in Figure 4.11a, the ozone destruction rate due to $HO_x$ cycles at 35°N at the September equinox increases by 0.4% to 1.1% between 20 km and 50 km levels in the A1FI $H_2$-ICE scenario, a direct result of increased $HO_x$ concentrations. In the middle stratosphere between 28 km and 40 km levels, the increase in the ozone destruction rate due to $HO_x$ cycles is more than 1%. However, the contribution of $HO_x$ cycles to the total ozone destruction rate is least in the middle atmosphere (Figure 4.11b) because $NO_x$ cycles dominate ozone destruction here. In the upper and lower stratosphere where $HO_x$ cycles dominate, contributions of the $HO_x$ cycles to the total ozone loss rate increase by 0.35% at 45 km level and by 0.3% at 21 km level. This intensification is damped and even offset by the attenuation of the $NO_x$ cycles in the lower and middle stratosphere, resulting in reduction in total ozone loss rate between 23 and 30 km levels. The combined impact of the perturbations to different catalytic cycles on ozone is a small in magnitude but spatially widespread ozone concentration increase in the middle stratosphere (Figure 4.8a). However, this increase does not fully compensate the decrease in column in the lower stratosphere because ozone is denser in terms of molecular number concentration at lower levels. The global-mean column ozone in the stratosphere would still be 0.23% less than that in the A1FI BL atmosphere.

In the B1 $H_2$-ICE scenario the annual, global mean stratospheric column ozone is increased by 0.04%, or 0.1 DU. Stratospheric column ozone is reduced north of 10ºS but is increased south of this latitude throughout the year (Figure 4.7b). The decrease in stratospheric column ozone in the Northern Hemisphere is no more than 0.5 DU. There is an increase of up to 3.5 DU, or 1%, in stratospheric column ozone in the Antarctic region from October to December.

From the zonal mean perspective, annual mean ozone concentrations are reduced in the lower stratosphere in the B1 $H_2$-ICE scenario (Figure 4.8b). The reduction pattern resembles that in the A1FI H2-FC scenario, but the magnitude of reduction is much smaller. The maximum relative reduction (1.5%) occurs at 17 km altitude, whereas the concentration change is less than $2\times10^{10}$ molecules $cm^{-3}$. Ozone concentrations are increased in the rest of the stratosphere (except two cells of very slight reduction at 30 km level between 30°S and 60°S and between 30°N and 60°N). There is up to $7\times10^{10}$ molecules $cm^{-3}$, ~1%, increase in ozone concentrations at levels around 18 km in the Antarctic region.

Again, $HO_x$ concentrations decrease in the troposphere in the B1 $H_2$-ICE scenario, for the reason mentioned in discussion of the A1FI $H_2$-ICE scenario. This decrease in the B1 $H_2$-ICE scenario is smaller in magnitude compared with that in the A1FI $H_2$-ICE scenario, but penetrates higher into the middle stratosphere (Figure 4.9b), as the smaller strength of $HO_x$ source from the $H_2$ leakage emission in the B1 $H_2$-ICE scenario cannot fully offset the decrease originated in the upper troposphere.

$NO_x$ concentrations increase in the whole stratosphere except a small region in the Southern Hemisphere a few kilometers above the tropopause in the B1 $H_2$-ICE scenario (Figure 4.10b). In the lower stratosphere $NO_x$ concentrations increase as they do in the A1FI $H_2$-ICE scenario, but again the magnitude of increase is smaller. In the Southern Hemisphere, the changes of $NO_x$ concentrations are in the opposite sign to that of $HO_x$ concentrations (Figure 4.9b), indicating a link between $HO_x$ and $NO_x$ concentrations via reaction (4.1). In the Northern Hemisphere, $NO_x$ concentrations increase as a result of the widespread decrease in $HO_x$ concentrations (Figure 4.9b). The increase in $NO_x$ concentrations in the middle and upper

stratosphere can be as much as 20 ppbv, however, the perturbation to the $NO_x$ cycles is relatively small because the baseline $NO_x$ concentrations are high in this region.

In the stratosphere between 20 km and 50 km levels at 35°N at the September equinox, the perturbations to each catalytic cycles are modest (between -0.1% and +0.3%) except for the halogen cycles, which decrease by 1.5% to 2.4% (Figure 4.11c). Despite the $NO_x$ concentration increase (less than 1%) throughout the stratosphere, the impact of the enhanced $NO_x$ catalyzed cycles on ozone in the lower stratosphere is "buffered" by the decrease in the halogen catalyzed cycles (Figure 4.11d). Increased $NO_x$ concentrations lead to slower halogen catalyzed cycles via halogen/$NO_x$ coupling, behaving like a buffer (Nevison et al., 1999). In the upper stratosphere, enhanced $HO_x$ catalyzed cycles are compensated by decreased halogen catalytic cycles. The resulting ozone loss rate is slowed down throughout the stratosphere. Zonal mean ozone concentrations increase slightly throughout the middle and upper stratosphere (Figure 4.11b). In the lower stratosphere, ozone decreases in the tropics and the Northern Hemisphere due to tropospheric impact, but increases in the southern high latitudes, where halogen catalyzed ozone loss cycles dominate, and halogen cycles are slowed down in this region as $NO_x$ concentrations increase. In the B1 $H_2$-ICE scenario the overall impact on stratospheric column ozone of is minimal (+0.04%) among all the studied $H_2$ scenarios.

### 4.4. Conclusions

In this study the possible impact of a future $H_2$-based road transportation sector on stratospheric composition and chemistry is investigated through chemistry-climate model simulations of the 2050 atmosphere based on several emission scenarios designed to bracket the possible future changes in emissions. These scenarios are based on the IPCC high (A1FI) and

low (B1) emitting paths. In addition, the impacts of two $H_2$ technology options are assessed: utilizing $H_2$ in fuel cells and utilizing $H_2$ in internal combustion engines.

These MOZART simulation results suggest that future implementation of a $H_2$-based road transportation sector would perturb stratospheric chemistry, by means of affecting catalytic ozone destruction cycles involving $HO_x$, $NO_x$, and halogens. The magnitude of the impact depends on the future growth path as well as the $H_2$ technology adopted. In general the impact is larger for the A1FI based scenarios than the corresponding B1 based scenarios, and the $H_2$-FC scenarios result in more ozone loss than the $H_2$-ICE scenarios. The impact on global stratospheric column ozone is considerable for the A1FI scenarios (-0.54% for $H_2$-FC and -0.23% for $H_2$-ICE) and for the B1 $H_2$-FC scenario (-0.20%) while there is a slight increase (0.04%) for the B1 $H_2$-ICE scenario. The largest relative reduction of ozone concentration occurs in the lower stratosphere where $HO_x$ cycles dominate $O_3$ loss and impact from the underlying troposphere is prominent. In the middle stratosphere ozone concentrations increase slightly while at higher altitudes they either decrease slightly or increase slightly depending on scenarios. These changes have relatively little impact on column ozone since ozone at this level only makes up a small fraction in terms of column ozone, due to the low ozone number concentration there. It is important to note that the chosen emission scenarios are developed with a 100% market penetration assumption. Less impact on stratospheric ozone is possible in the case of an intermediate market penetration.

It is important to note that even though a $H_2$-based road transportation sector is likely to decrease stratospheric ozone, this reduction is considerably less than the ozone recovery due to the reductions in ozone depleting substances, e.g., CFCs, from the atmosphere in 2050. In terms of total column ozone, the MOZART simulations results suggest that there would still be

4%~5% more ozone in the 2050 atmosphere with a $H_2$-based road transportation sector than that in today's atmosphere. Therefore, the ozone reduction due to a $H_2$-based road transportation sector should not constitute a major concern on stratospheric ozone and increased UV radiation at the surface in 2050.

## 4.5. Figures

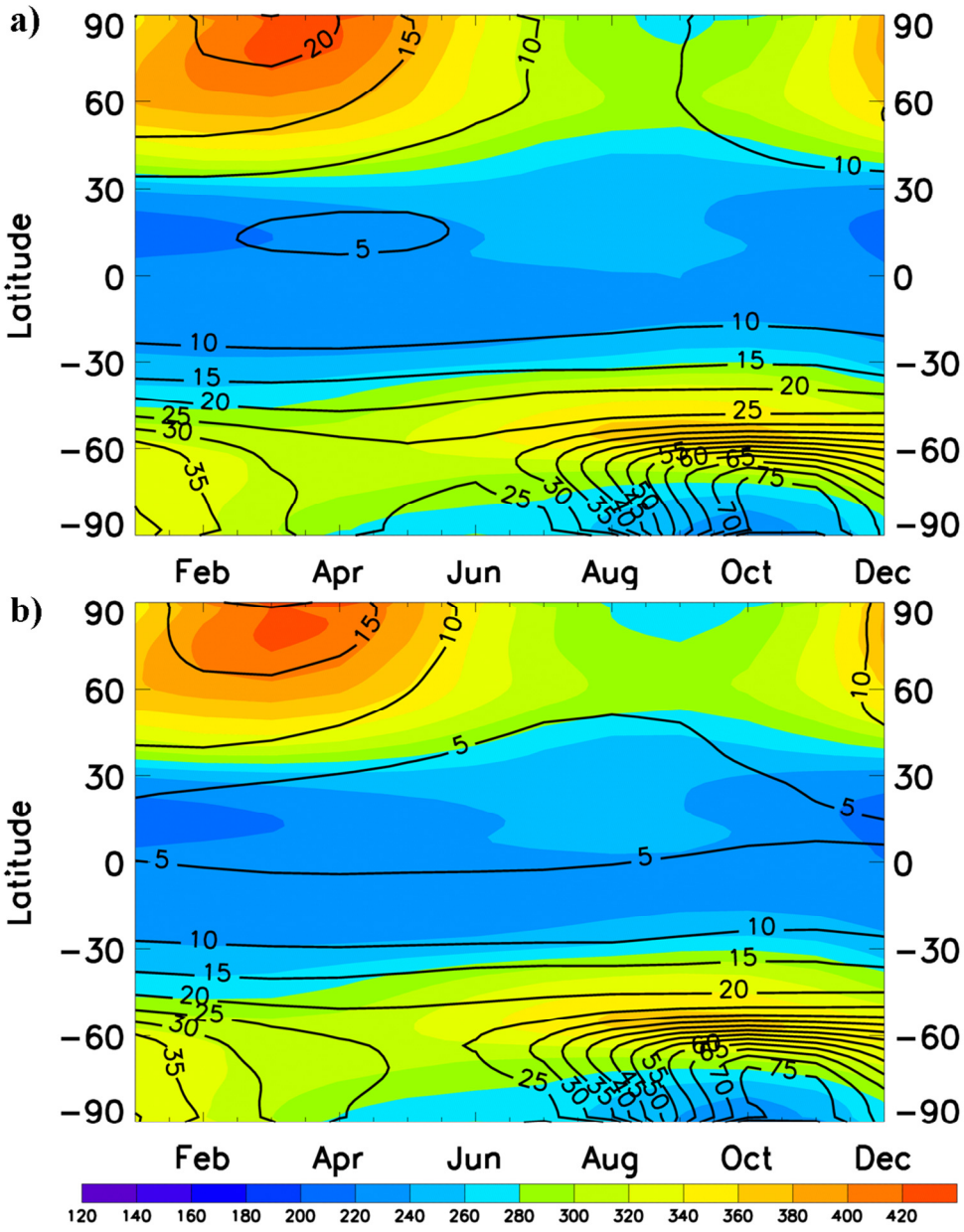


Figure 4.1 2050 zonal mean stratospheric column $O_3$ (shown by color in units of DU) and the increase from today's atmosphere (a model run representing mid-1990s atmosphere) (shown by contours in units of DU) as a function of latitude and time of a year for (a) A1FI BL and (b) B1 BL scenarios.

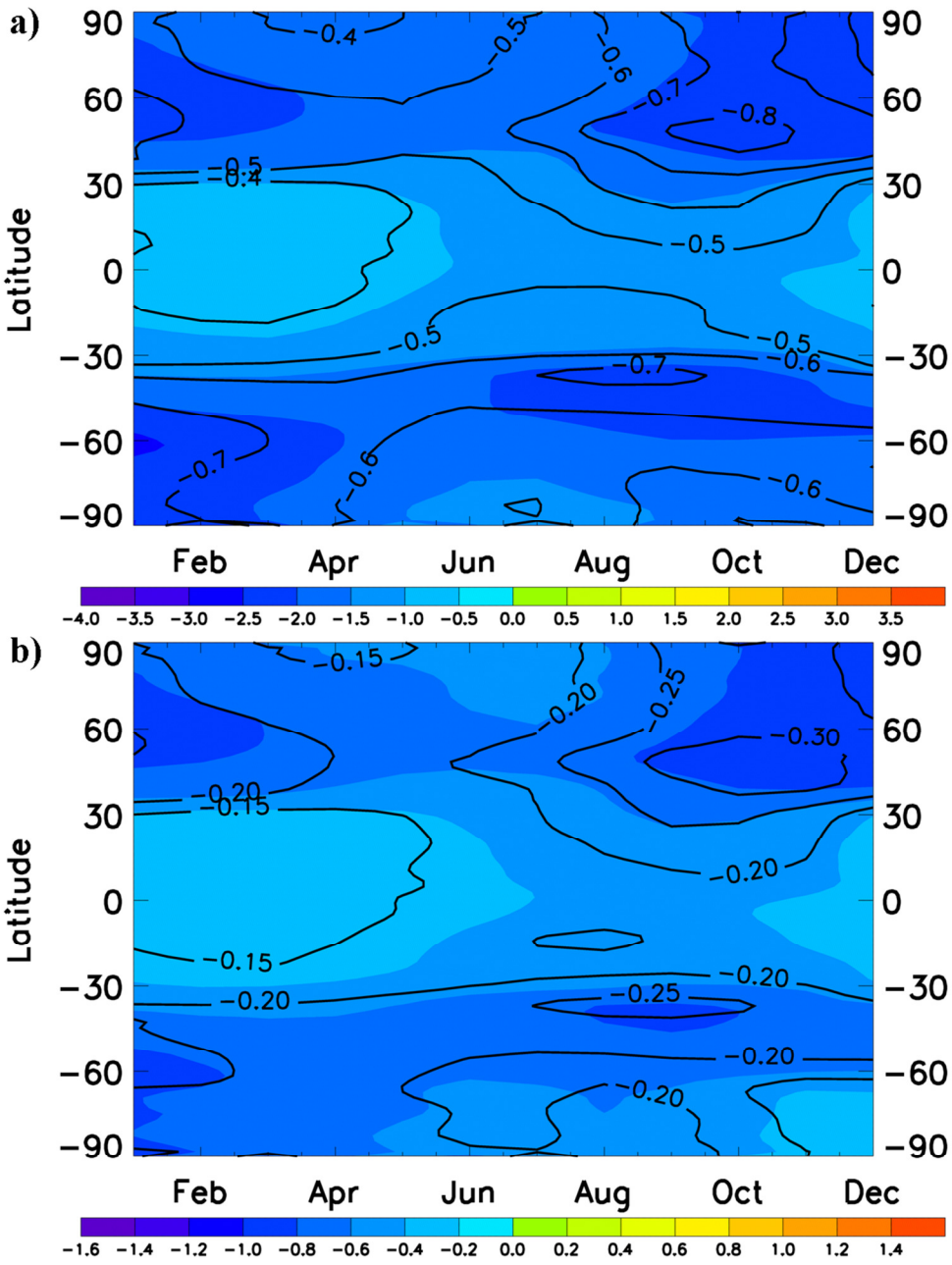


Figure 4.2 Zonal mean stratospheric column $O_3$ changes in units of DU (shown by color) and the relative change in % (shown by contours) in the $H_2$-FC scenarios compared with the BL scenarios as a function of latitude and time of a year for (a) A1FI and (b) B1 scenarios.

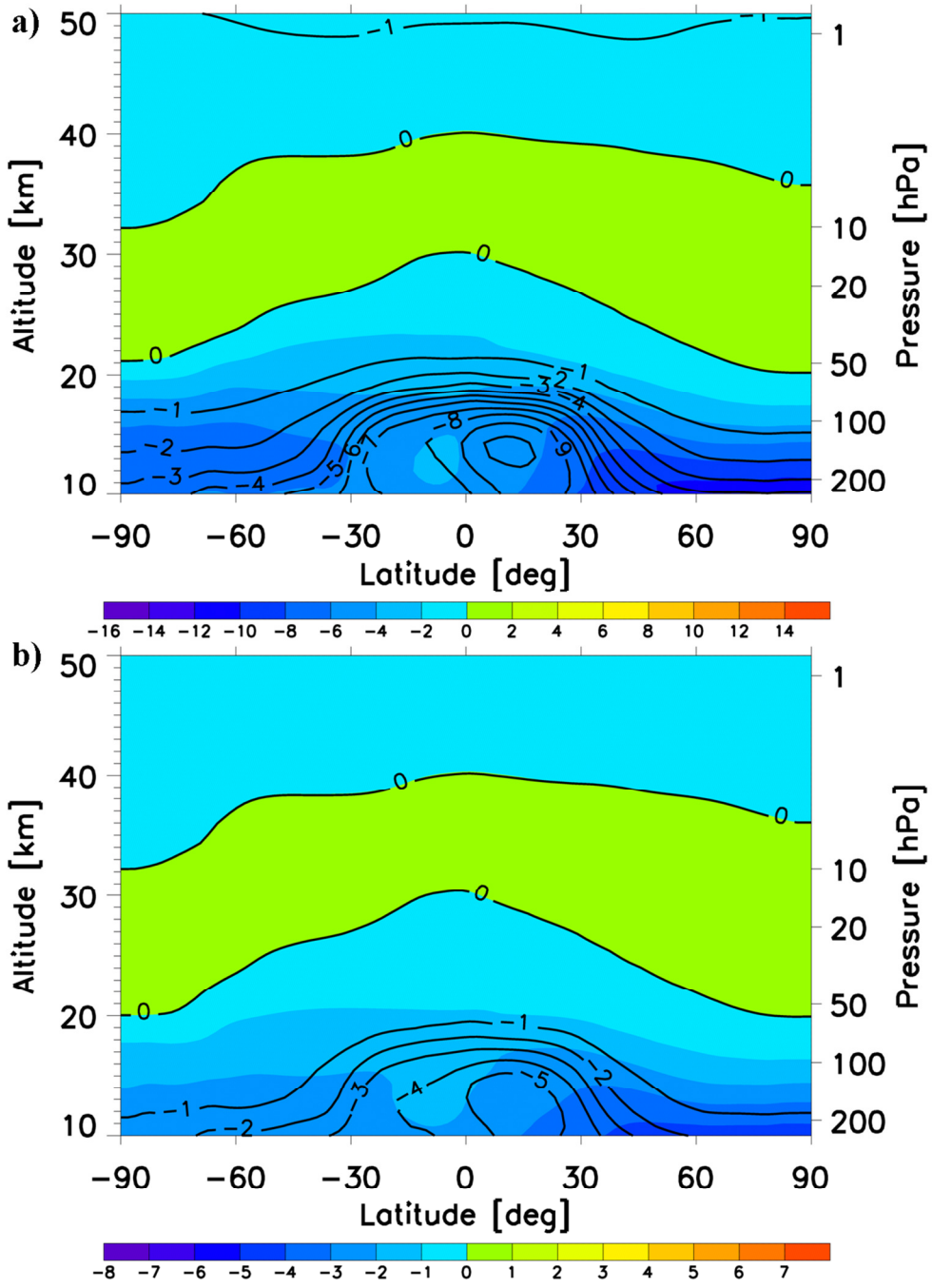


Figure 4.3 Annually, zonally averaged $O_3$ concentration changes in units of $10^{10}$ molecules $cm^{-3}$ (shown by color) and the relative change in % (shown by contours) in the $H_2$-FC scenarios compared with the BL scenarios as a function of latitude and altitude for (a) A1FI and (b) B1 scenarios.

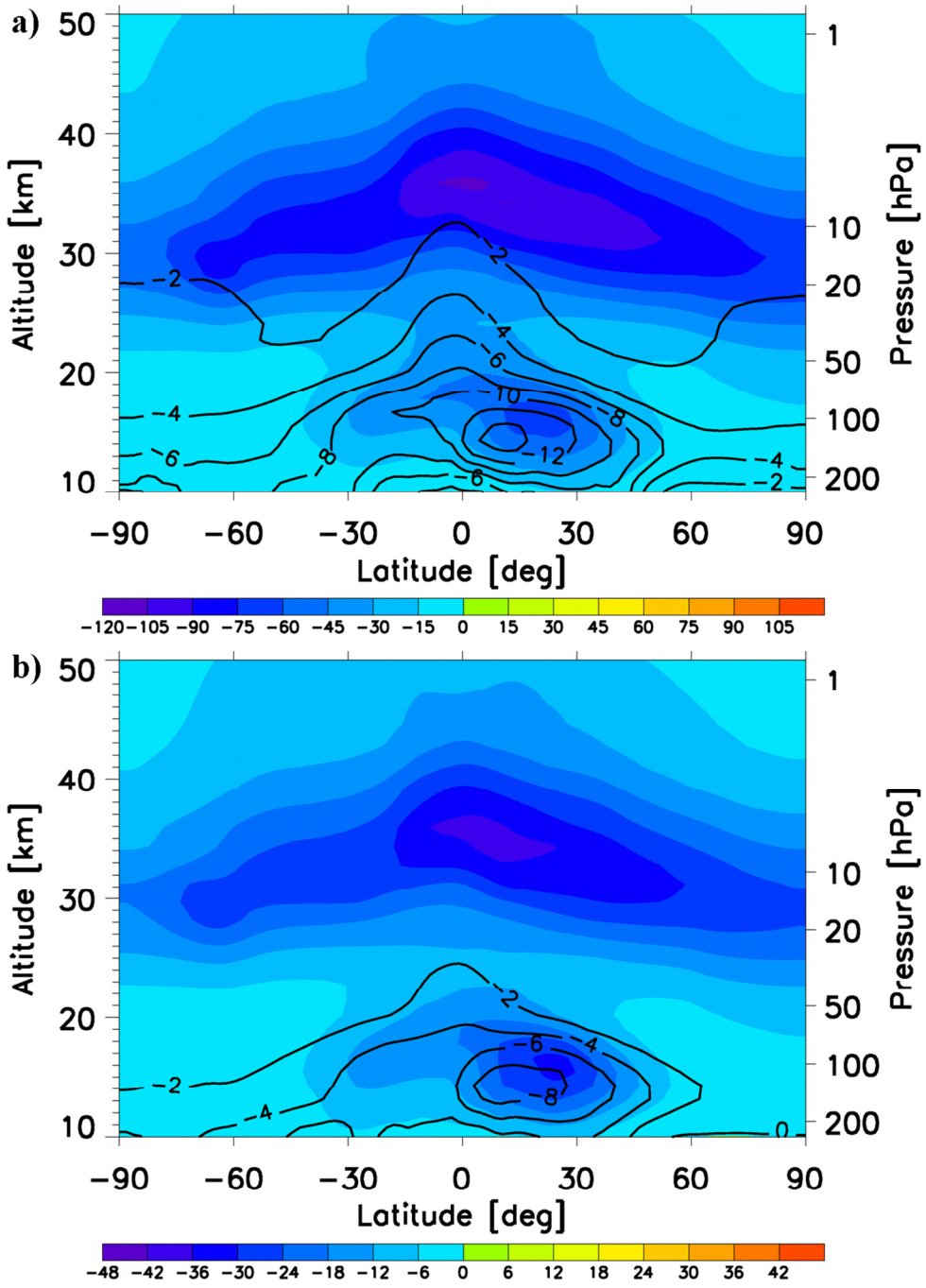


Figure 4.4 Annually, zonally averaged $NO_x$ concentration changes in units of pptv (shown by color) and the relative change in % (shown by contours) in the $H_2$-FC scenarios compared with the BL scenarios as a function of latitude and altitude for (a) A1FI and (b) B1 scenarios.

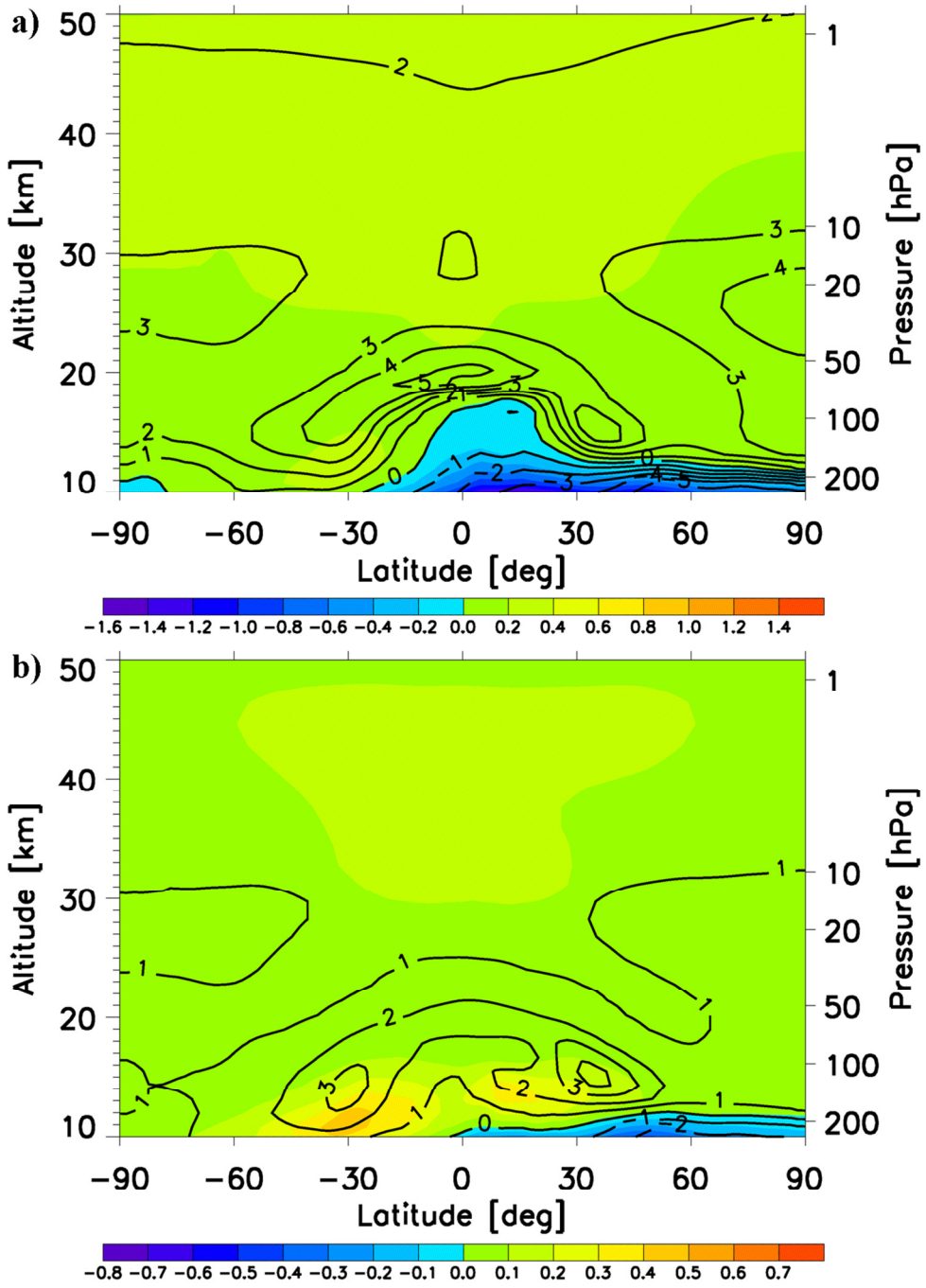


Figure 4.5 Annually, zonally averaged $HO_x$ concentration changes in units of $10^6$ molecules $cm^{-3}$ (shown by color) and the relative change in % (shown by contours) in the $H_2$-FC scenarios compared with the BL scenarios as a function of latitude and altitude for (a) A1FI and (b) B1 scenarios.

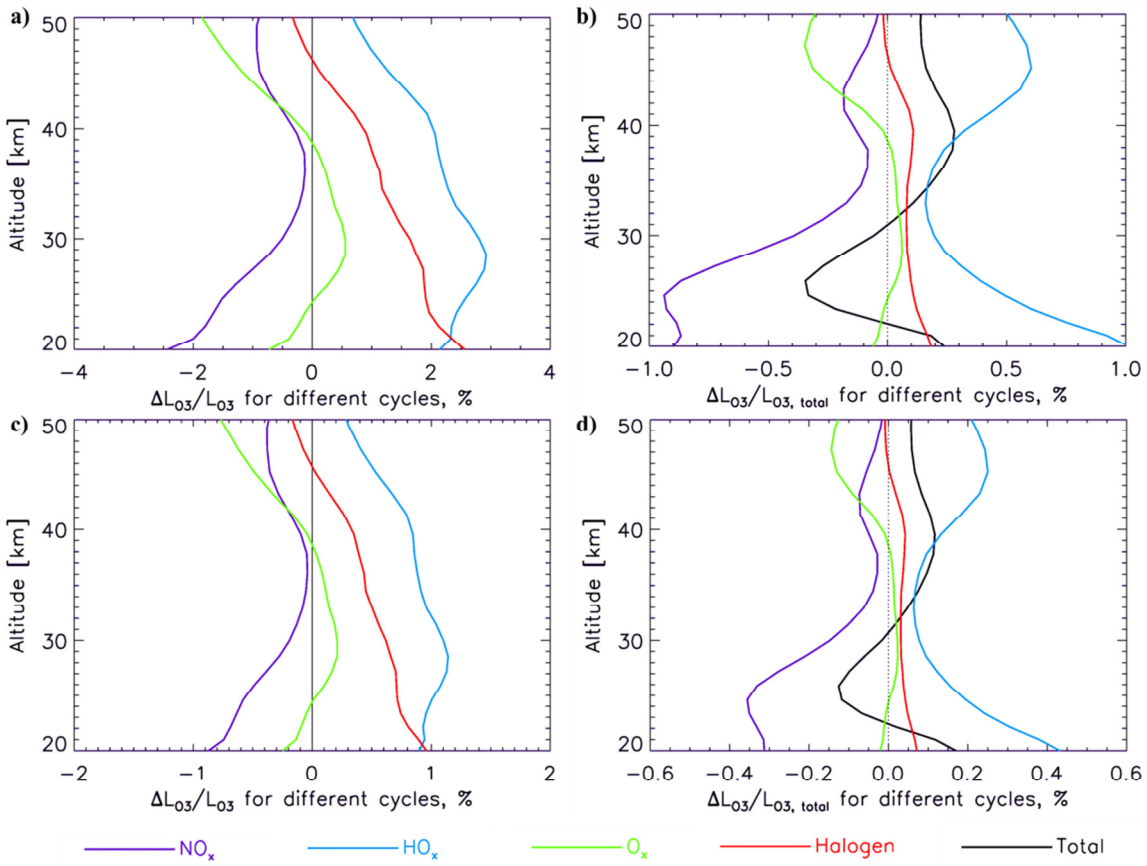


Figure 4.6 Changes in contributions of different catalytic $O_3$ destruction cycles to the total $O_3$ loss in the $H_2$-FC scenarios compared to the Baseline scenario. Panels (a) and (b) are for A1FI and panels (c) and (d) are for B1. (a) and (c): % change in contribution of each catalytic cycle compared to its contribution in the BL; (b) and (d): % change in contributions of different catalytic $O_3$ destruction cycles compared to the total $O_3$ loss rate in BL. All figures are daily averaged values for the September equinox at 35ºN.

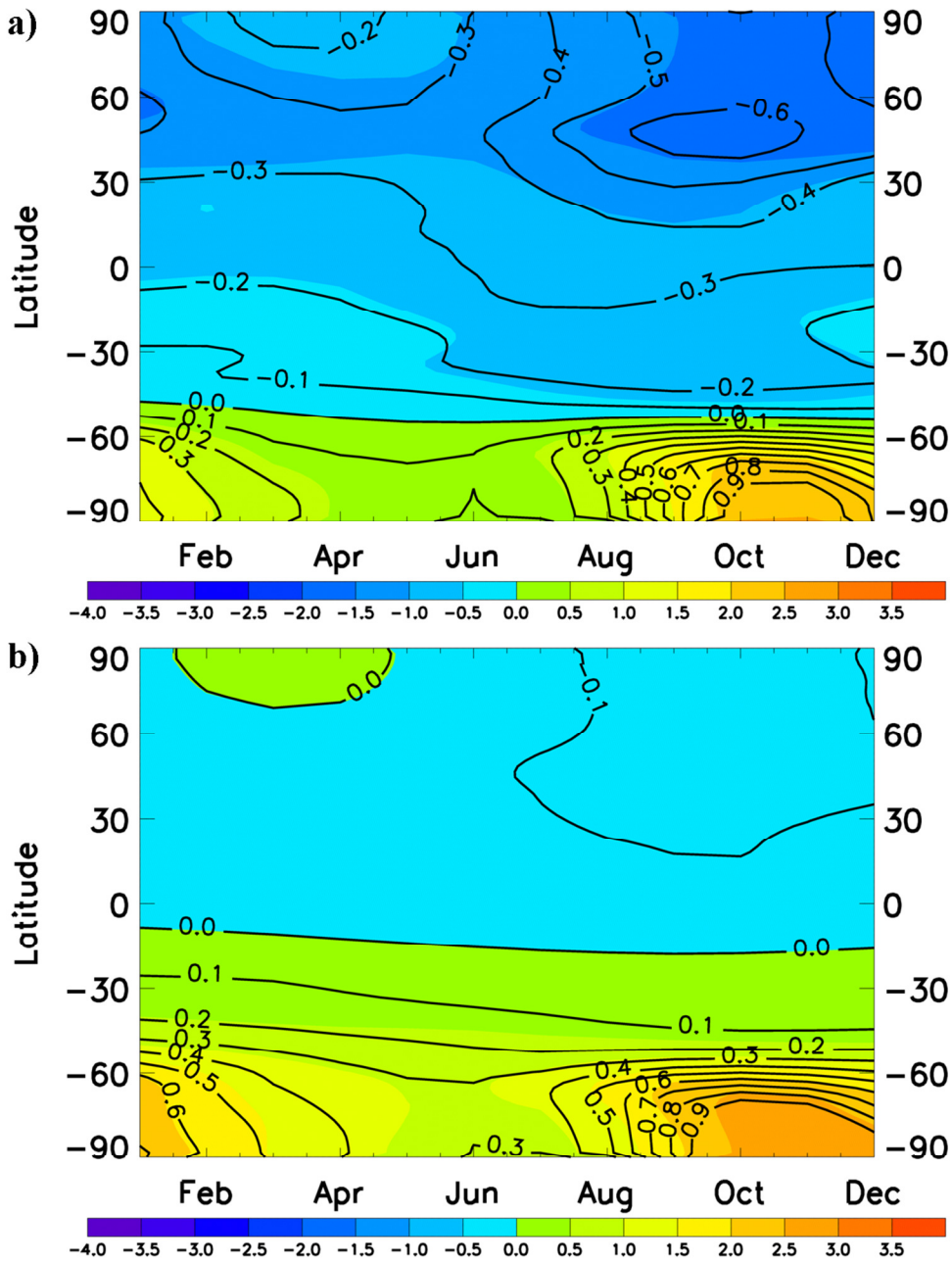


Figure 4.7 Zonal mean stratospheric column $O_3$ changes in units of DU (shown by color) and the relative change in % (shown by contours) in the $H_2$-ICE scenarios compared with the BL scenarios as a function of latitude and time of a year for (a) A1FI and (b) B1 scenarios.

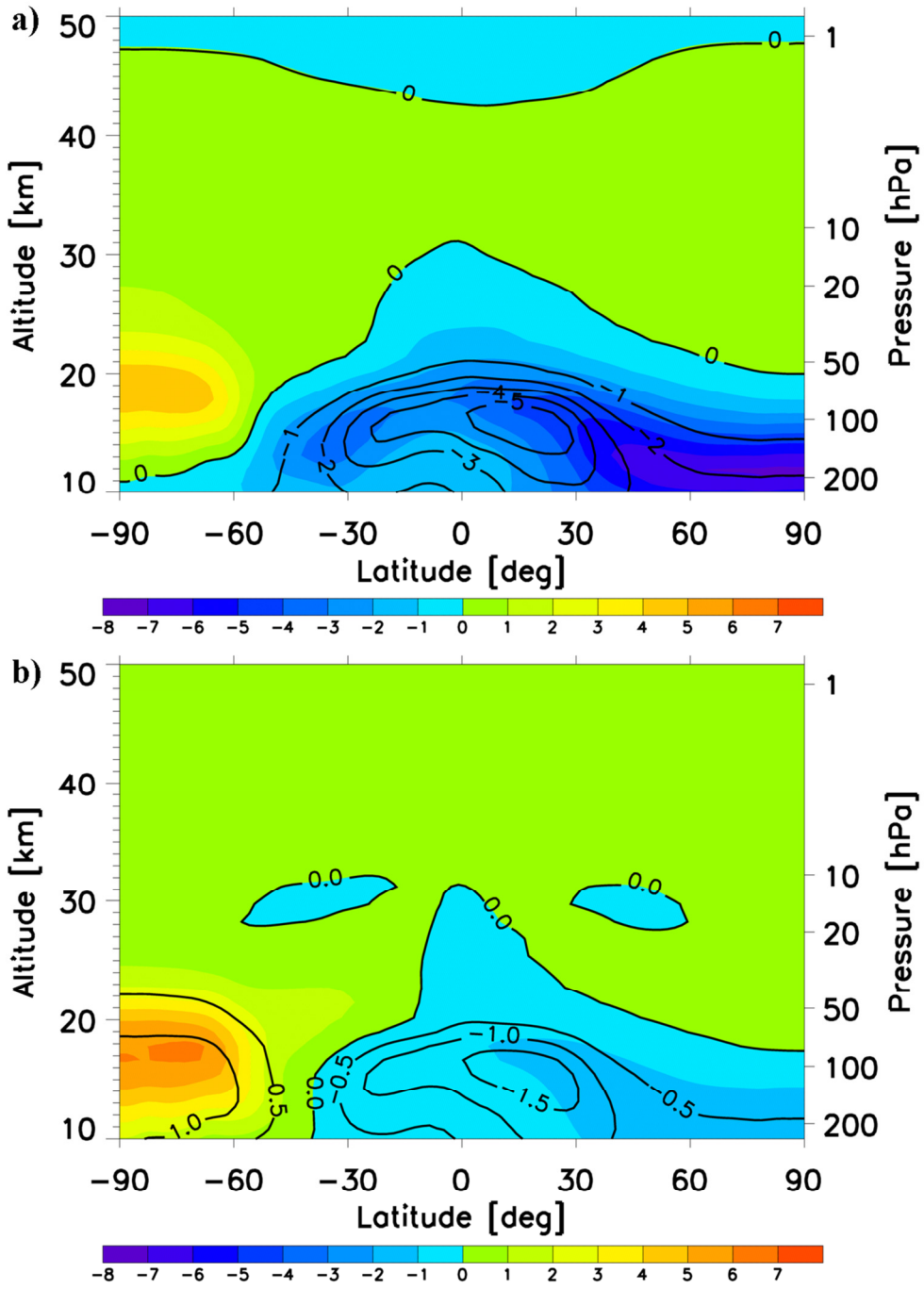


Figure 4.8 Annually, zonally averaged $O_3$ concentration changes in units of $10^{10}$ molecules $cm^{-3}$ (shown by color) and the relative change in % (shown by contours) in the $H_2$-ICE scenarios compared with the BL scenarios as a function of latitude and altitude for (a) A1FI and (b) B1 scenarios.

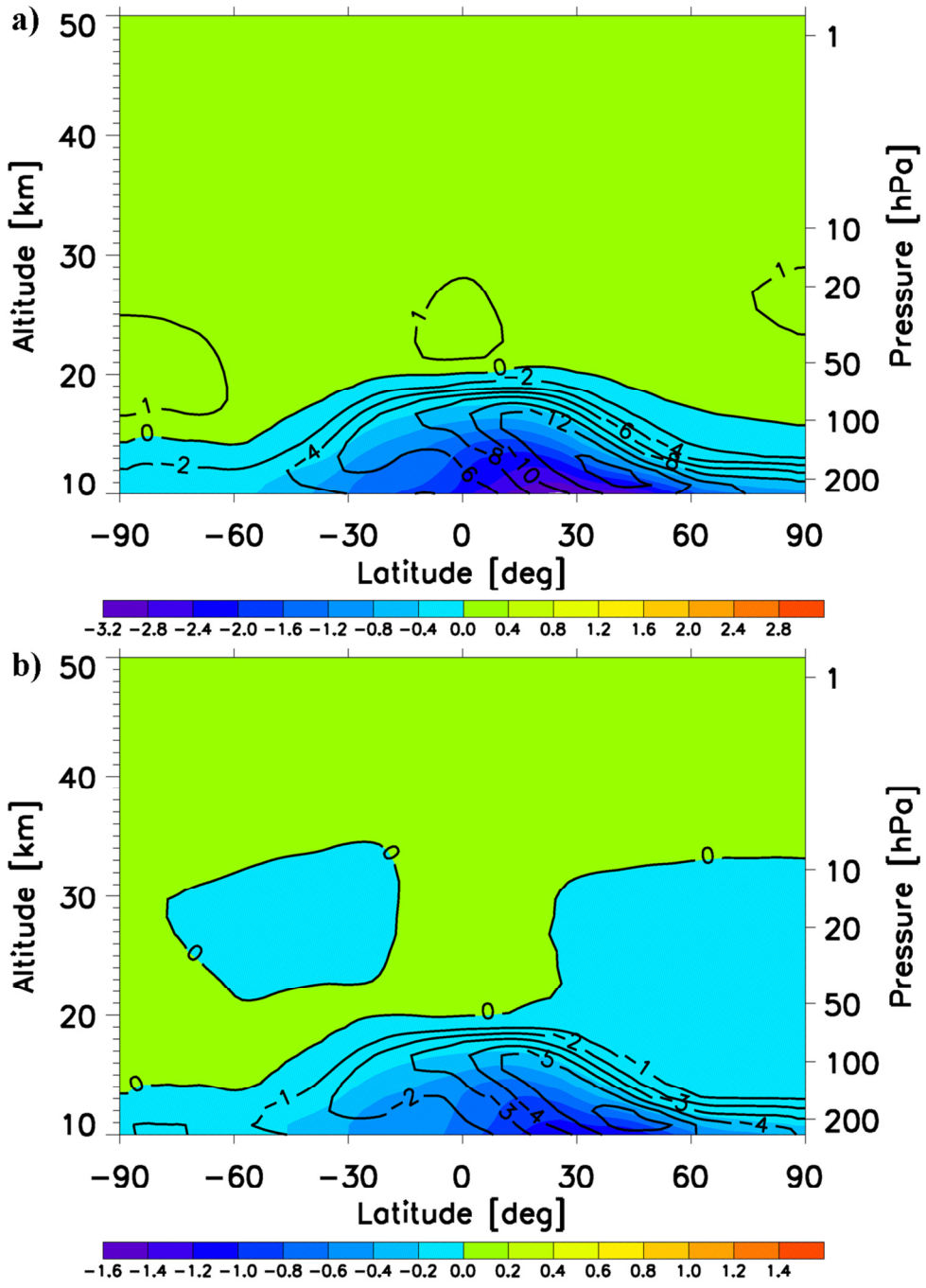


Figure 4.9 Annually, zonally averaged $HO_x$ concentration changes in units of $10^6$ molecules $cm^{-3}$ (shown by color) and the relative change in % (shown by contours) in the $H_2$-ICE scenarios compared with the BL scenarios as a function of latitude and altitude for (a) A1FI and (b) B1 scenarios.

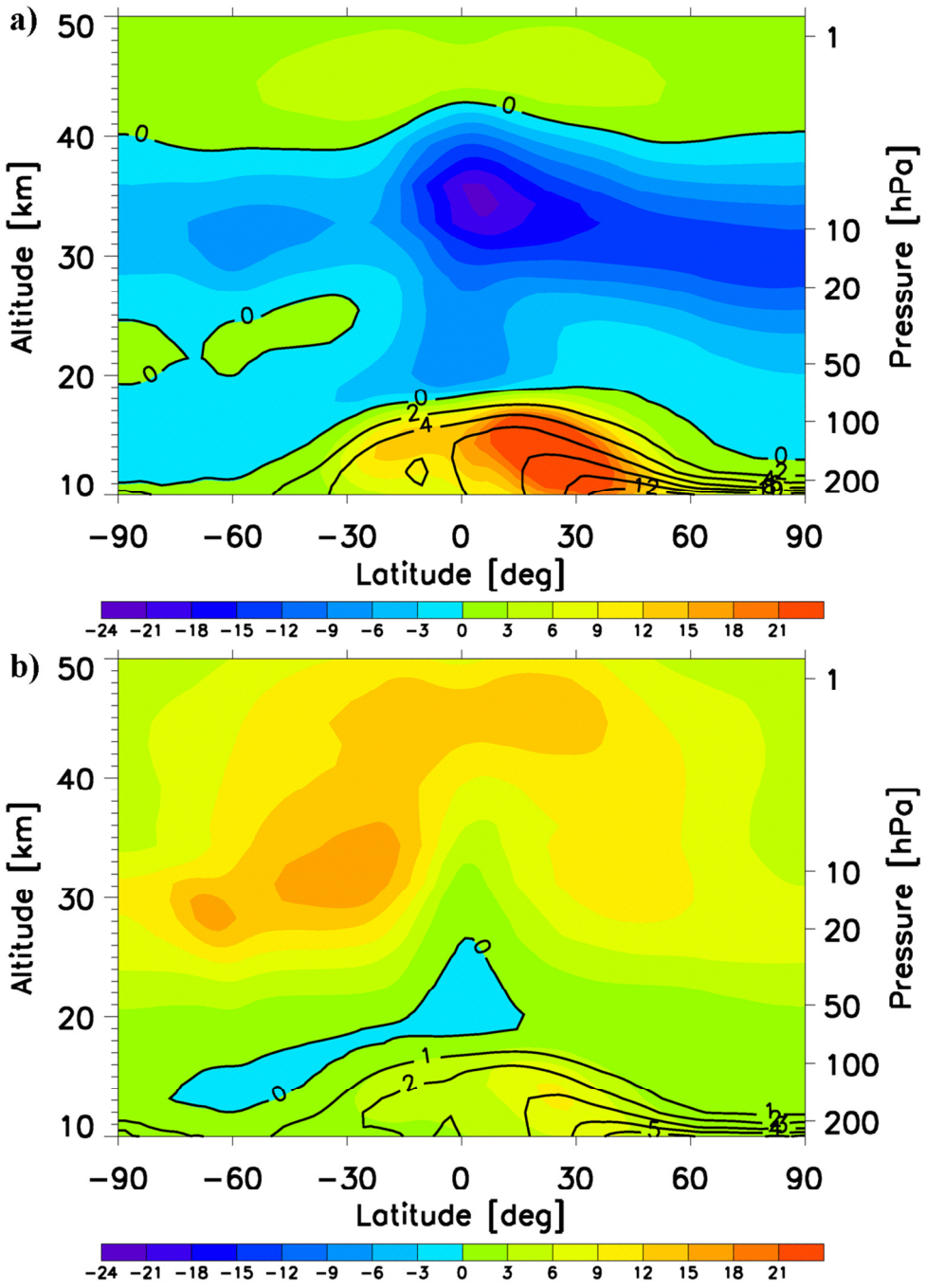


Figure 4.10 Annually, zonally averaged $NO_x$ concentration changes in units of pptv (shown by color) and the relative change in % (shown by contours) in the $H_2$-ICE scenarios compared with the BL scenarios as a function of latitude and altitude for (a) A1FI and (b) B1 scenarios.

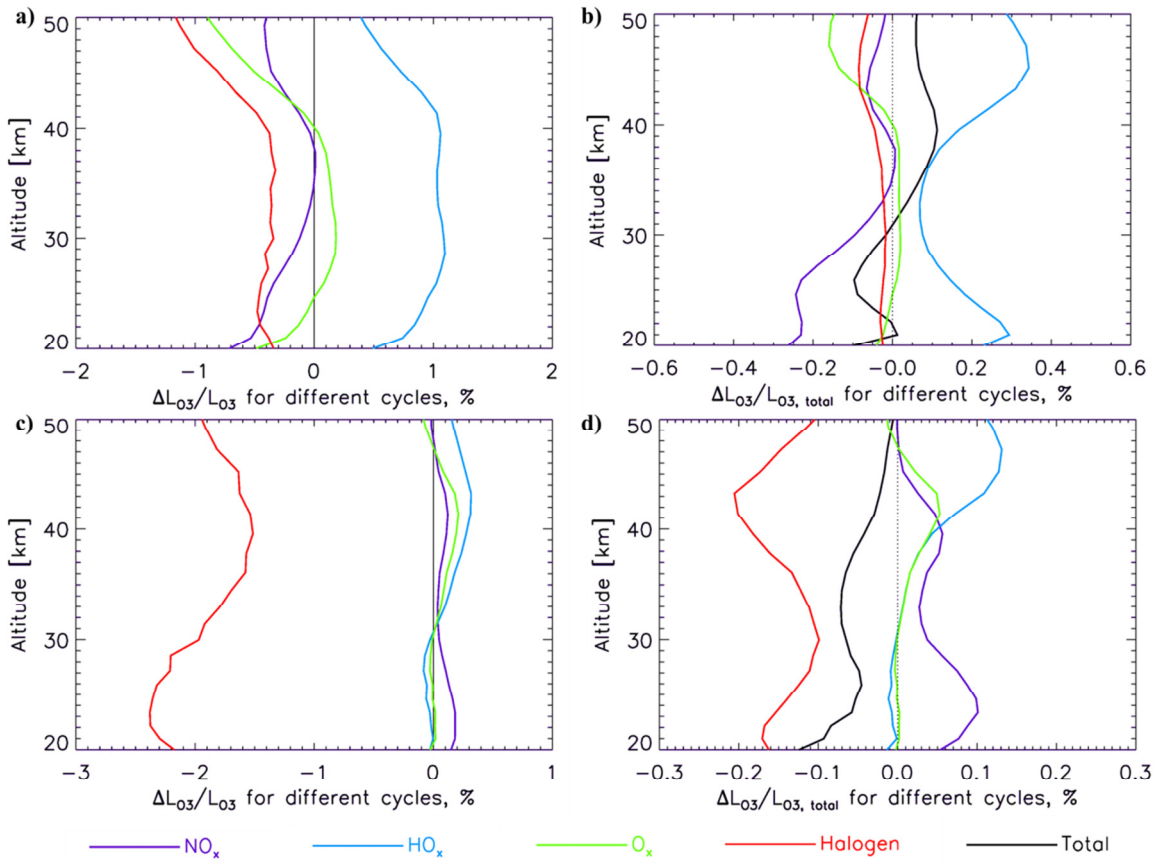


Figure 4.11 Changes in contributions of different catalytic $O_3$ destruction cycles to the total $O_3$ loss in the $H_2$-ICE scenarios compared to the Baseline scenario. Panels (a) and (b) are for A1FI and panels (c) and (d) are for B1. (a) and (c): % change in contribution of each catalytic cycle compared to its contribution in the BL; (b) and (d): % change in contributions of different catalytic $O_3$ destruction cycles compared to the total $O_3$ loss rate in BL. All figures are daily averaged values for the September equinox at 35ºN.

# CHAPTER 5: LOW-GWP ALTERNATIVES TO OZONE-DEPLETING SUBSTANCES

In this chapter key findings on atmospheric lifetimes and radiative forcing effects of the low-GWP alternatives to ozone depleting substances using 3-D global atmospheric models are presented, and comparisons with the previously-used simple estimation approach are discussed.

The reaction of each unsaturated halogenated hydrocarbons of interest with OH is added into the WACCM model, which is described in details in Chapter 2, along with the reaction rates obtained in laboratory studies available in previously published journal papers (listed in Table 5.1). It is assumed that emissions of each compound of interest in major regions of the world is proportional to the consumption of blowing agents in 2010 (Rajiv Singh, personal communication, 2011), and within each region emissions are constant through time and location. The annual emissions of each compound of interest are 3.4, 0.6, 4.8, 0.9, 0.5, 0.9, 1.6, and 2.7 Tg in the regions of the European Union, Japan, China, India, Turkey, the Middle East and North Africa, Latin America, and North America, respectively. The WACCM model simulation is run for five years for each compound of interest, assuming emission patterns described in Chapter 2. In addition, a reference WACCM simulation without any of these compounds of interest emissions is run in parallel to the perturbation runs.

The derived monthly averaged three-dimensional mixing ratio profiles of the fifth year WACCM simulation are input into the University of Illinois at Urbana-Champaign Radiative Transfer Model (UIUC RTM), which is described in details in Chapter 2. By comparing the

radiative forcings at tropopause derived from the perturbation runs and the reference run, the radiation effects of these proposed compounds are evaluated.

### 5.1. Atmospheric Lifetime

The atmospheric lifetime ($\tau_X$) of a gas X is determined as the ratio of its burden X in the atmosphere over the total sink of X. Lifetime can be calculated by integrating its burden and sink throughout the whole atmosphere, as shown in the following equation

$$\tau_X = \frac{\iint [X]_{V,t} N_{V,t} dV dt}{\iint k_{X+OH} [X]_{V,t} [OH]_{V,t} {N_{V,t}}^2 dV dt} \quad \text{(Eq. 5.1)}$$

Where $k_{X+OH}$ is the rate constant of the reaction of X and OH, $[X]_{V,t}$, $[OH]_{V,t}$, and $N_{V,t}$ the mixing ratios of X and OH and number of air molecules per unit volume, respectively, in the volume element of interest (V) at time t.

Table 5.2 lists the lifetimes for these compounds calculated from the WACCM model simulated results using the above equation. Among the six unsaturated halogenated hydrocarbons investigated here, HFO-1225ye(E) has the shortest lifetime of 9.2 days, while tCFP has the longest lifetime of 30.5 days. With lifetimes much shorter than six months, these compounds fall well into the category of very short-lived substances (VSLS) (WMO, 2007). Most of the compounds are degraded before being transported to remote regions as a direct result of their short atmospheric lifetimes, so the distribution of mixing ratios is very inhomogeneous throughout the atmosphere. Figure 5.1 shows the WACCM simulated steady-state annual mean zonal average mixing ratios. For each compound, the largest mixing ratios are near surface in the northern mid-latitudes, where human activity is most intensive and emissions are strongest. Mixing ratios decrease rapidly as the compounds move away from location of emissions because of their short lifetime. The longer its lifetime, the further the compound can reach into remote

regions with significant amount. For the assumed emissions scenario, mixing ratios of tCFP (lifetime 30.5 days) can reach more than 100 ppt in the northern mid- and high-latitudes below 8 km altitude, whereas 100 ppt HFO-1225ye(E) (lifetime 9.2 days) mixing ratio contour does not exceed 3 km altitude.

Table 5.2 also lists the lifetimes for these VSLS in the previous papers, calculated using the estimation approach by substituting the rate constant of the reaction X + OH obtained in laboratories and a global weighted-average OH concentration into the following equation.

$$\tau_X = \frac{1}{k_{X+OH} N_{OH}} \quad \text{(Eq. 5.2)}$$

where $N_{OH}$ is global weighted-average OH concentration. As OH concentrations in the atmosphere are highly variable, it does not make sense to use a globally-averaged OH concentration for such short-lived compounds; as will be shown in the coming discussion, the appropriate average would be species and emissions scenario dependent. In the previously published studies, a global weighted-average OH concentration of $1.0\times10^6$ molecules $cm^{-3}$ were used for HFO-1234yf, HFO-1234ze(E), HFO-1234ze(Z), and tCFP (Nielsen et al., 2007; Nilsson et al., 2009; Sondergaard et al., 2007; Sulbaek Andersen et al., 2008). Whereas for HFO-1225ye(E) and HFO-1225ye(Z), their lifetimes were scaled with that of $CH_3CCl_3$, whose lifetime is 6.1 years and the rate constant for its reaction with OH is $1.0\times10^{-14}$ $cm^3$ $molecules^{-1}$ $s^{-1}$ (Hurley et al., 2007). This scaling is equivalent to assuming a global weighted-average OH concentration of $5.2\times10^5$ molecules $cm^{-3}$. Hence, the globally weighted-average OH concentration are not consistent in the simple estimation approach used in these studies Furthermore, compared with the lifetimes derived from the 3-D atmospheric model simulations in the present study using a state-of-the-art atmospheric chemistry-climate model, using the estimation approach with a

global weighted-average OH concentration of $1.0\times10^6$ molecules $cm^{-3}$ leads to an underestimation of atmospheric lifetimes by 30%, 19%, 30%, and 15% for HFO-1234yf, HFO-1234ze(E), HFO-1234ze(Z), and tCFP, respectively; using a global weighted-average OH concentration of $5.2\times10^5$ molecules $cm^{-3}$, the estimation approach results an overestimation of atmospheric lifetimes by 29% and 9% for HFO-1225ye(Z) and HFO-1225(E), respectively (Table 5.2).

Here, an interesting question arises: What is the appropriate average OH concentration to derive the lifetimes the same as those derived from 3-D model simulations? Table 5.2 lists this pseudo average OH concentration for each compound of interest; these values range from 5.9 to $8.6\times10^5$ molecules $cm^{-3}$, indicating that assuming an global average OH concentration for very short-lived substances is not appropriate.

Equation 5.2 is actually a simplified form of Eq.5.1 if $k_{X+OH}$ is not dependent on temperature, and [X] is nearly constant throughout the atmosphere, as well as $N_{OH}$ satisfying the following equation

$$N_{OH} = \frac{\iint [OH]_{V,t} N_{V,t}^2 dVdt}{\iint N_{V,t} dVdt} \qquad \text{(Eq.5.3)}$$

However, [X] is highly variable in the atmosphere for very short-lived substances. Therefore, Eq.5.2 is inadequate to accurately calculate atmospheric lifetimes for very short-lived.

## 5.2. Global Warming Potentials

In the previously published studies (Hurley et al., 2007; Nielsen et al., 2007; Nilsson et al., 2009; Sondergaard et al., 2007; Sulbaek Andersen et al., 2008), the GWPs for these VSLS of interest are estimated through the Halocarbon Global Warming Potential (HGWP) over time

horizon $t_H$ defined as the ratio of the GWP for gas X to that for CFC-11, following the method by Pinnock et al. (1995)

$$GWP_X(t_H) = HGWP_X(t_H) \times GWP_{CFC-11}(t_H) \quad \text{(Eq. 5.4)}$$

$HGWP_X(t_H)$ for gas X is obtained by

$$HGWP_X(t_H) = \left(\frac{IF_X}{IF_{CFC-11}}\right)\left(\frac{\tau_X M_{CFC-11}}{\tau_{CFC-11} M_X}\right)\left(\frac{1-\exp(-t_H/\tau_X)}{1-\exp(-t_H/\tau_{CFC-11})}\right) \quad \text{(Eq. 5.5)}$$

where $M_X, M_{CFC-11}, \tau_X, \tau_{CFC-11}, IF_X$, and $IF_{CFC-11}$ are the molecular weights, atmospheric lifetimes, and instantaneous forcings for gas X and CFC-11, respectively. Note in the estimation approach the instantaneous forcings for the VSLS are calculated assuming constant mixing ratios in the atmosphere for the gas of interest.

The Global Warming Potential (GWP) is defined as the ratio of time-integrated radiative forcing over a select horizon after a pulse emission of gas X to that after a pulse emission of $CO_2$ of the same mass (IPCC, 1990), as an analogy to the Ozone Depleting Potential (ODP), first proposed by Wuebbles (1981) and well accepted as a measure of relative efficiency in depleting atmospheric ozone for ODSs. The time-integrated forcing for each gas is also called absolute GWP, or AGWP. It is well established that atmospheric concentration of a gas, whose sink is proportional to its concentration, will decay exponentially after emission into the atmosphere (except for $CO_2$, which is the sum of several exponentially decaying terms with different lifetimes). Accordingly, for a gas X whose efficiency in changing radiative forcing is proportional to its mass in the atmosphere, the radiative forcing caused by a pulse emission of one unit mass X, decays exponentially following

$$RF_p(t) = F_0 \exp\left(-\frac{t}{\tau_X}\right), \quad \text{(Eq. 5.6)}$$

where $F_0$ is the instantaneous radiative forcing at the time X is injected into the atmosphere, and $\tau_X$ atmospheric lifetime of X. Hence AGWP, or time-integrated radiative forcing, over time horizon $t_H$ for gas X can be derived as the following

$$AGWP = \int_0^{t_H} RF_p(t)\,dt = \int_0^{t_H} F_0 \exp(-\frac{t}{\tau_X})\,dt = F_0\tau_X\left[1 - \exp(-\frac{t_H}{\tau_X})\right]. \quad \text{(Eq. 5.7)}$$

The conventionally chosen time horizons for GWP comparisons are 20-, 100-, and 500-years (IPCC, 1990). The atmospheric lifetimes of these VSLS are no longer than 1 month, i.e. $t_H \ll \tau_X$ . Hence, for these VSLS

$$AGWP \cong F_0\tau_X. \quad \text{(Eq. 5.8)}$$

On the other hand, the UIUC RTM calculates the radiative forcing change due to sustained emission of a gas. The following deduction shows that the AGWP of X just equals the radiative forcing caused by sustained X emissions.

Considering a sustained emission such that one unit mass X is emitted in one unit time, the radiative forcing caused by such sustained emission at time t can be calculated

$$RF_s(t) = \int_0^t RF_p(u - t)\,du = \int_0^t F_0 \exp(-\frac{t-u}{\tau_X})\,du = F_0\tau_X\left[1 - \exp(-\frac{t}{\tau_X})\right]. \quad \text{(Eq. 5.9)}$$

If t is sufficiently longer than $\tau_X$, (as in the case of time-horizons chosen for VSLS GWP calculation)

$$RF_s \cong F_0\tau_X. \quad \text{(Eq. 5.10)}$$

The above derivation shows that, for a VSLS, both the AGWP and radiative forcing caused by sustained emission of the strength one unit mass per unit time can be approximated to

the product of $F_0$ and its atmospheric lifetime, which is readily calculated in the radiative transfer model and are listed in Table 5.3. GWPs over 20-, 100-, and 500-yr horizons for the six unsaturated halogenated hydrocarbons derived from the 3-D model method are listed in Table 5.4. The 100-yr GWPs are overestimated by 49% to 233% using the estimation approach.

For HFO-1225ye(Z) and HFO-1225(E), the 233% overestimation of their 100-yr GWPs using the estimation approach is a combined effect of their overestimated lifetimes and overestimated radiative efficiency assuming constant concentration profiles; for the other four compounds, even though the overestimation in radiative efficiency is partly offset by the underestimation of their lifetime, the overall effect is still an overestimation of 100-yr GWPs by more than 49%.

In order to estimate how much of the GWP differences come from the radiative transfer model used in this study and the scheme in the estimation approach in previous studies, experimental RTM simulations, in which the WACCM calculated VSLS burden in the atmosphere is homogeneously distributed in the atmosphere (i.e., constant mixing ratios in the troposphere and stratosphere), are carried out. The resulting radiative forcing changes on a per ppb basis are listed in Table 5.5 and compared with those reported in the previous studies. The differences are within 11%, confirming that the differences in derived GWPs come primarily from differences in assumed mixing ratio profiles and atmospheric lifetimes.

This study suggests that the 100-yr GWPs for these very short-lived unsaturated halogenated hydrocarbons are all less than 5. Scenarios of replacing HFCs with the low-GWP alternative are developed based on the needs for such compounds put together by Velders et al. (2009) with the assumptions that (i) productions and consumptions of HFCs decrease linearly

starting in 2015; (ii) productions and consumptions of HFC-32, -125, -143a, -245fa, and -365mfc decrease to zero in 2035; (iii) productions and consumptions of HFC-134a decrease to zero in 2025; (iv) the demands for refrigerants from use of HFC-32, -125, -134a, and -143a are replaced by HFO-1234yf, -1234ze(Z), -1225ye(Z), or -1225ye(E); (v) the demands for blowing agents from use of HFC-152a, -245fa, and -365mfc are replaced by HFO-1234ze(E), or tCFP. With these assumptions, the radiative forcing of the low-GWP alternatives in 2050 is between 0.26 and 0.80 mW $m^{-2}$ (Figure 5.2). As a result, radiative forcing from future needs for refrigerants, etc. is significantly reduced. In contrast to the monotonically increasing radiative forcing of long-lived HFCs that reaches 0.25 to 0.40 W $m^{-2}$ in 2050, radiative forcing of long-lived HFCs peaks at 46.3 to 53.5 mW $m^{-2}$ near 2030 and decreases to 26.1 to 31.3 mW $m^{-2}$ in 2050. The resulting saving in radiative forcing on climate in 2030 is between 0.04 and 0.07 W $m^{-2}$, comparable to the savings of the regulatory black carbon reduction measures, or a sizable fraction of the savings of the technological black carbon reduction measures and $CH_4$ reduction measures recently suggested by Shindell et al. (2012).

### 5.3. Conclusions

Atmospheric lifetimes and steady-state concentration profiles for six unsaturated halogenated hydrocarbons, which are prospective low-GWP ODSs alternatives, are calculated using a state-of-the-art three-dimensional numerical model that simulates the physical and chemical processes of the atmosphere, and realistic geographical emission pattern. The derived concentration profiles are input into a radiative transfer model to evaluate their radiation effects. Atmospheric lifetimes and GWPs for these compounds are obtained in this research. The atmospheric lifetimes of these compounds are less than a month, much shorter than those HFCs that are currently used or proposed to use. 100-year GWPs for these compounds are less than 5,

orders of magnitude smaller than those HFCs. These compounds may constitute a new generation of chemicals that are friendly both to the ozone layer and climate.

In addition, a methodology of evaluating GWPs for VSLS using three-dimensional global atmospheric models is presented in this research. Compared with those derived from the 3-D modeling method, 100-year GWPs for these alternative compounds are overestimated by 49% to 233% using the simple approach. The error comes from an oversimplified assumption of a global weighted-average OH concentration in atmospheric lifetime estimation, and an oversimplified assumption of constant concentration profiles in the atmosphere. Three-dimensional model simulations are necessary in accurate evaluation of GWPs for VSLS.

If the demands for HFCs are to be replaced with these low-GWP alternatives in 10 to 20 years starting 2015, radiative forcing saving (0.04 to 0.07 W $m^{-2}$) comparable to that due to the regulatory black carbon measures by Shindell et al. (2012) can be achieved in 2030. Radiative forcing of these low-GWP alternatives in 2050 is only 0.26 to 0.80 mW $m^{-2}$.

## 5.4. Figures and Tables

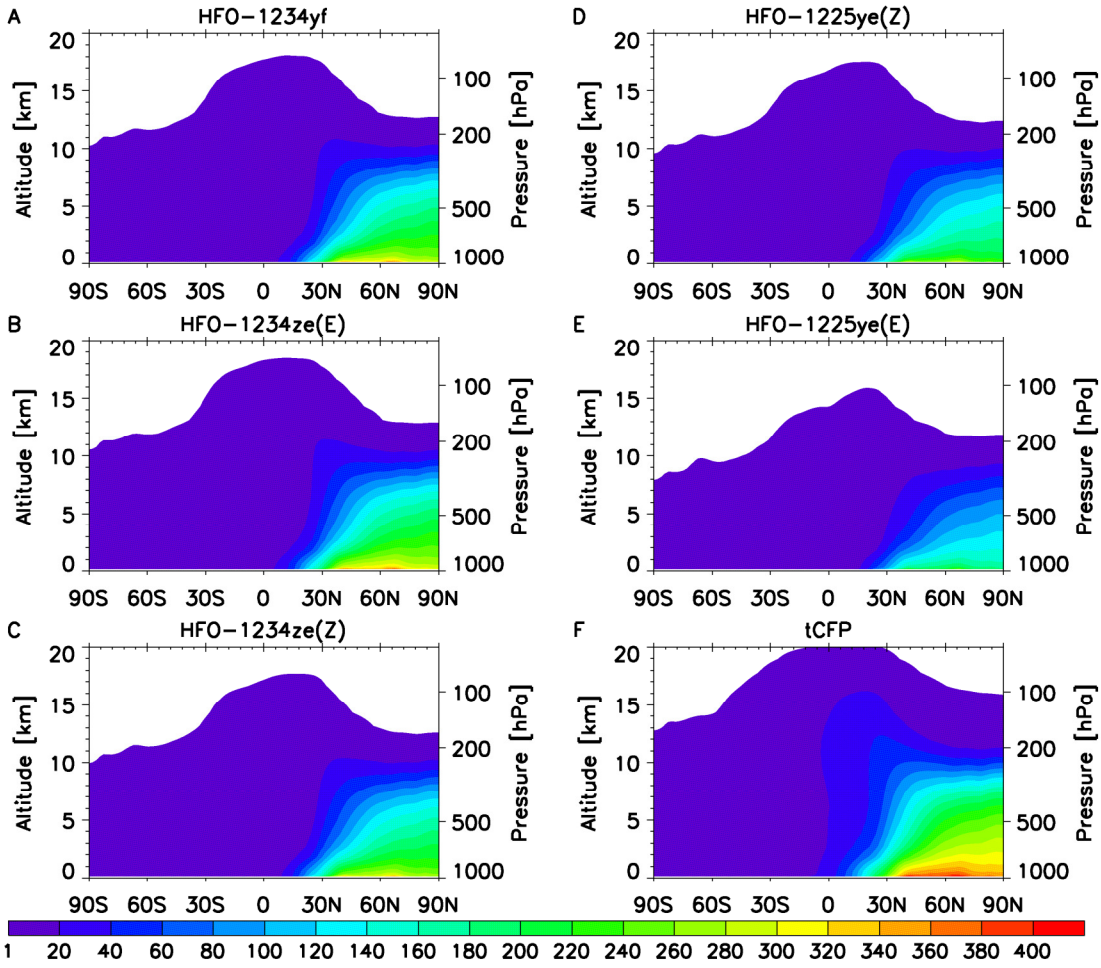


Figure 5.1. Annual-averaged zonal mean mixing ratios (in ppt by volume) for each of the six unsaturated halogenated hydrocarbons calculated by the WACCM model.

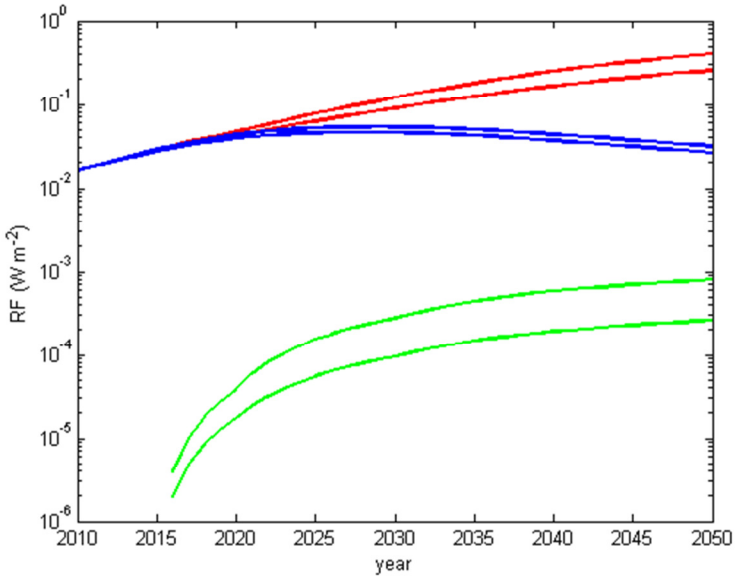


Figure 5.2. Range of radiative forcing of HFCs in the Velders scenario (red), and radiative forcing of low-GWP alternatives (green) and HFCs (blue) in the low-GWP replacement scenario as described in the main text.

Table 5.1 Rate constants for the reactions of the six unsaturated halogenated hydrocarbons and hydroxyl radical (OH) obtained from laboratory studies and their sources.

| compound | rate constant ($cm^3$ $molecules^{-1}$ $s^{-1}$) | source |
|---|---|---|
| HFO-1234yf | $(1.05\pm0.17)\times10^{-12}$ | Nielsen et al. (2007) |
| HFO-1234ze(E) | $(9.25\pm1.72)\times10^{-13}$ | Sondergaard et al. (2007) |
| HFO-1234ze(Z) | $(1.20\pm0.14)\times10^{-12}$ | Nilsson et al. (2009) |
| HFO-1225ye(Z) | $(1.22\pm0.14)\times10^{-12}$ | Hurley et al. (2007) |
| HFO-1225ye(E) | $(2.15\pm0.23)\times10^{-12}$ | Hurley et al. (2007) |
| tCFP | $(4.40\pm0.38)\times10^{-13}$ | Sulbaek Andersen et al. (2008) |

Table 5.2 Atmospheric lifetimes for the six unsaturated halogenated hydrocarbons derived from the 3-D model method, and from the estimation approach and errors of the estimation approach.

| compound | 3-D model method | the estimation approach | |
|---|---|---|---|
| | lifetime (days) | lifetime (days) | error |
| HFO-1234yf | 15.7 | 11 | -30% |
| HFO-1234ze(E) | 17.3 | 14 | -19% |
| HFO-1234ze(Z) | 14.2 | 10 | -30% |
| HFO-1225ye(Z) | 14.0 | 18 | +29% |
| HFO-1225ye(E) | 9.2 | 10 | +9% |
| tCFP | 30.5 | 26 | -15% |

Table 5.3 Changes in radiative forcing due to sustained 15.6 Tg/yr emission for each of the six unsaturated halogenated hydrocarbons and their AGWPs.

| compound | RF ($mW/m^{-2}$) | AGWP ($10^{-13}$ W yr $m^{-2}$ $kg^{-1}$) |
|---|---|---|
| HFO-1234yf | 2.72 | 1.75 |
| HFO-1234ze(E) | 3.94 | 2.53 |
| HFO-1234ze(Z) | 2.27 | 1.46 |
| HFO-1225ye(Z) | 2.40 | 1.54 |
| HFO-1225ye(E) | 1.28 | 0.82 |
| tCFP | 6.27 | 4.03 |

Table 5.4 GWPs over 20-, 100-, and 500-yr horizons for the six unsaturated halogenated hydrocarbons derived from the 3-D model method, and GWPs over 20- and 100-yr horizons from the estimation approach and errors of the estimation approach.

| compound | 3-D model method | | | The estimation approach | | | |
|---|---|---|---|---|---|---|---|
| | 20-yr | 100-yr | 500-yr | 20-yr | 20-yr error | 100-yr | 100-yr error |
| HFO-1234yf | 7.4 | 2.1 | 0.6 | 12 | +62% | 4 | +90% |
| HFO-1234ze(E) | 10.2 | 2.9 | 0.9 | 19 | +86% | 6 | +107% |
| HFO-1234ze(Z) | 5.9 | 1.7 | 0.5 | 10 | +69% | 3 | +76% |
| HFO-1225ye(Z) | 6.2 | 1.8 | 0.5 | 21 | +239% | 6 | +233% |
| HFO-1225ye(E) | 3.3 | 0.9 | 0.3 | 11 | +233% | 3 | +233% |
| tCFP | 16.3 | 4.7 | 1.4 | 26 | +60% | 7 | +49% |

Table 5.5 Instantaneous radiative forcing (in W $m^{-2}$ $ppb^{-1}$) for each of the six unsaturated halogenated hydrocarbons calculated following Pinnock et al. (1995) and calculated in the UIUC RTM, both assuming constant mixing ratio profiles for the compounds of interest.

| compound | Pinnock | UIUC RTM |
|---|---|---|
| HFO-1234yf | 0.22 | 0.20 |
| HFO-1234ze(E) | 0.27 | 0.24 |
| HFO-1234ze(Z) | 0.20 | 0.19 |
| HFO-1225ye(Z) | 0.25 | 0.23 |
| HFO-1225ye(E) | 0.24 | 0.23 |
| tCFP | 0.214 | 0.20 |

# CHAPTER 6: CONCLUSIONS AND FUTURE WORK

## 6.1. Conclusions

### *6.1.1. Impact of a Future Hydrogen Economy on Tropospheric Chemistry and Air Quality*

The possible impacts of transitioning to a $H_2$ powered road transportation sector in 2050 are evaluated using atmospheric chemistry-climate models and emissions scenarios based on the IPCC A1FI and B1 SRES growth scenarios and fuel cell and internal combustion engine technology options. The model simulation results show that air quality would improve significantly with adoption of a $H_2$ fuel cell type road transportation sector ($H_2$-FC scenarios). Primary gaseous (CO, $NO_x$) and particulate (soot) pollutants are reduced substantially once the fossil fuel based road transportation sector transitions to $H_2$ fuel cells. Ozone, a major secondary pollutant that often exceeds air quality standards in some regions of the United States (and is a severe problem in developing countries), would be reduced to a significant extent as its precursors, CO, $NO_x$ and NMVOCs emissions are reduced. Additionally, concentrations of particulate matter, especially those with diameter less than 2.5 μm ($PM_{2.5}$) would be significantly reduced in densely populated regions.

Some aspects of air quality would also improve with application of a $H_2$ internal combustion engine type road transportation sector ($H_2$-ICE scenarios). Ambient ozone concentrations would decrease slightly as its precursor emissions by fossil fuel combustion from road transportation sector are eliminated. Ozone mitigation with the $H_2$-ICE option is not nearly as effective as in the $H_2$-FC scenarios but is somewhat more effective in the relatively few VOC-limited regions. Urban $PM_{2.5}$ concentrations would not be significantly reduced except in eastern China.

For each specific type of $H_2$ technology applied in the road transportation sector, the reductions of key air pollution species are not as significant in the B1 scenario as in the A1FI scenario. However, since the emissions of key ozone and aerosol precursors are lower in the B1 scenarios, air quality in the B1 scenarios is generally better than that in the A1FI scenarios. For example, tropospheric ozone concentrations are substantially lower in all of the B1 scenarios than in all of the A1FI scenarios regardless of the $H_2$ technology adopted.

With a leakage rate of 2.5%, $H_2$ emissions in a $H_2$-based road transportation sector are larger than the replaced $H_2$ emissions from fossil fuel burning, leading to increased $H_2$ concentrations in the atmosphere. The added $H_2$ would decrease tropospheric OH abundance, resulting in elongated $CH_4$ lifetime and thus warming. However, when taking changes in emissions of CO, $NO_x$ and NMVOCs into account, the picture of the climate impact is more complicated. In the $H_2$-FC scenarios, the combined effect of emission changes is a 4% decrease in OH abundance, which contributes to warming by increasing $CH_4$ lifetime. On the other hand, concurrent decrease in tropospheric $O_3$ concentrations would provide a cooling mechanism. The overall effect is further complicated by the temporal and spatial inhomogeneity of the two offsetting mechanisms. In the $H_2$-ICE scenarios, both decrease in $CH_4$ lifetime due to OH increase and the decrease in tropospheric $O_3$ tend to cool the climate while, again, inhomogeneities in space and time would complicate the problem.

It is worth noting that the emission scenarios are assumed 100% market penetration of $H_2$ technologies in 2050. That is, all vehicles operating on road are replaced with $H_2$ powered ones. It is also assumed that the $H_2$ for road transportation is produced by renewable, nuclear, or fossil fuel facilities with advanced scrubbing technologies with no emissions associated with its production. The positive and negative impacts presented here will decrease in magnitude to the

extent that market penetration is not total and if there are emissions associated with $H_2$ production.

*6.1.2. Impact of a Future Hydrogen Economy on Stratospheric Ozone*

In this study the possible impact of a future $H_2$-based road transportation sector on stratospheric composition and chemistry is investigated through chemistry-climate model simulations of the 2050 atmosphere based on several emission scenarios designed to bracket the possible future changes in emissions. These scenarios are based on the IPCC high (A1FI) and low (B1) emitting paths. In addition, the impacts of two $H_2$ technology options are assessed: utilizing $H_2$ in fuel cells and utilizing $H_2$ in internal combustion engines.

These MOZART simulation results suggest that future implementation of a $H_2$-based road transportation sector would perturb stratospheric chemistry, by means of affecting catalytic ozone destruction cycles involving $HO_x$, $NO_x$, and halogens. The magnitude of the impact depends on the future growth path as well as the $H_2$ technology adopted. In general the impact is larger for the A1FI based scenarios than the corresponding B1 based scenarios, and the $H_2$-FC scenarios result in more ozone loss than the $H_2$-ICE scenarios. The impact on global stratospheric column ozone is considerable for the A1FI scenarios (-0.54% for $H_2$-FC and -0.23% for $H_2$-ICE) and for the B1 $H_2$-FC scenario (-0.20%) while there is a slight increase (0.04%) for the B1 $H_2$-ICE scenario. The largest relative reduction of ozone concentration occurs in the lower stratosphere where $HO_x$ cycles dominate $O_3$ loss and impact from the underlying troposphere is prominent. In the middle stratosphere ozone concentrations increase slightly while at higher altitudes they either decrease slightly or increase slightly depending on scenarios. These changes have relatively little impact on column ozone since ozone at this level only makes up a small fraction in terms of column ozone, due to the low ozone number concentration there. It is

important to note that the chosen emission scenarios are developed with a 100% market penetration assumption. Less impact on stratospheric ozone is possible in the case of an intermediate market penetration.

It is important to note that even though a $H_2$-based road transportation sector is likely to decrease stratospheric ozone, this reduction is considerably less than the ozone recovery due to the reductions in ozone depleting substances, e.g., CFCs, from the atmosphere in 2050. In terms of total column ozone, the MOZART simulations results suggest that there would still be 4%~5% more ozone in the 2050 atmosphere with a $H_2$-based road transportation sector than that in today's atmosphere. Therefore, the ozone reduction due to a $H_2$-based road transportation sector should not constitute a major concern on stratospheric ozone and increased UV radiation at the surface in 2050.

*6.1.3. Low-GWP Alternatives to ODSs*

Atmospheric lifetimes and steady-state concentration profiles for six unsaturated halogenated hydrocarbons, which are prospective low-GWP ODSs alternatives, are calculated using a state-of-the-art three-dimensional numerical model that simulates the physical and chemical processes of the atmosphere, and realistic geographical emission pattern. The derived concentration profiles are input into a radiative transfer model to evaluate their radiation effects. Atmospheric lifetimes and GWPs for these compounds are obtained in this research. The atmospheric lifetimes of these compounds are less than a month, much shorter than those HFCs that are currently used or proposed to use. 100-year GWPs for these compounds are less than 5, orders of magnitude smaller than those HFCs. These compounds may constitute a new generation of chemicals that are friendly both to the ozone layer and climate.

In addition, a methodology of evaluating GWPs for VSLS using three-dimensional global atmospheric models is presented in this research. Compared with those derived from the 3-D modeling method, 100-year GWPs for these alternative compounds are overestimated by 49% to 233% using the simple approach. The error comes from an oversimplified assumption of a global weighted-average OH concentration in atmospheric lifetime estimation, and an oversimplified assumption of constant concentration profiles in the atmosphere. Three-dimensional model simulations are necessary in accurate evaluation of GWPs for VSLS.

If the demands for HFCs are to be replaced with these low-GWP alternatives in 10 to 20 years starting 2015, radiative forcing saving (0.04 to 0.07 W $m^{-2}$) comparable to that due to the regulatory black carbon measures by Shindell et al. (2012) can be achieved in 2030. Radiative forcing of these low-GWP alternatives in 2050 is only 0.26 to 0.80 mW $m^{-2}$.

## 6.2. Future Work

Work accomplished in this research provides opportunities to several topics of future work. Some examples are discussed below:

### *6.2.1. Hydrogen Economy*

This study focuses on the environmental impact of emission changes in a future hydrogen economy, whereas chemistry-climate interactions may play a key role as well. In future studies the environmental impact of a hydrogen economy can be analyzed taking chemistry-climate interactions into account, in order to establish a fuller knowledge on hydrogen economy.

In addition, it is projected more people will live in megacities in the coming decades. The air quality and climate-forcing agents emissions in megacities have drawn researchers' attention (Parrish and Zhu, 2009). As discussed in this research, hydrogen economy has the potential to

tackle these problems. Future research can focus on cost-benefit analysis of a hydrogen economy for megacities, and provide guidance for relevant policymakers.

### *6.2.2. Low-GWP Alternatives to ODSs*

Plans of replacing HCFCs and HFCs with the low-GWP alternative compounds discussed in this study can be formulated based on comprehensive reviews of the environmental, economic and technological facets of the replacement processes. Such plans can work as guidance by international treaties to tackle climate change in the coming decades.

## REFERENCES


Abe, R.: Recent progress on photocatalytic and photoelectrochemical water splitting under visible light irradiation, J. Photoch. Photobio. C, 11, 179-209, 2010.

Appel, K. W., Gilliland, A. B., Sarwar, G., and Gilliam, R. C.: Evaluation of the Community Multiscale Air Quality (CMAQ) model version 4.5: Sensitivities impacting model performance Part I - Ozone, Atmos. Environ., 41, 9603-9615, 2007.

Appel, K. W., Bhave, P. V., Gilliland, A. B., Sarwar, G., and Roselle, S. J.: Evaluation of the community multiscale air quality (CMAQ) model version 4.5: Sensitivities impacting model performance; Part II - particulate matter, Atmos. Environ., 42, 6057-6066, 2008.

Atkinson, R., Baulch, D. L., Cox, R. A., Crowley, J. N., Hampson, R. F., Hynes, R. G., Jenkin, M. E., Rossi, M. J., Troe, J. and Wallington, T. J.: Evaluated kinetic and photochemical data for atmospheric chemistry: Volume IV - gas phase reactions of organic halogen species, Atmos. Chem. Phys., 8, 4141-4496, 2008.

Barnes, D. H., Wofsy, S. C., Fehlau, B. P., Gottlieb, E. W., Elkins, J. W., Dutton, G. S., and Novelli, P. C.: Hydrogen in the atmosphere: Observations above a forest canopy in a polluted environment, J. Geophys. Res., 108, 2003.

Bond, T. C., Streets, D. G., Yarber, K. F., Nelson, S. M., Woo, J. H., and Klimont, Z.: A technology-based global inventory of black and organic carbon emissions from combustion, J. Geophys. Res., 109, D14203, 2004.

Brown, J. S., Zilio, C. and Cavallini, A.: The fluorinated olefin R-1234ze(Z) as a high-temperature heat pumping refrigerant, International Journal of Refrigeration-Revue Internationale Du Froid, 32, 1412-1422, 2009.

Byun, D. and Schere, K. L.: Review of the governing equations, computational algorithms, and other components of the models-3 Community Multiscale Air Quality (CMAQ) modeling system, Appl. Mech. Rev., 59, 51-77, 2006.

Colella, W. G., Jacobson, M. Z., and Golden, D. M.: Switching to a US hydrogen fuel cell vehicle fleet: The resultant change in emissions, energy use, and greenhouse gases, J. Power Sources, 150, 150-181, 2005.

Conrad, R. and Seiler, W.: Influence of Temperature, Moisture, and Organic-Carbon on the Flux of $H_2$ and CO between Soil and Atmosphere: Field Studies in Sub-Tropical Regions, J. Geophys. Res., 90, 5699-5709, 1985.

Constant, P., Poissant, L., and Villemur, R.: Annual hydrogen, carbon monoxide and carbon dioxide concentrations and surface to air exchanges in a rural area (Québec, Canada), Atmos. Environ., 42, 5090-5100, 2008.

Constant, P., Poissant, L., and Villemur, R.: Tropospheric $H_2$ budget and the response of its soil uptake under the changing environment, Sci. Total Environ., 407, 1809-1823, 2009.

Deboer, P. C. T., Mclean, W. J. and Homan, H. S.: Performance and Emissions of Hydrogen Fueled Internal-Combustion Engines, Int J Hydrogen Energy, 1, 153-172, 1976.

Derwent, R., Simmonds, P., O'Doherty, S., Manning, A., Collins, W., and Stenvenson, D.: Global environmental impacts of the hydrogen economy, Int. J. Nucl. Hydrogen Prod. Appl., Vol. 1, No. 1, 2006.

Ehhalt, D. H. and Rohrer, F.: The tropospheric cycle of $H_2$: a critical review, Tellus B, 61, 500-535, 2009.

Eyring, V., T. G. Shepherd, and D. W. Waugh (Eds.): Stratospheric Processes And Their Role in Climate Report on the Evaluation of Chemistry-Climate Models (SPARC CCMVal). SPARC Report No. 5, WCRP-132, WMO/TD-No. 1526, accessed at http://www.atmosp.physics.utoronto.ca/SPARC, 2010.

Granier, C., Lamarque, J. F., Mieville, A., Muller, J. F., Olivier, J., Orlando J., Peters, J., Petron, G., Tyndall, G., and Wallens, S.: POET, a database of surface emissions of ozone precursors, available at: http://www.aero.jussieu.fr/projet/ACCENT/POET.php, 2005.

Gettelman, A., Kinnison, D. E., Dunkerton, T. J., and Brasseur, G. P.: Impact of monsoon circulations on the upper troposphere and lower stratosphere, J. Geophys. Res., 109, D22101, 2004.

Gettelman, A., M. I. Hegglin, S. W. Son, M. Fujiwara, S. Tilmes, L. Pan, P. Hoor, H. Lee, G. L. Manney, T. Birner, G. Stiller, M. Rex, S. Kremser, D. Wuebbles, K. A. Walker, and J. A. Anel: Upper Troposphere and Lower Stratosphere, in Stratospheric Processes And Their Role in Climate Report on the Evaluation of Chemistry-Climate Models (SPARC CCMVal), edited by V. Eyring, T. G. Shepherd, and D. W. Waugh, pp. 253-304, World Meteorological Organization, SPARC Report No. 5, WCRP-132, WMO/TD-No. 1526, World Climate Research Programme, accessed through http://www.atmosp.physics.utoronto.ca/SPARC, 2010.

Horowitz, L. W., Walters, S., Mauzerall, D. L., Emmons, L. K., Rasch, P. J., Granier, C., Tie, X. X., Lamarque, J. F., Schultz, M. G., Tyndall, G. S., Orlando, J. J., and Brasseur, G. P.: A global simulation of tropospheric ozone and related tracers: Description and evaluation of MOZART, version 2, J. Geophys. Res., 108, 2003.

Huang, H. C., Lin, J. T., Tao, Z. N., Choi, H., Patten, K., Kunkel, K., Xu, M., Zhu, J. H., Liang, X. Z., Williams, A., Caughey, M., Wuebbles, D. J., and Wang, J. L.: Impacts of long-range transport of global pollutants and precursor gases on US air quality under future climatic conditions, J. Geophys. Res., 113, 2008.

Hurley, M. D., Ball, J. C. and Wallington, T. J.: Atmospheric chemistry of the Z and E isomers of CF3CF=CHF; Kinetics, mechanisms, and products of gas-phase reactions with Cl atoms, OH radicals, and O-3, J Phys Chem A, 111, 9789-9795, 2007.

Intergovernmental Panel on Climate Change (IPCC): Special Report on Emissions Scenarios. Working Group III, IPCC, Cambridge University Press, Cambridge, 2000.

Intergovernmental Panel on Climate Change (IPCC): Climate Change 2001, the Scientific Basis. Contribution of Working Group 1 to the Third Assessment Report of the IPCC, Cambridge University Press, Cambridge, UK and New York, NY, USA, 881 pp, 2001.

Intergovernmental Panel on Climate Change (IPCC): Climate Change 2007, the Scientific Basis. Contribution of Working Group 1 to the Fourth Assessment Report of the IPCC, Cambridge University Press, Cambridge, UK and New York, NY, USA, 996 pp, 2007.

Jacobson, M. Z., Colella, W. G., and Golden, D. M.: Cleaning the air and improving health with hydrogen fuel-cell vehicles, Science, 308, 1901-1905, 2005.

Jacobson, M. Z.: Effects of wind-powered hydrogen fuel cell vehicles on stratospheric ozone and global climate, Geophys. Res. Lett., 35, L19803, 2008.

Jain, A. K., Briegleb, B. P., Minschwaner, K. and Wuebbles, D. J.: Radiative forcings and global warming potentials of 39 greenhouse gases, Journal of Geophysical Research-Atmospheres, 105, 20773-20790, 2000.

Johnson, H.: Hydrogen Embrittlement, Science, 179, 228-&, 1973.

Kim, Y. and Logan, B. E.: Hydrogen production from inexhaustible supplies of fresh and salt water using microbial reverse-electrodialysis electrolysis cells, Proc. Natl. Acad. Sci. U. S. A., 108, 16176-16181, 2011.

Kinnison, D. E., Brasseur, G. P., Walters, S., Garcia, R. R., Marsh, D. R., Sassi, F., Harvey, V. L., Randall, C. E., Emmons, L., Lamarque, J. F., Hess, P., Orlando, J. J., Tie, X. X., Randel, W., Pan, L. L., Gettelman, A., Granier, C., Diehl, T., Niemeier, U., and Simmons, A. J.: Sensitivity of chemical tracers to meteorological parameters in the MOZART-3 chemical transport model, J. Geophys. Res., 112, 2007.

Ko, M. K. W., Mcelroy, M. B., Weisenstein, D. K., and Sze, N. D.: Lightning: a Possible Source of Stratospheric Odd Nitrogen, J. Geophys. Res., 91, 5395-5404, 1986.

Kulawik, S. S., Worden, H., Osterman, G., Luo, M., Beer, R., Kinnison, D. E., Bowman, K. W., Worden, J., Eldering, A., Lampel, M., Steck, T., and Rodgers, C. D.: TES atmospheric profile retrieval characterization: An orbit of simulated observations, IEEE Trans. Geosci. Rem. Sens., 44, 1324-1333, 2006.

Lamarque, J. F., Kiehl, J. T., Hess, P. G., Collins, W. D., Emmons, L. K., Ginoux, P., Luo, C., and Tie, X. X.: Response of a coupled chemistry-climate model to changes in aerosol emissions: Global impact on the hydrological cycle and the tropospheric burdens of OH, ozone, and NOx, Geophys. Res. Lett., 32, 2005.

Liang, X. Z., Kunkel, K. E., and Samel, A. N.: Development of a regional climate model for US Midwest applications. Part I: Sensitivity to buffer zone treatment, J. Clim., 14, 4363-4378, 2001.

Liebl, K.H., and Seiler, W.: CO and H2 destruction at the soil surface, Microbial Production and Utilization of Gases, edited by Schlegel, H. G., Gottschalk, G., and Pfenning, N., Goltze, Gottingen, Germany, pp. 215-229, 1976.

Lin, J. T., Patten, K. O., Hayhoe, K., Liang, X. Z., and Wuebbles, D. J.: Effects of future climate and biogenic emissions changes on surface ozone over the United States and China, J. Appl. Meteorol. Clim., 47, 1888-1909, 2008a.

Lin, J., Wuebbles, D. J., and Liang, X.: Effects of intercontinental transport on surface ozone over the United States: Present and future assessment with a global model, Geophys. Res. Lett., 35, L02805, 2008b.

Liu, C., Liu, Y., Cai, Z., Gao, S., Lu, D., and Kyrola, E.: A Madden-Julian Oscillation-triggered record ozone minimum over the Tibetan Plateau in December 2003 and its association with stratospheric "low-ozone pockets", Geophys. Res. Lett., 36, L15830, 2009.

Liu, Y., Liu C., Tie, X., and Gao S.: Middle stratospheric polar vortex ozone budget during the warming Arctic winter, 2002-2003, Adv. Atmos. Sci., 28, 985-996, 2011.

Luecken, D. J., Phillips, S., Sarwar, G., and Jang, C.: Effects of using the CB05 vs. SAPRC99 vs. CB4 chemical mechanism on model predictions: Ozone and gas-phase photochemical precursor concentrations, Atmos. Environ., 42, 5805-5820, 2008.

Murphy, D. M., Fahey, D. W., Proffitt, M. H., Liu, S. C., Chan, K. R., Eubank, C. S., Kawa, S. R., and Kelly, K. K.: Reactive Nitrogen and its Correlation with Ozone in the Lower Stratosphere and Upper Troposphere, J. Geophys. Res., 98, 8751-8773, 1993.

Naik, V., Jain, A. K., Patten, K. O. and Wuebbles, D. J.: Consistent sets of atmospheric lifetimes and radiative forcings on climate for CFC replacements: HCFCs and HFCs, Journal of Geophysical Research-Atmospheres, 105, 6903-6914, 2000.

Nevison, C. D., Solomon, S., and Gao, R. S.: Buffering interactions in the modeled response of stratospheric $O_3$ to increased NOx and HOx, J. Geophys. Res., 104, 3741-3754, 1999.

Nielsen, O. J., Javadi, M. S., Sulbaek Andersen, M. P., Hurley, M. D., Wallington, T. J. and Singh, R.: Atmospheric chemistry of CF3CF=CH2: Kinetics and mechanisms of gas-phase reactions with Cl atoms, OH radicals, and O-3, Chemical Physics Letters, 439, 18-22, 2007.

Nilsson, E. J. K., Nielsen, O. J., Johnson, M. S., Hurley, M. D. and Wallington, T. J.: Atmospheric chemistry of cis-CF(3)CH=CHF: Kinetics of reactions with OH radicals and O(3) and products of OH radical initiated oxidation, Chemical Physics Letters, 473, 233-237, 2009.

Novelli, P. C., Lang, P. M., Masarie, K. A., Hurst, D. F., Myers, R., and Elkins, J. W.: Molecular hydrogen in the troposphere: Global distribution and budget, J. Geophys. Res., 104, 30427-30444, 1999.

Olivier J., Peters, J., Granier, C., Petron, G., Muller, J. F., and Wallens, S.: Present and future surface emissions of atmospheric compounds, POET report #2, EU project EVK2-1999-00011, 2003.

Pan, L. L., Wei, J. C., Kinnison, D. E., Garcia, R. R., Wuebbles, D. J., and Brasseur, G. P.: A set of diagnostics for evaluating chemistry-climate models in the extratropical tropopause region RID A-9296-2008, J. Geophys. Res., 112, D09316, 2007.

Park, M., Randel, W., Kinnison, D., Garcia, R., and Choi, W.: Seasonal variation of methane, water vapor, and nitrogen oxides near the tropopause: Satellite observations and model simulations, J. Geophys. Res., 109, D03302, 2004.

Parrish, D. D. and Zhu, T.: Clean Air for Megacities, Science, 326, 674-675, 2009.

Patten, K. O. and Wuebbles, D. J.: Atmospheric lifetimes and Ozone Depletion Potentials of trans-1-chloro-3,3,3-trifluoropropylene and trans-1,2-dichloroethylene in a three-dimensional model, Atmospheric Chemistry and Physics, 10, 10867-10874, 2010.

Patten, K. O., Khamaganov, V. G., Orkin, V. L., Baughcum, S. L. and Wuebbles, D. J.: OH reaction rate constant, IR absorption spectrum, ozone depletion potentials and global warming potentials of 2-bromo-3,3,3-trifluoropropene, Journal of Geophysical Research-Atmospheres, 116, D24307, 2011.

Pfister, G. G., Hess, P. G., Emmons, L. K., Rasch, P. J., and Vitt, F. M.: Impact of the summer 2004 Alaska fires on top of the atmosphere clear-sky radiation fluxes, J. Geophys. Res., 113, 2008.

Pinnock, S., Hurley, M. D., Shine, K. P., Wallington, T. J. and Smyth, T. J.: Radiative Forcing of Climate by Hydrochlorofluorocarbons and Hydrofluorocarbons, Journal of Geophysical Research-Atmospheres, 100, 23227-23238, 1995.

Prather, M. J.: An environmental experiment with H2?, Science, 302, 581-582, 2003.

Price, H., Jaegle, L., Rice, A., Quay, P., Novelli, P. C., and Gammon, R.: Global budget of molecular hydrogen and its deuterium content: Constraints from ground station, cruise, and aircraft observations, J. Geophys. Res., 112, D22108, 2007.

Rothman, L. S., Jacquemart, D., Barbe, A., Benner, D. C., Birk, M., Brown, L. R., Carleer, M. R., Chackerian, C., Chance, K., Coudert, L. H., Dana, V., Devi, V. M., Flaud, J. M., Gamache, R. R., Goldman, A., Hartmann, J. M., Jucks, K. W., Maki, A. G., Mandin, J. Y., Massie, S. T., Orphal, J., Perrin, A., Rinsland, C. P., Smith, M. A. H., Tennyson, J., Tolchenov, R. N., Toth, R. A., Vander Auwera, J., Varanasi, P. and Wagner, G.: The HITRAN 2004 molecular spectroscopic database, J. Quant. Spectrosc. Radiat. Transfer, 96, 139-204, 2005.

Sander, S. P., R. R. Friedl, D. M. Golden, M. J. Kurylo, G. K. Moortgat, H. Keller-Rudek, P. H. Wine, A. R. Ravishankara, C. E. Kolb, M. J. Molina, B. J. Finlayson-Pitts, R. E. Huie, and V. L. Orkin: Chemical Kinetics and Photochemical Data for Use in Atmospheric Studies, Evaluation Number 15, JPL Publication 06-2, NASA Panel for Data Evaluation, Jet Propulsion Laboratory, California Institute of Technology, Pasadena, California, July 10. Available at: http://jpldataeval.jpl.nasa.gov, 2006.

Sarwar, G., Luecken, D., Yarwood, G., Whitten, G. Z., and Carter, W. P. L.: Impact of an updated carbon bond mechanism on predictions from the CMAQ modeling system: Preliminary assessment, J. Appl. Meteorol. Clim., 47, 3-14, 2008.

Sassi, F., Boville, B. A., Kinnison, D., and Garcia, R. R.: The effects of interactive ozone chemistry on simulations of the middle atmosphere, Geophys. Res. Lett., 32, L07811, 2005.

Schultz, M. G., Diehl, T., Brasseur, G. P., and Zittel, W.: Air pollution and climate-forcing impacts of a global hydrogen economy, Science, 302, 624-627, 2003.

Seiler, W. and Zankl, H.: Die Spurengase CO und H2 uber Munchen, Umschau, 75 (23), 735-736, 1975.

Shindell, D., Kuylenstierna, J. C. I., Vignati, E., van Dingenen, R., Amann, M., Klimont, Z., Anenberg, S. C., Muller, N., Janssens-Maenhout, G., Raes, F., Schwartz, J., Faluvegi, G., Pozzoli, L., Kupiainen, K., Hoeglund-Isaksson, L., Emberson, L., Streets, D., Ramanathan, V., Hicks, K., Oanh, N. T. K., Milly, G., Williams, M., Demkine, V. and Fowler, D.: Simultaneously Mitigating Near-Term Climate Change and Improving Human Health and Food Security, Science, 335, 183-189, 2012.

Shine, K. P., Fuglestvedt, J. S., Hailemariam, K. and Stuber, N.: Alternatives to the global warming potential for comparing climate impacts of emissions of greenhouse gases, Clim. Change, 68, 281-302, 2005.

Simmonds, P. G., Derwent, R. G., O'Doherty, S., Ryall, D. B., Steele, L. P., Langenfelds, R. L., Salameh, P., Wang, H. J., Dimmer, C. H., and Hudson, L. E.: Continuous high-frequency observations of hydrogen at the Mace Head baseline atmospheric monitoring station over the 1994-1998 period, J. Geophys. Res., 105, 12105-12121, 2000.

Smith-Downey, N. V., Randerson, J.T., and Eiler, J.M.: Molecular hydrogen uptake by soils in forest, desert, and marsh ecosystems in California, J. Geophys. Res., 113. doi:10.1029/2008JG000701, 2008.

Sondergaard, R., Nielsen, O. J., Hurley, M. D., Wallington, T. J. and Singh, R.: Atmospheric chemistry of trans-CF3CH = CHF: Kinetics of the gas-phase reactions with Cl atoms, OH radicals, and O-3, Chemical Physics Letters, 443, 199-204, 2007.

Sulbaek Andersen, M. P., Nilsson, E. J. K., Nielsen, O. J., Johnson, M. S., Hurley, M. D. and Wallington, T. J.: Atmospheric chemistry of trans-CF(3)CH = CHCl: Kinetics of the gas-phase reactions with Cl atoms, OH radicals, and O(3), Journal of Photochemistry and Photobiology A-Chemistry, 199, 92-97, 2008.

Tie, X. X., Madronich, S., Walters, S., Edwards, D. P., Ginoux, P., Mahowald, N., Zhang, R. Y., Lou, C., and Brasseur, G.: Assessment of the global impact of aerosols on tropospheric oxidants, J. Geophys. Res., 110, 2005.

Tromp, T. K., Shia, R. L., Allen, M., Eiler, J. M., and Yung, Y. L.: Potential environmental impact of a hydrogen economy on the stratosphere, Science, 300, 1740-1742, 2003.

United Nations Environment Programme (UNEP): HFCs: A Critical Link in Protecting Climate and the Ozone Layer, 2011.

United States Environmental Protection Agency (U.S. EPA): Air Emissions by Pollutant, available at: http://www.epa.gov/air/emissions/, 2009.

van der Werf, G. R., Randerson, J. T., Giglio, L., Collatz, G. J., Kasibhatla, P. S., and Arellano, A. F.: Interannual variability in global biomass burning emissions from 1997 to 2004, Atmos. Chem. Phys., 6, 3423-3441, 2006.

Velders, G. J. M., Fahey, D. W., Daniel, J. S., McFarland, M. and Andersen, S. O.: The large contribution of projected HFC emissions to future climate forcing, Proc. Natl. Acad. Sci. U. S. A., 106, 10949-10954, 2009.

Velders, G. J. M., Ravishankara, A. R., Miller, M. K., Molina, M. J., Alcamo, J., Daniel, J. S., Fahey, D. W., Montzka, S. A. and Reimann, S.: Preserving Montreal Protocol Climate Benefits by Limiting HFCs, Science, 335, 922-923, 2012.

Vollmer, M. K., Juergens, N., Steinbacher, M., Reimann, S., Weilenmann, M., and Buchmann, B.: Road vehicle emissions of molecular hydrogen (H2) from a tunnel study, Atmos. Environ., 41, 8355-8369, 2007.

Warwick, N. J., Bekki, S., Nisbet, E. G., and Pyle, J. A.: Impact of a hydrogen economy on the stratosphere and troposphere studied in a 2-D model, Geophys. Res. Lett., 31, L05107, 2004.

Wennberg, P. O., Cohen, R. C., Stimpfle, R. M., Koplow, J. P., Anderson, J. G., Salawitch, R. J., Fahey, D. W., Woodbridge, E. L., Keim, E. R., Gao, R. S., Webster, C. R., May, R. D., Toohey, D. W., Avallone, L. M., Proffitt, M. H., Loewenstein, M., Podolske, J. R., Chan, K. R., and Wofsy, S. C.: Removal of Stratospheric O3 by Radicals: In-Situ Measurements of OH, HO2, NO, NO2, ClO, and BrO, Science, 266, 398-404, 1994.

World Meteorological Organization (WMO): Scientific Assessment of Ozone Depletion: 1994, WMO Rep.37, Geneva, 1995.

World Meteorological Organization (WMO): Scientific Assessment of Ozone Depletion: 2002, WMO Rep.47, Geneva, 2003.

World Meteorological Organization (WMO): Scientific Assessment of Ozone Depletion: 2010, WMO Rep.52, Geneva, 2011.

World Health Organization/Europe (WHO/Europe): Health aspects of air pollution with particulate matter, ozone and nitrogen dioxide: Report on a WHO working group, Bonn, Germany, 2003.

Wu, S., Mickley, L. J., Jacob, D. J., Rind, D., and Streets, D. G.: Effects of 2000-2050 changes in climate and emissions on global tropospheric ozone and the policy-relevant background surface ozone in the United States, J. Geophys. Res., 113, D18312, 2008.

Wuebbles, D.J.: The relative efficiency of a number of halocarbons for destroying stratospheric ozone. Lawrence Livermore National Laboratory report UCID-18924, 1981.

Wuebbles, D., Patten, K., Johnson, M. and Kotamarthi, R.: New methodology for Ozone Depletion Potentials of short-lived compounds: n-propyl bromide as an example, J. Geophys. Res. -Atmos., 106, 14551-14571, 2001.

Yonemura, S., Kawashima, S., and Tsuruta, H.: Continuous measurements of CO and H2 deposition velocities onto an andisol: uptake control by soil moisture, Tellus B, 51, 688-700, 1999.

Yonemura, S., Kawashima, S., and Tsuruta, H.: Carbon monoxide, hydrogen, and methane uptake by soils in a temperate arable field and a forest, J. Geophys. Res., 105, 14347-14362, 2000.

Youn, D., Patten, K. O., Lin, J. T. and Wuebbles, D. J.: Explicit calculation of indirect global warming potentials for halons using atmospheric models, Atmospheric Chemistry and Physics, 9, 8719-8733, 2009.

## APPENDIX A: INTEGRATED GLOBAL TEMPERATURE POTENTIALS

Inspired by the concept of Global Temperature change Potential (GTP) by Shine et al. (2005), I proposed a prospective climate metric, Integrated Global Temperature change Potential (IGTP), defined as the ratio of the integral over a certain time horizon of the temperature change caused by a unit emission of a climate agent of interest, with respect to the integral over the same time horizon of the temperature change caused by a unit emission of $CO_2$. The concept of IGTP can be expressed mathematically as the following equation,

$$IGTP^x(t) = \frac{IAGTP^x(t)}{IAGTP^C(t)} = \frac{\int_0^t AGTP^x(t')dt'}{\int_0^t AGTP^C(t')dt'} \qquad \text{(Eq. A.1)}$$

where $IAGTP^x(t)$ and $IAGTP^C(t)$ are integrated absolute global temperature change potential for the gas x and $CO_2$, respectively; $AGTP^x(t)$ and $AGTP^C(t)$ are absolute global temperature change potential for the gas x and $CO_2$, respectively. $AGTP^x(t)$ and $AGTP^C(t)$ are described in Shine et al. (2005). As for the absolute global temperature change potential, it is important to note that the integrated global temperature change potential has different forms for pulse emissions and sustained emissions.

Integration of AGTP over a time horizon t yields the formula of Integrated AGTP (IAGTP) for a pulse emission of a non-$CO_2$ climate agent emitted into the atmosphere at time zero, as the following equation

$$IAGTP_P^x(t) = \int_0^t AGTP_P^x(t')dt' = \frac{A_x\alpha_x\tau}{C}\left[1 - \frac{\alpha_x}{\alpha_x - \tau}\exp(-\frac{t}{\alpha_x}) + \frac{\tau}{\alpha_x - \tau}\exp(-\frac{t}{\tau})\right] \qquad \text{(Eq. A.2)}$$

where $A_x$, $\alpha_x$, C, and $\tau$ are the radiative forcing for a 1-kg change in concentration of the gas of interest, the atmospheric lifetime of the gas of interest, the heat capacity of the climate system, and the time constant for the climate system, respectively. For $CO_2$, the IAGTP for a pulse emission is the following

$$IAGTP_P^C(t) = \int_0^t AGTP_P^C(t')dt' = \frac{A^C}{C}\left\{\tau a_0[t - \tau + \tau\exp(-\frac{t}{\tau})] + \sum_i \frac{a_i}{\left(\tau^{-1} - \alpha_i^{-1}\right)}\left[\alpha_i - \tau - \alpha_i\exp(-\frac{t}{\alpha_i})) + \tau\exp(-\frac{t}{\tau})\right]\right\}$$

(Eq. A.3)

The IGTP for a pulse emission of x can be derived using the following equation

$$IGTP_P^x(t) = \frac{IAGTP_P^x(t)}{IAGTP_P^C(t)} = \frac{\int_0^t AGTP_P^x(t')dt'}{\int_0^t AGTP_P^C(t')dt'} \quad \text{(Eq. A.4)}$$

Similarly, formulae of IAGTP for sustained emissions can be derived. $IAGTP_s$ for a non-$CO_2$ gas can be written as

$$IAGTP_S^x(t) = \int_0^t AGTP_S^x(t')dt' = \frac{A_x\alpha_x\tau}{C}\left[t - \tau - \alpha_x + \frac{\alpha_x^2}{\alpha_x - \tau}\exp(-\frac{t}{\alpha_x}) - \frac{\tau^2}{\alpha_x - \tau}\exp(-\frac{t}{\tau})\right]$$

(Eq. A.5)

$IAGTP_s$ for $CO_2$ can be written as

$$IAGTP_S^C(t) = \int_0^t AGTP_S^C(t')dt' = \frac{A^C\tau}{C}\left\{a_0\left[\frac{1}{2}t^2 - \tau t + \tau^2 - \tau^2\exp(-\frac{t}{\tau})\right] + \sum_i a_i\alpha_i\left[t - \tau - \alpha_i + \frac{\alpha_x^2}{\alpha_x - \tau}\exp(-\frac{t}{\alpha_x}) - \frac{\tau^2}{\alpha_x - \tau}\exp(-\frac{t}{\tau})\right]\right\}$$

(Eq. A.6)

Thus the IGTP for sustained emission is:

$$IGTP_S^x(t) = \frac{IAGTP_S^x(t)}{IAGTP_S^C(t)} = \frac{\int_0^t AGTP_S^x(t')dt'}{\int_0^t AGTP_S^C(t')dt'} \qquad \text{(Eq. A.7)}$$

The IGTP values calculated for pulse and sustained emissions using Eqs. A.4 and A.7, respectively, for five illustrative climate gases are listed in Table A1.1.

## Appendix A Table

Table A1.1 Integrated AGTP of pulse (in K (kg $yr^{-1}$)$^{-1}$ yr ) or sustained (K (kg $yr^{-1}$)$^{-1}$ $yr^2$) $CO_2$ emissions and $IGTP_p$ and $IGTP_s$ values for five illustrative cliamate gases.

| | $IGTP_p$ | | | $IGTP_s$ | | |
|---|---|---|---|---|---|---|
| Time Horizon (yr) | 20 | 100 | 500 | 20 | 100 | 500 |
| IAGTP $CO_2$ | 1.25 | 6.71 | 23.1 | 1 | 35 | 653 |
| HFC-152a | 569 | 129 | 37 | 839 | 220 | 65 |
| $CH_4$ | 69 | 24 | 7 | 75 | 37 | 12 |
| HFC-134a | 3587 | 1366 | 398 | 3847 | 2008 | 669 |
| $N_2O$ | 262 | 293 | 155 | 250 | 290 | 210 |
| $CF_4$ | 3608 | 5473 | 8674 | 609 | 4793 | 7522 |